The Deep Optical ZoA Galaxy Catalogue in Vela

First Indications of Previously Hidden Large-Scale Structures

Kosma von Maltitz

May 2012

A project submitted in partial fulfilment of the requirements for the degree M.Sc. in the Department of Astronomy, as part of the National Astrophysics and Space Science Programme
UNIVERSITY OF CAPE TOWN

Supervisors: Prof. R.C. Kraan-Korteweg and A/Prof. P. A. Woudt

Abstract

This thesis presents a deep optical galaxy catalogue of the Vela region in the Zone of Avoidance ($|b| < 10°, 245° < l < 280°$). This region was searched for galaxy candidates by optical inspection of IIIaJ (3950 Å to 5400 Å) film copies of the ESO/SRC sky survey as part of an effort to reduce the ZoA. The mapping and identification of Large-Scale Structure (LSS) is essential for understanding the origin of the CMB dipole (the direction and foremost convergence radius), and the dynamics in the Local Universe in general, which not only has historically been hampered by a lack of data in the ZoA, but still is.

The deep optical Vela galaxy catalogue lists 3922 galaxy candidates and is complete to an apparent diameter limit of 12″. An additional 388 galaxies were recorded that have diameters below the 12″ limit. The 279 galaxy candidates who's extragalactic natures were in question were flagged.

Rough positions for the galaxies from the photographic plates were remeasured on the astrometrically calibrated Digitized Sky Survey to an accuracy of 1.″3. Major and minor apparent diameters were recorded ($\sigma_D \sim 6''$). The apparent magnitude estimates were calculated from the average surface density over the apparent area of each galaxy. The estimated magnitudes have a dispersion of $0\overset{m}{.}75$. The morphology of galaxies with sufficient resolution were noted. In this dust obscured region of the sky, galaxies are traced to extinction levels of $A_B \sim 3^m$. Due to the varying foreground dust obscuration in the ZoA the apparent diameters and magnitudes had to be extinction corrected before analysis could be carried out to determine their LSS.

The Vela catalogue has 311 galaxies with extinction-corrected diameters greater than $D^0 > 1.'3$. However, only 56 (18%) of these where recorded in the ESO-LV catalogue. The latter has been found to be complete to $D^0 = 1.'3$. Given that the Vela region is not as effected by star crowding as areas closer to the Galactic bulge, a higher fraction ($\sim 50\%$, N=2106) of galaxy counterparts were identified in the 2MASS Extended Source Catalogue than in similarly surveyed regions.

Analysis of the two dimensional distribution of the galaxies reveals strong clustering. This distribution was examined in extinction-corrected magnitude intervals to roughly differentiate between nearby and distant structures. This distribution was then used to plan a preliminary follow-up redshift survey with the 1.9-m Radcliffe telescope at SAAO. Thirty new redshifts were determined and found to be most sensitive to velocities below $10\,000\,\mathrm{km\,s^{-1}}$.

The combination of the new SAAO redshifts, ~ 300 redshifts from two ZoA 6dF fields (Anglo Australian Telescope) and published redshifts in and surrounding the Vela region indicate prominent Large-Scale Structures between $9\,000\,\mathrm{km\,s^{-1}}$ and $11\,000\,\mathrm{km\,s^{-1}}$ and an unexpected, very extended and surprisingly smooth prominent overdensity between $18\,000\,\mathrm{km\,s^{-1}}$ and $20\,000\,\mathrm{km\,s^{-1}}$.

Recent bulk flow studies indicate that the direction and convergence radius of the CMB may well be in the direction of the Vela region and at the distance of the massive overdensity.

Acknowledgements

I would like to thank my supervisor Prof Renée C. Kraan-Korteweg for her time, patience, encouragement and guidance to me to complete this thesis. I also want to thank my co-supervisor A/Prof. Patrick A. Woudt for his support and guidance during this project, especially with the spectroscopic observations and data analysis. Thank you to Dr. Anja Schröder for being of invaluable support, especially during the last few months.

To all my friends and colleagues (still here and who have left) in the UCT Astronomy Department and at the SAAO, thank you for insightful conversations and providing a supportive working environment. The staff at SAAO, Sutherland deserve my thanks for helping my observing runs go smoothly, particularly when the telescope suffered technical problems.

Thank you to my numerous office mates, Tom, Deanne, Sally, Vinesh, Moses, Mpati, Iniyan: fun times! Thank you Bryony for emergency proofreading and essential tea breaks. A special thank you to my friend Wendy Williams who read countless drafts, discussed the details and is just an amazing, brilliant friend! Charlotte en Esti, julle ondersteuning en vriendskap dra my, dankie maatjies, JDB! And last but certainly not least, I want to thank my family, without whom this would all not have been possible.

Finally, I would like to acknowledge the National Astrophysics and Space Science Programme (NASSP) and the National Research Foundation (NRF) for funding and supporting this work.

Plagiarism Declaration

I, Kosma von Maltitz, know the meaning of plagiarism and declare that all of the work in the document, save for that which is properly acknowledged, is my own.

Contents

List of Figures

List of Tables

Chapter 1

Introduction

This thesis presents the results from a deep optical galaxy search in the Vela region within the Zone of Avoidance (ZoA). The search was undertaken to reduce the optical ZoA and thereby improve the understanding of streaming motions due to the mass distribution in the local Universe. The exact origins of all the mass contributors of the Cosmic Microwave Background (CMB) dipole still remains unclear, with the current 'great attractors' unable to fully account for the Local Group's (LG's) peculiar velocity.

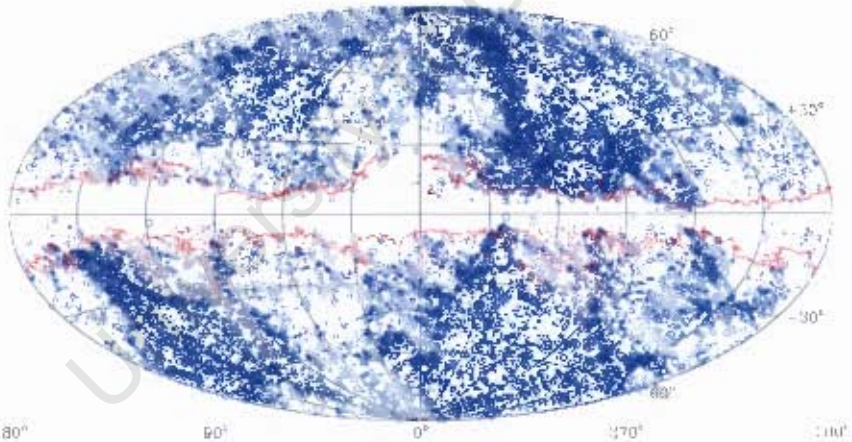

Figure 1.1: The figure shows all optically detected galaxies with diameters $D > 1.3'$. The red contour shows one magnitude of extinction in the blue ($A_B = 1^m$), which clearly describes the optical ZoA. This figure has been reproduced from Kraan-Korteweg & Lahav (2000).

The on-sky distribution of optically detected galaxies with $D > 1.3$ (Fig. 1.1) shows galaxies clearly forming regions of high density as well as sparsely populated areas. These formations are known as Large-Scale Structure (LSS) and form a labyrinth of structures with galaxy clusters, filaments and voids (Fairall 1998). The red contour in Fig. 1.1 describes one magnitude of extinction in the blue ($A_B = 1^m$), which clearly outlines the optical ZoA where there is a lack of data. LSSs such as the Super Galactic Plane (de Vaucouleurs 1958), the

Perceus-Pisces Chain (Chamaraux et al. 1990), the Hydra-Antlia Supercluster (SC) (Kraan-Korteweg et al. 1995) and the Centaurus SC (Fairall 1998) cross and/or continue into the ZoA.

Overdensities of galaxies influence the dynamics of their surrounding neighbourhood: galaxies move towards clusters and filaments, and 'away' from voids. An all-sky map of the galaxy distribution is vital to understanding the motion of the LG itself. However the most prominent feature in Fig. 1.1 is the ZoA.The Milky Way contains vast amounts of dust and stars. Light from galaxies located behind the Galactic Plane is absorbed and scattered by dust and obscured by stars of the Milky Way. This creates the Zone of Avoidance (ZoA), a region where the extragalactic sky is hidden from view.

This thesis forms part of the effort to fill that gap, adding a piece to the puzzle that will help resolve this question. The following sections present an historic overview of the efforts to map the LSS in the ZoA, highlighting efforts to map the ZoA in different wavelength regimes. Special emphasis is placed on the optical searches for galaxies as motivation for investigating the Vela region which is the focus of this project.

1.1 Historic Review of the Zone of Avoidance

The ZoA was first noticed by Proctor (1887) as a gap in the nebulae distribution in the Catalogue of Nebulae and Clusters of Stars (Herschel 1864). At this point it was not known that some 'nebulae' where in fact extragalactic objects. In the early 1920's, the so-called 'Great Debate' took place between Shapley and Curtis about the scale of the Universe. Shapley argued that if the spiral nebulae were beyond the Milky Way their distances would be inconceivably large, and therefore they must reside within the Milky Way. Curtis on the other hand argued for Kant's (1755) *island universes*, and regarded spiral nebulae as objects external to the Milky Way. One of the sources of confusion in resolving the Great Debate was the incorrect scale of the Milky Way, which was heavily underestimated because the impact of dust was not known at the time. In 1925 Hubble resolved the debate by placing the distances of the nebulae well beyond the dimensions of the Milky Way. No connection had yet been made between the Milky Way and Procter's Zone of few Nebulae.

In 1930 Trumpler showed that 'fine cosmic dust' in the plane of the Milky Way causes the extinction of light, which makes the extragalactic sky *appear* sparsely populated. The dust in the Galactic Plane causes galaxies to be fainter and have reduced diameters.

In 1961 Shapley defined the ZoA as the region where he found $N \leq 5$ galaxies per square degree, as opposed to the average of 54 found by Shane & Wirtanen (1967) in non-obscured regions. A second factor, besides the dust, that complicates looking at galaxies in the ZoA is confusion and obscuration by star-crowding, especially towards the Galactic bulge.

The extent of the ZoA is wavelength-dependent. Recent surveys find that about 20% of the optical extragalactic sky is heavily obscured by the Milky Way (Kraan-Korteweg & Lahav 2000, see Fig.1.1:). At infrared (IR) wavelengths the percentage of the sky obscured only amounts to about 10% (e.g. 2MASX the 2MASS Extended Source Catalogue: Jarrett

et al. 2000). Each wavelength has different advantages and disadvantages for searching the ZoA (discussed further in Section 1.3: Kraan-Korteweg & Lahav 2000).

1.2 Motions in The Local Universe

Concentrations of mass beyond our LG contribute to the appearance of a dipole in the CMB (Fig. 1.2) towards $(l, b, v) \sim (277°, 30°, 622 \mathrm{kms}^{-1})$ (COBE,WMAP; Lineweaver et al. 1996, Bennett et al. 2003). Tammann & Sandage (1985) determined that the Virgo Cluster could not account wholly for the CMB dipole. Early reconstructions of the peculiar velocity flow fields by Lynden-Bell et al. (1988) using an all-sky elliptical galaxy sample around the ZoA indicated that important attractors lie hidden by the Milky Way. In particular the significance of the Great Attractor region was first recognised by this whole-sky peculiar velocity study.

The Great Attractor and the Shapley Super Concentration have been the greatest contenders for the major fraction of the origin of the LG's peculiar velocity. Giovanelli (1999) and Courteau (2000) are proponents of these structures being the answer. Peculiar velocity flow studies (2MASX, Erdoğdu et al., Erdoğdu et al. 2006a;b, X-ray clusters, Kocevski & Ebeling 2006) suggest the mass hidden behind the Milky Way could be the key to solving this conundrum. More recent bulk flow studies suggest that the local bulk flow is generated at distances beyond 100 Mpc (Hudson et al. 2004, Feldman et al. 2010, Macaulay et al. 2011). Other surveys even claim a significant increase in the dipole amplitude up to and beyond 300 Mpc (Kashlinsky et al. 2008; 2010, 2011, Abate & Feldman 2012). All of these studies and surveys suggest convergence towards low Galactic latitudes in the Southern ZoA for the location of the missing attractor(s).

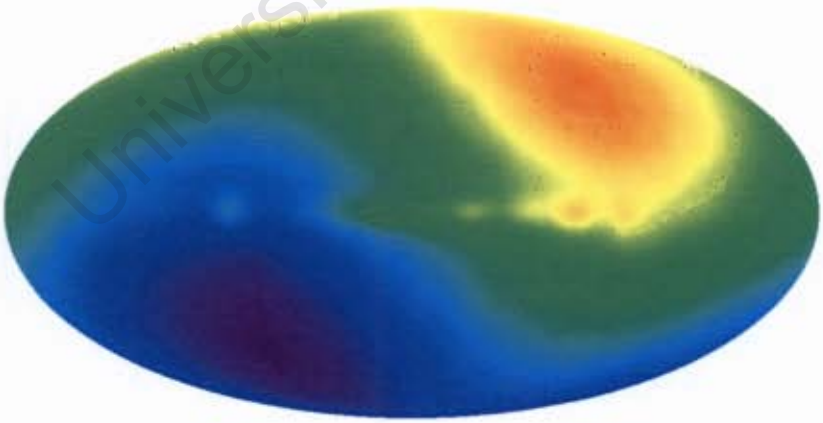

Figure 1.2: 53 GHz DMR sky map of COBE-DIRBE showing the dipole observed. (Lineweaver et al. 1996)

Subtracting the peculiar velocities of known attractors from the CMB dipole causes a change in the position of the apex towards which the LG is moving. Furthermore, as nearby

attractors are accounted for, the convergence radius of volume of influence increases. Gravity is inversely proportional to the distance squared. A cluster three times more distant must be nine times more massive to induce the same gravitational acceleration. Therefore an attractor with equal influence as the GA ($\sim$ 65Mpc) beyond 200 Mpc, as suggested by some studies, must be at least 9.5 times as massive as the GA to produce a similar acceleration locally. An inhomogeneity this large is a challenge to the current model of cosmology that advocates homogeneity on scales of $\sim$ 100 Mpc (Joyce et al. 2005, Hogg et al. 2005).

Attempts at simulating the galaxy distribution in the ZoA by statistical interpolation of the mass distribution of adjacent regions (Lynden-Bell et al. 1989, Yahil et al. 1991, Lahav et al. 1991, Loeb & Narayan 2008) have had varied success but more significantly show how important a role the missing matter plays. On the other hand, Kolatt et al. (1995), interpolated the potential field into the ZoA instead of the mass distribution, and found that the unaccounted for mass is highly relevant for the resulting dipole direction.

1.3 Mapping the ZoA

The ZoA has been investigated by various methods at different wavelengths. They are described, with special emphasis on the optical since it is relevant to this thesis.

1.3.1 Optical Searches in the ZoA

In the optical part of the spectrum the dust in the Milky Way causes extended objects that lie behind our Galaxy to appear smaller and fainter. Star-crowding can cause misidentification of blended stars as an extended object and many galaxies have super-imposed stars on them. Optical surveys are sensitive to all morphologies, detecting ellipticals, spirals and nearby dwarfs.

Inspection of photographic plates by eye has proven a successful method of identifying galaxy candidates in the optical ZoA. Attempts at automated scanning of the plates, as for example the Co-Ordinates, Sizes, Magnitudes, Orientations and Shapes (COSMOS; Pratt 1977, Drinkwater et al. 1995) machine and automated photographic measuring (APM; Lewis & Irwin 1996) facility, have been successful in correctly identifying a large sample of galaxies but misidentify an equally large sample of blended stars as extended objects in the ZoA. Visual examination by eye remains the most powerful tool in identifying galaxies in areas of high star densities.

Systematic deep optical searches for galaxies hidden by the ZoA, by eye, were started in the late 1980's by different research groups. Most of the ZoA has now been surveyed for $|b| \lesssim 10^{\circ}$. Following Kraan-Korteweg & Lahav (2000) Fig. 1.3 demarcates the regions observed in galactic coordinates centred on the bulge. Region A was investigated on POSS E prints by Pantoja et al. (1997; 1994) to explore the extent of the Perceus-Pisces complex. Regions B_1-B_3 where searched on the POSS I and POSS II survey plates by Seeberger & Saurer (1998), Seeberger et al. (1996; 1994), Lercher et al. (1996), Saurer et al. (1997) (B_1),

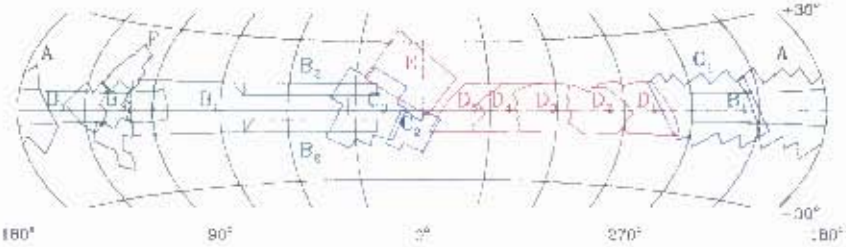

Figure 1.3: Optical survey regions in the ZoA (Kraan-Korteweg & Lahav 2000). Regions D_1 to D_5 have been surveyed by our group.

Marchiotto et al. (1999) (B_2) and Weinberger et al. (1999) (B_3). These regions completed the northern sky surveys. The survey of region C_1 was led by Saito et al. (1991; 1990) and due to the low extinction levels in this region found 7000 new galaxies. Region C_2 and C_3, near the bulge, where investigated by Roman et al. (1998; 1996) respectively. Region E hosts the Ophiuchus (Johnston et al. 1981, Wakamatsu & Malkan 1981) and Sagittarius clusters which led to a deeper survey that revealed 4000 new galaxies (Wakamatsu et al. 1994, Hasegawa et al. 2000a). Region F has been surveyed to find more members of the Supergalactic Plane (Hau et al. 1995).

Subsequent deep optical surveys have revealed dynamically important nearby ($\sim$ 1000 - 6000 km s^{-1}) structures such as the Puppis cluster, the Ophiuchus Cluster (Hasegawa et al. 2000b, Wakamatsu et al. 2005), the Norma cluster (Woudt 1998a) and the local Void (Tully & Fisher 1987).

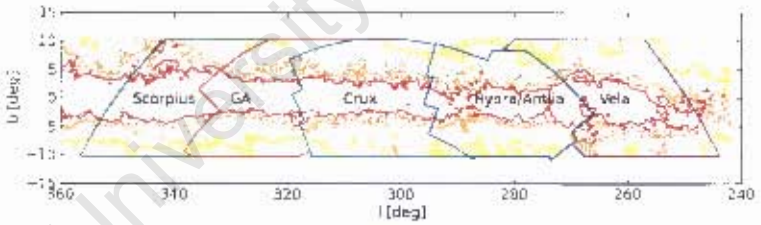

Figure 1.4: The regions searched optically for extended objects: Scorpius, GA, Crux, Hydra/Antlia and Vela regions (*from left to right*) The dust extinction contours are shown in red ($A_B = 3^m$), orange ($A_B = 3^m$) and yellow ($A_B = 1^m$).

A systematic optical search of the southern ZoA ($250° < l < 350°$, regions D_1 - D_5 in Fig. 1.3), led by Kraan-Korteweg was started in 1990. Using the deep ESO/SRC sky survey, the survey areas are separated into five contiguous regions, namely the Scorpius (D_5), Crux (D_4), Great Attractor (GA, D_3), Hydra/Antlia (D_2) and Vela (D_1) regions. In Fig. 1.4 these five regions are outlined in Galactic coordinates. The dust extinction (A_B) contours as derived from the Diffuse Infra-red Background Experiment (DIRBE; Schlegel et al. 1998) are also shown. The catalogues for the Hydra/Antlia, GA, and Crux regions have been published in Kraan-Korteweg (2000) and Woudt & Kraan-Korteweg (2001). These catalogues have

facilitated reducing the optical ZoA in this region of the Galactic Plane (GP) to lower galactic latitudes, from $|b| \lesssim 10°$ to $|b| \lesssim 5°$, and higher levels of extinction, from $A_B \lesssim 1$ mag to $A_B \lesssim 3$ mag. Analysis of the GA region, so called because it covers a great fraction of the GA, led to the discovery of the massive Norma cluster which is comparable in richness to the Coma cluster and is located at the centre of the GA (Kraan-Korteweg et al. 1996, Woudt 1998b, Woudt et al. 2008). The Hydra/Antlia region revealed an extension to the Antlia and Hydra clusters (Kraan-Korteweg et al. 1994, Kraan-Korteweg 2000).

The completed regions were found to be complete to an apparent diameter of $12''$ which corresponds to an isophotal magnitude of approximately 24.5 mag/arcsec^2. The Scorpius catalogue is in preparation for publication, but has been used for preliminary analysis and a redshift survey (Fairall & Kraan-Korteweg 2000).

This thesis covers the optical search of the Vela region, the final part of this series that spans $\sim 90°$ of the southern ZoA. With the completion of this project the whole optical ZoA will then have been surveyed.

1.3.2 HI Searches of the ZoA

THe 21-cm HI emission is not hampered by the ZoA. The HI Parkes Deep Zone of Avoidance Survey (HIZOA survey; Henning et al. 2005) and its northern extension (Donley et al. 2005) covered $|b| < 5°$. Due to dust and stars the Galactic Bulge extension (Shafi 2008) was extended to $|b| < 10°$. Over a thousand gas-rich galaxies were revealed in the southern ZOA out to $v \lesssim 12\,000 \mathrm{km\,s^{-1}}$, where most observing methods do not penetrate the ZoA. HIZOA still very sparsely sampled the area revealing only $\sim 0.5\,\mathrm{gal}/\square°$.

However, while HI observations are the only survey method that can trace LSS unbiased across the ZoA, they are biased towards HI rich spiral galaxies. Future surveys such as WALLABY (Koribalski & López-Sánchez 2009) the ASKAP HI All-Sky Survey, will probe much deeper and detect fainter (i.e. more distant and/or less HI massive) galaxies.

1.3.3 The Infrared ZoA

The Infrared (IR) Astronomy Satellite (IRAS: Neugebauer et al. 1984, Soifer et al. 1987) Sky Survey Atlas (ISSA: Wheelock et al. 1994) was the pioneering all-sky IR survey. IRAS was carried out in the far-infrared. At low galactic latitudes, and therefore around the ZoA, IRAS is incomplete due to Galactic sources dominating the signal.

The 2 Micron All Sky Survey (2MASS Skrutskie et al. 2006) revolutionised our view of the near infrared (NIR) sky. It revealed many uncharted galaxies and probed deeply into the ZoA. NIR observations are less effected by extinction, but are hampered where star density is high. NIR observations are however biased towards ellipticals because they are dominated by an old stellar population. The recent release of the 2MASS Redshift Survey (2MRS: Huchra et al. 2011) will be useful in mapping LSS.

The most recent surveys in the ZoA were carried out using the mid-infrared (MIR) space telescope *SPITZER*. One was the Galactic Legacy Infrared Mid-Plane Survey Extraordinaire

(GLIMPSE: Benjamin et al. 2003, Jarrett et al. 2007) and the other the MIPS Galactic Plane Survey (MIPSGAL: Carey 2008, Marleau et al. 2008). Both revealed a handful of new galaxies in the limited area scanned. In the 2011 the Wide-field Infrared Survey Explorer (WISE) completed its first all-sky scan and covers the whole ZoA (Wright et al. 2010) which opens another avenue to be explored.

1.3.4 X-ray

X-rays are excellent for revealing galaxy clusters and the Clusters In the Zone of Avoidance (CIZA) survey looked specifically behind the Milky Way (Ebeling et al. 2005). X-rays are absorbed by neutral hydrogen and thus the detection of sources is dependent on the HI column density (Böhringer et al. 2000). The HI column density increases towards the Galactic Plane thus leaving the X-ray ZoA where $n_{HI} < 2 \times 10^{21}\mathrm{cm}^{-2}$, which roughly is within $|b| \lesssim 5^{\circ}$.

1.4 The Vela Region

The Vela survey area is of interest and needs to be filled in to show how the numerous LSSs seen in surveys that surround the region extend into or cross the region.

As mentioned in Sec. 1.3.1, the Vela region ($245^{\circ} \lesssim l \lesssim 280^{\circ}$, $|b| \leq 10^{\circ}$ in Fig. 1.4) is the last region outstanding in a systematic deep optical survey of the southern ZoA using the deep ESO/SRC IIIaJ plates, mapping galaxies with $D > 12''$, which is considerably deeper than most whole-sky surveys that have diameter limits of $D > 1\farcm3$.

Tantalising results from two 6dF fields (Sec. 5.1.1) indicated a large overdensity in the Vela region. Recent bulk flow studies consistently claim that attractor(s) located at $(l) \approx (280^{\circ})$ in the ZoA, beyond 100 Mpc (Hudson et al. 2004, Feldman et al. 2010, Macaulay et al. 2011) and even 300 Mpc (Kashlinsky et al. 2008; 2010; 2011, Abate & Feldman 2012), are contributing significantly to the peculiar velocity of the LG. Inspection of the LSS surrounding the area indicate stuctures crossing/leading into the Vela region at the redshifts suggested by these studies.

Confirmation of such a large overdensity in the Vela region, and a measure of its extent, could contribute significantly towards explaining the discrepency between the observed dipole (e.g. Hudson et al. 2004) and the CMB dipole, with the addition of a significant accelerator at large distances ($\sim$ 180Mpc) and the controversy around radius of influence of the various bulk flow results. In addition such a large, extended overdensity is not in agreement with the currently favoured Lambda CDM cosmology model, as was shown by Lavaux et al. (2010) and Bilicki et al. (2011) in their comparisons of LSS to the expected Lambda CDM predictions. They state that if there are massive overdensities on scales greater than $\sim$100 Mpc the agreement becomes unlikely.

The Vela region is surrounded by filamentary structure and clusters at different redshifts. When looking at the 2MASX photometric redshift slice between $0.06 < z0.07(\sim$ 18000 –

20000 km s^{-1}, $\sim$ 200 Mpc) there is a filamentary structure that disappears into the Vela region from above the Galactic Plane (Jarrett 2004). Similarly the 6dFGS displays a similar filament entering the Vela region from below the plane at that redshift interval, in which two CIZA clusters are seen.

Figure 1.5 has six panels that depict known galaxy redshifts between $|b| < 30°$ and $240° < l < 300°$. The redshifts come from the HYPERLEDA database, the 6dF Galaxy Survey (6dFGS) and 2MRS (Macri L. 2011, priv communication). Note that very few redshifts are available within 10 degrees of the Galactic Plane. The different velocity intervals, each an interval of Δv =3500 km s^{-1}, were chosen to highlight the LSS present.

In the top left panel (red) we see the interval $0 < v < 3500$ km s^{-1}. The Antlia ($(l, b) = (272.^{\circ}9, 19.^{\circ}2)$) and Hydra clusters ($(l, b) = (269.^{\circ}6, 26.^{\circ}5)$) are clearly visible. The so-called Vela cluster (Abell S0639; Stein 1996) is located at $(l, b, v) = (280.^{\circ}5345, 10.^{\circ}9079, 6326$ km s$^{-1})$ in the top right hand panel (magenta; $3500 < v < 7000$ km s^{-1}). The middle left panel (blue; $7000 < v < 10500$ km s^{-1}) shows structure coming into the Vela region at $(l, b) \sim (250°, -10°)$.

The lime dots ($14000 < v < 17500$ km s^{-1}) show an intersection filament-like structure going through the Hydra-Antlia region. The green dots ($14000 < v < 17500$ km s^{-1}) show a structure entering the Hydra-Antlia region at $(l, b) \sim (270°, -10°)$. This is also where the two CIZA (CIZA J0812.5-5714 and CIZA J0820.9-5704, large cyan stars)) clusters are seen.

Filling in the Vela region will reduce the ZoA between $245° \lesssim l \lesssim 280°$ and provide a catalogue for follow-up investigations in this region. Then the extent and dynamical importance of hinted structure can be confirmed.

1.5 Overview

The aim of this thesis is to present the deep optical survey galaxy catalogue of the Vela region in the ZoA ($245° < l < 280°, |b| \leq 10°$) and the first follow-up spectroscopy for this region. This chapter has given the background and motivation for the project.

In Chapter 2 the compilation of the catalogue is discussed in detail. The search of the photographic plates, the parameter derivation and calibration (Sec. 2.2-2.3) as well as their quality assessment are included. The Vela region lies in the dust-obscured ZoA and the parameters of galaxy candidates are extinction corrected (Sec. 2.4). Finally Sec. 2.5 gives a full description of the catalogue (which is listed in its entirety in Appendix A).

The properties of the galaxy catalogue, which include the magnitude and diameter distributions (Sec. 3.1.1) and their dependence on foreground extinction (Sec. 3.1.2), and the completeness of the survey are discussed in Chapter 3. Furthermore, in Sec. 3.2 the on-sky distributions of the galaxies as a function of extinction-corrected diameters (Sec. 3.2.1), morphology (Sec. 3.2.2) and extinction-corrected magnitudes (Sec. 3.2.3) are examined for first indications of structure.

Chapter 4 discusses the data collection, reduction and results from the observing run at the 1.9m Radcliffe telescope in Sutherland. In addition the preliminary results from two

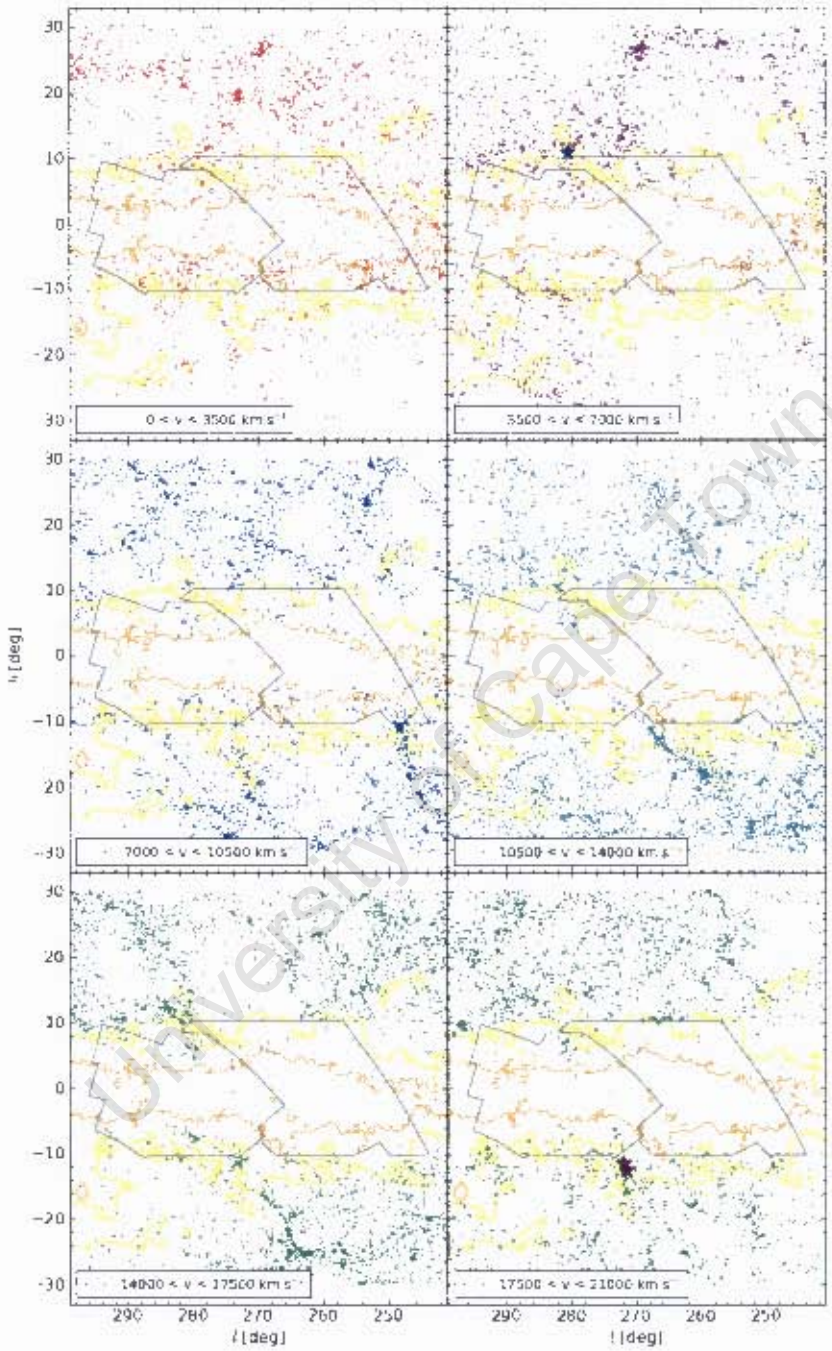

Figure 1.5: Known galaxy redshifts between $|b| < 30°$ and $240° < l < 300°$ in velocity intervals of 3500 km s^{-1}. Abell S0639 (blue star) is located in the top right hand panel (magenta; $3500 < v < 7000$ km s^{-1}). In the bottom right panel (green; $14000 < v < 17500$ km s^{-1}) are the two CIZA (CIZA J0812.5-5714 and CIZA J0820.9-5704, cyan stars) clusters.

6dF fields taken with the Anglo Australian Telescope (AAT) are shown.

Chapter 5 shows how the 30 new redshifts (from the 1.9-m Radcliffe telescope) combined with ~ 300 redshifts from the two 6dF fields and published redshifts in and surrounding the Vela region indicate LSS.

The last chapter is a summary of the findings of this thesis and a look towards the future opportunities opened by the Vela catalogue.

Chapter 2

The Vela Catalogue

The Vela region ($245° \lesssim l \lesssim 280°, |b| \leq 10°$) is the fifth in a series of regions (Kraan-Korteweg 2000, Fairall & Kraan-Korteweg 2000, Kraan-Korteweg & Lahav 2000, Woudt & Kraan-Korteweg 2001) surveyed for extended objects in the southern ZoA.

In this chapter the steps followed to compile the Vela deep optical catalogue are described in detail. Firstly, in Sec. 2.1, the characteristics of the photographic plates used to survey the region are presented.

For this thesis a distinction needs to be made between the work done by Chadi Salem for his Masters thesis (Salem 1996) when he identified the galaxies of the Vela catalogue and the work that forms part of this dissertation. Salem identified all the galaxy candidates and measured 'raw' parameters for the majority of the objects ($\sim 88\%$) from the plates. Section 2.2 discusses how all these 'raw' parameters were measured, and as part of this thesis, calibrated. Furthermore, this section covers how the final positions, diameters, magnitudes and Hubble types were determined by me.

The subsample of galaxy candidates for which parameters were measured as part of this thesis is discussed in Sec. 2.3. A thorough analysis of how these galaxies were integrated into the greater catalogue is carried out.

Section 2.4 shows how extinction corrections were applied to the observed diameters and magnitudes.

A short description of the final catalogue listed in Appendix A is given in Sec. 2.5.

The properties of the catalogue galaxies are discussed in Sec. 3.1. First the distribution of the observed and extinction-corrected magnitudes and diameters are compared to other regions surveyed in the southern ZoA. Secondly the dependence on Galactic extinction is examined. Finally the completeness of the catalogue is addressed.

At the end of the chapter (Sec. 3.2) a first look is taken at possible indicators of LSS.

2.1 Survey Plates

Galaxies in the Vela region were detected by examining IIIaJ film copies of the ESO/SRC all sky survey. The plates are each exposed $6.5^\circ \times 6.5^\circ$ (35 cm × 35 cm). The blue film was chosen above red film (6300 Å- 6900 Å)in spite of the high extinction levels in the region, since it was found that the hypersensitized and fine-grained emulsion of the blue film facilitated finding galaxy candidates and more detail could be identified in them than the red (Kraan-Korteweg 2000). The band, B_J, has an effective bandpass of 3950 Å to 5400 Å.

Twenty plates were surveyed for the Vela catalogue. They are F209-F210, F258-F263, F311-F316 and F367-F372 limited by Galactic latitude $|b| < 10^\circ$. In total, 4566 extended objects were found on the 20 plates (see Fig. 2.1). Of these galaxy candidates, 3922 have diameters greater than the $12''$ completeness limit (blue and green dots in Fig. 2.1) and 388 have diameters less than $12''$ (red and cyan dots in Fig. 2.1). Smaller galaxies are very difficult to detect and mostly only found in more transparent (low sky-background levels) regions. Moreover, stars do not have diffraction spikes below $12''$, which increases the chance of miss-identifying stars as potential round galaxy candidates. While obvious galaxies with $D < 12''$ were recorded, they have not been included in the main catalogue, nor are they used for the data analysis and LSS identification. The galaxies that fall beneath the diameter limit were identified by being either extremely inclined (edge-on) or by being clearly diffuse. Suspected confusion sources (22) such as HII regions or planetary nebula are noted in the comments.

The green and cyan dots in Fig. 2.1 indicated extended objects whose galactic nature are uncertain. It is clear from the figure that most of these are located in the highest extinction areas where confusion is to be expected, and Galactic objects are more prevalent.

Table 2.1 shows the number of identified galaxy candidates, and a break down of those numbers with respect to certain attributes.

Table 2.1: Summary of numbers given in relation to the Vela catalogue.

Number	Galaxy Candidate Attributes
4566	identified as galaxy candidates
3922	$D \geq 12''$
388	$D < 12''$
279	extragalactic natures are in question
311	$D^0 > 1'.3$
56	counterparts in the $D^0 > 1'.3$ diameter limited Lauberts catalogue
2106	counterparts in the 2MASS XSC

2.2 Parameters

The plates are viewed using a modified blinking machine (Fig. 2.2). The light path is such that it produces a 50 times magnified image; the illuminated part of the plate is

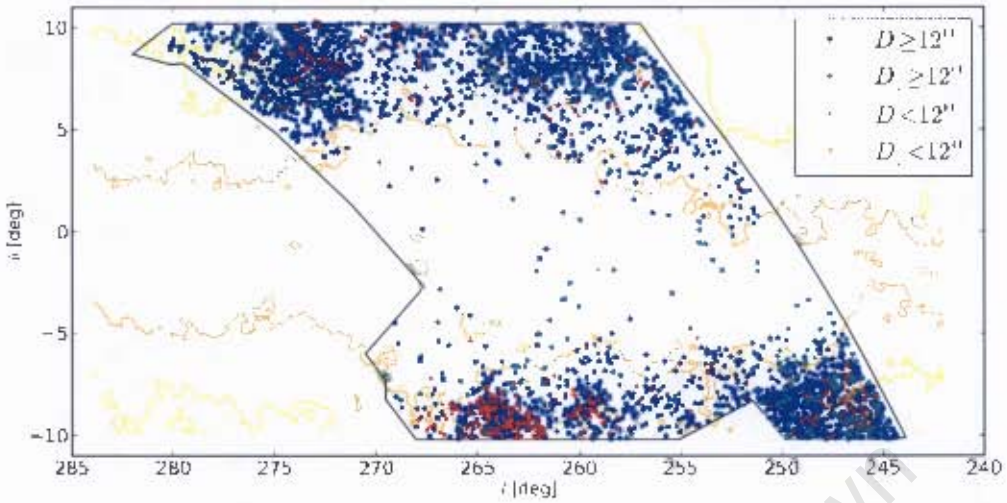

Figure 2.1: All detected extended objects within the Vela region (solid line), galaxy candidates with diameters greater than 12″ are shown as blue dots and those with diameters less than 12″ are depicted by red dots. Extended objects where there is uncertainty about their galactic nature are shown in cyan ($D \geq 12''$) and orange ($D < 12''$) respectively. The three ($A_H - 3^m$) and one ($A_H - 1^m$) magnitude extinction contours are shown in orange and yellow respectively.

projected through a magnifying lens, two prisms and is then reflected off a mirror onto a 18 cm × 19 cm milk glass screen (B in Fig. 2.2). The plates are systematically scanned for extended objects in segments of an area of 3′.5 × 4′.0. The identified objects are marked and assigned a number. In the next step the Cartesian coordinates are measured and then converted to approximate celestial coordinates using known positions of bright stars on the plates. Measurements are also taken of the surface density (the blackness on a plate is a measure for surface brightness), major and minor axes and morphology of the objects. Within a circular area with a diameter of one arcminute around the objects the sky surface density and star density are recorded.

2.2.1 Positions

Approximate positions for all and parameters for 88% of galaxy candidates were determined from the plates by Chadi Salem for his Masters project in 1995-1996. How the missing parameters are determined to complete the catalogue parameters is discussed in Sec. 2.3. He measured the positions (X and Y values) with an illuminated measuring table, by positioning the cross hairs of the measuring instrument over the centre of galaxies. From the equally measured (X, Y) positions of stars with known positions, equatorial coordinates were calculated for the galaxies to within a few tenths of an arcminute. The plan had been to determine more accurate positions with the MAMA measuring machine, a high speed multichannel microdensitometer, Observatoire de Paris in France, but this was never carried out.

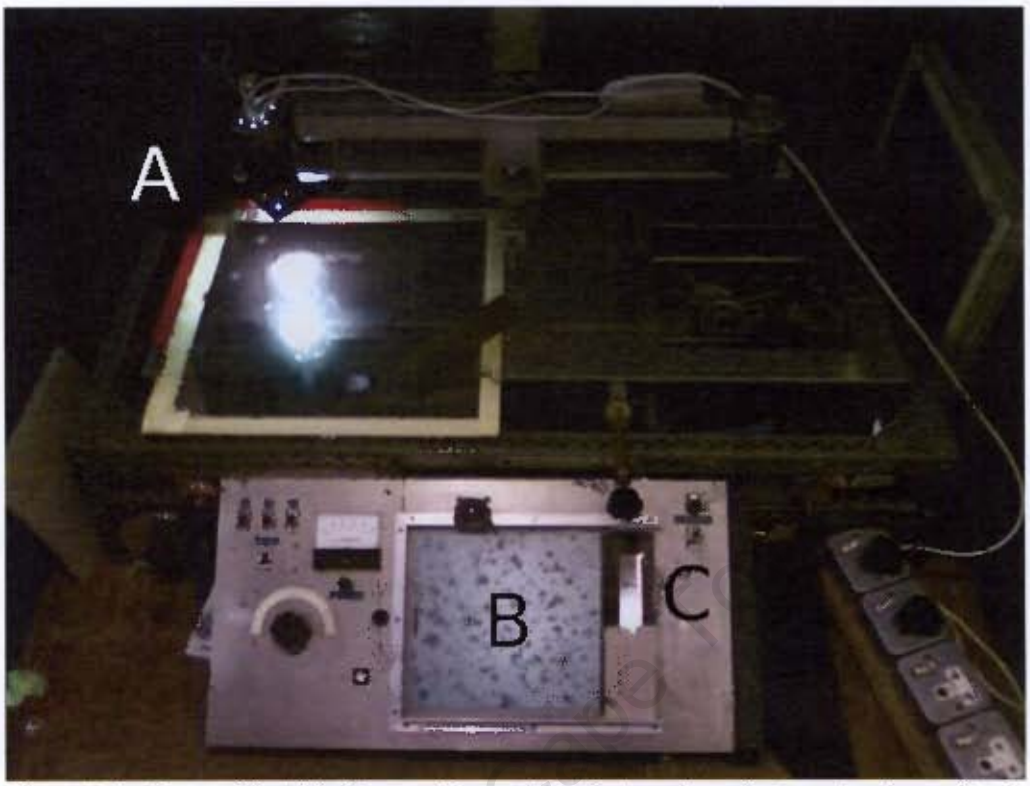

Figure 2.2: The modified blinking machine. 'A' indicates where the tungsten lamp illuminates a small area of the plate. 'B' indicates where the light is projected onto the milk glass. 'C' indicates the twenty-one steps of blackness to compare the plates to.

Identification of galaxies

As the first part of my thesis I used the rough positions as a guideline to identify galaxies on the astrometrically calibrated Digitized Sky Survey[1] (DSS) images. The DSS is a digitised archive of the photographic plates. Images of $1' \times 1'$ around the rough positions were downloaded from the DSS archive. The pixel scale of the images is 1 arcsec/pixel. The positions of the extended objects in the images were found using the software package *jskycat*[2].

Where no extended object could be seen or identified on the DSS image, the relevant plate was inspected by eye for clarity. The plates have a fine-grained emulsion that provide a better resolution than the pixelated DSS images. Many of the low surface brightness (LSB) galaxy features and even entire LSB galaxies are lost in the DSS images.

Figure 2.3 shows the offsets between Salem's rough positions of Right Ascension and

[1] http://archive.eso.org/dss/dss
[2] http://jsky.sourceforge.net

Declination, and the newly measured positions. They are defined as

$$\Delta\mathrm{RA} = \mathrm{RA}_{Vela} - \mathrm{RA}_{Salem} \quad (2.1)$$

$$\Delta\mathrm{Dec} = \mathrm{Dec}_{Vela} - \mathrm{Dec}_{Salem}. \quad (2.2)$$

The sides of the figure display the respective RA and Dec off-sets as histograms. Positions were measured for 1566 objects. Twenty-seven off-sets are not plotted since they are extreme outliers where wrong coordinates must have been entered in Salem's listing (not corresponding to the galaxy numbered on the plate). The apparent stratification in the centre of the distribution is an indication of the limiting 1″ pixel scale of the DSS images. The obtained offset and dispersion around the mean are:

$$\mu_{RA} = -1\farcs0 \mp 0\farcs3 \quad (2.3)$$

$$\sigma_{RA} = 20\farcs1 \quad (2.4)$$

$$\mu_{Dec} = -1\farcs3 \pm 0\farcs2 \quad (2.5)$$

$$\sigma_{Dec} = 16\farcs4. \quad (2.6)$$

The statistics of the distribution seem consistent with the $\sim 20''$ uncertainty estimation by Salem (1996).

Positional Accuracy

To determine the positional uncertainty of the updated positions of the galaxies measured on the DSS images, a comparison with counterparts in the 2 Micron All Sky Survey Extended Source Catalogue (2MASX: Jarrett et al. 2000) was made. There are 2106 2MASX counterparts[3] in the Vela region. There are a high number of 2MASX ZoA counterparts because (a) star crowding is not too severe in the Vela region (compared with the other optical ZoA surveys closer to the Galactic Bulge), and (b) an infrared catalogue is less affected by dust than the optical. Counterparts were searched for within a 12 arcsec radius since that is the diameter cutoff for the extended objects in the Vela catalogue. 2MASX has a positional accuracy of 0.5″ for extended objects (Jarrett et al. 2000). Figure 2.4 shows the positional difference in right ascension and declination, where

$$\Delta\mathrm{RA} = \mathrm{RA}_{Vela} - \mathrm{RA}_{2MASX} \quad (2.7)$$

$$\Delta\mathrm{Dec} = \mathrm{Dec}_{Vela} - \mathrm{Dec}_{2MASX}. \quad (2.8)$$

On the sides of the figure are histograms that show the distribution of the respective offsets. Out of the 2106 counter parts only 92(2%) have positional differences greater than 3″ and only 93(2%) between $2'' - 3''$.

[3]Counterparts are in Appendix A in Table A.3.

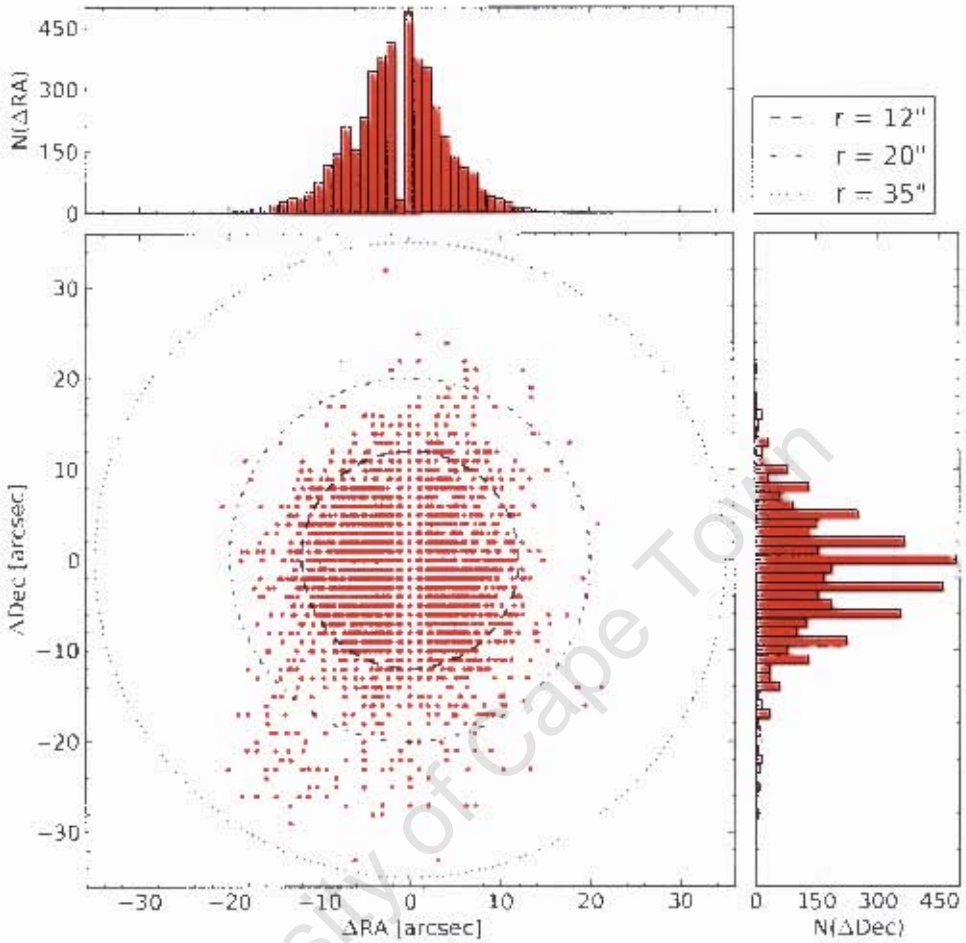

Figure 2.3: Offsets between the rough RA and Dec measurements by Salem and the newly measured positions from DSS images.

The obtained offset and dispersion around the mean RA and Dec are:

$$\mu_{RA} = -0\farcs1 \pm 0\farcs0 \quad (2.9)$$

$$\sigma_{RA} = 1\farcs2 \quad (2.10)$$

$$\mu_{Dec} = 0\farcs2 + 0\farcs0 \quad (2.11)$$

$$\sigma_{Dec} = 1\farcs3. \quad (2.12)$$

The average difference in the Right Ascension and the average difference in the Declination with 2MASX counterparts shows no systematics in the positional offsets (see e.g. Kraan-Korteweg & Jarrett 2005).

Taking the positional uncertainty contributions of the 2MASX (0.5″) positions and

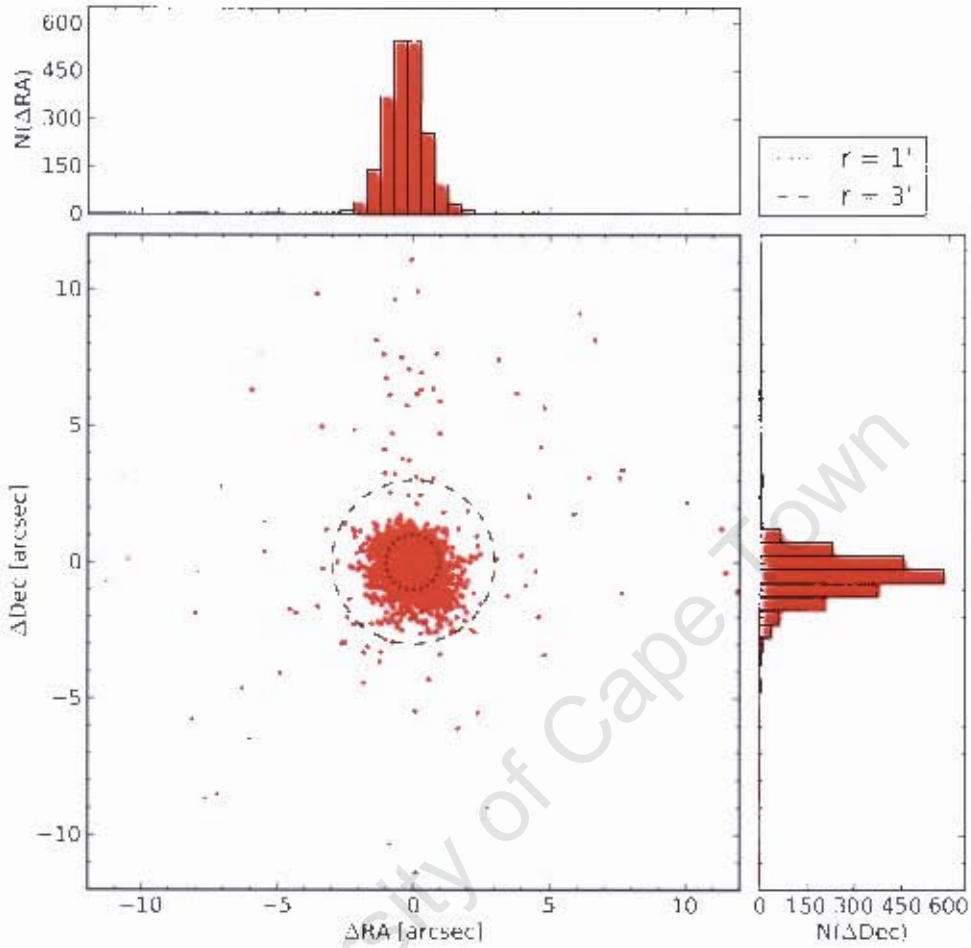

Figure 2.4: Offset of the RA and Dec of Vela catalogue positions and their 2MASS counterparts positions.

considering the 1″/pixel limit imposed by the DSS images, the uncertainty in the RA and Dec of 1.2″ and 1.3″ could not have been better.

2.2.2 Diameters

Diameter of the major and minor axes were measured on the magnified projected image on the milk glass screen (B in Fig. 2.2) with a ruler in units of millimetres. The units were then converted to arcseconds by a conversion factor. Given that the plate scale is 67.2 ″/mm (UK Schmidt Telescope Handbook, 1983), the conversion factor from mm on 50 times magnified scale to arcseconds is $[''] = [\mathrm{mm}] \times \frac{67.2\,''/\mathrm{mm}}{50} = [\mathrm{mm}] \times 1.344[''/\mathrm{mm}]$.

In the next subsections the diameters will be compared to first the Lauberts (ESO-LV; 1982) catalogue (Sec. 2.2.2), secondly, overlapping galaxies with the adjacent Hydra-Antlia

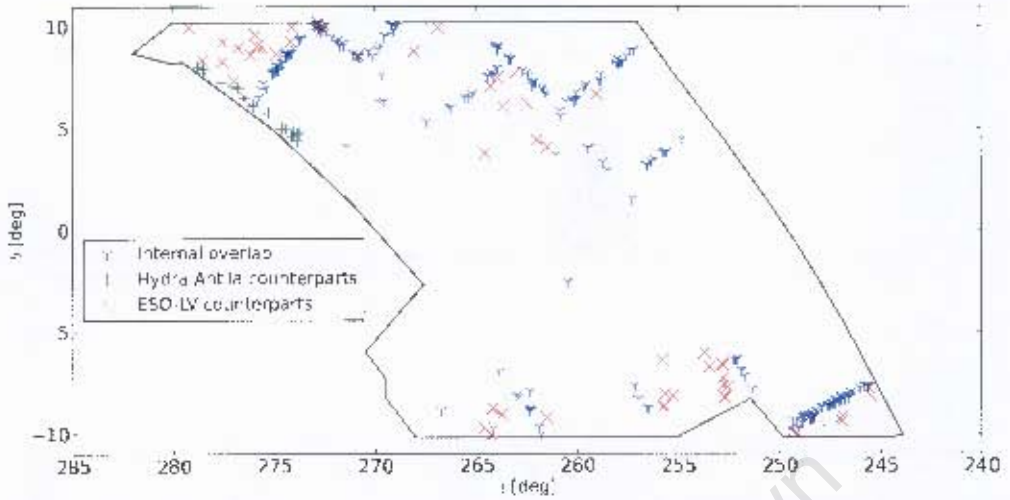

Figure 2.5: Internal overlap galaxies are shown in blue 'Y' symbols. Counterparts from ESO-LV and the Hydra-Antlia catalogues are shown in red 'x' symbols and green '+' symbols respectively.

(Sec. 2.2.2) and, finally, overlapping galaxies where internal plates overlap (Sec 2.2.2). Note that the latter two will lead to upper limits of errors because these galaxies are located on the edges of the plates.

Comparison to the ESO-LV catalogue assesses the reliability of the derived diameters in context to other diameter values. Comparing the Vela diameters with the Hydra-Antlia diameters, which is the region adjacent to Vela in the Southern ZoA Survey (Kraan-Korteweg 2000), gives insight as to how well the diameters compare to the other four optical Southern ZoA Surveys.

I furthermore did an internal check for galaxies within the Vela catalogue, where plate borders overlap and where therefore galaxies were identified multiple times. Figure 2.5 shows the Vela region (outlined in black), with the internally overlapping galaxies shown in blue. Counterparts in the ESO-LV and Hydra-Antlia catalogues are shown in red and green respectively.

Comparison with ESO-LV

A comparison is made to the diameters of the 25^{th} B magnitude isophote (D_{25}) of counterparts in the ESO-LV catalogue (shown in Fig. 2.5 as red 'x' symbols). Kraan-Korteweg (2000) found that the measured diameters correspond approximately to a 24.5 mag/arcsec^2 isophote.

Figure 2.6 displays the comparison of the 56 ESO-LV D_{25} counterparts with the Vela catalogue. Galaxy 307-004 is an outlier excluded from the fit because it has a very faint disk that clearly was not measured properly in the Lauberts catalogue.

A linear least squares fit to the data show that there is hardly a gradient between the

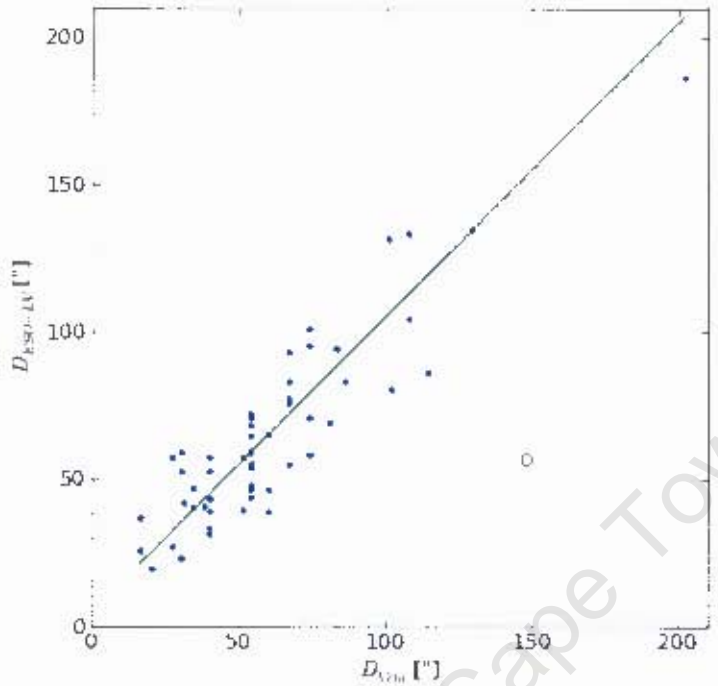

Figure 2.6: Comparison of Vela diameters to ESO-LV counterparts. The solid line shows the least squares fit for a slope of one and the dashed line for a optimal slope fit. The two lines are so close that they are indistinguishable. (The open circle marks the outlier excluded from the fit.)

two data sets, if the slope is left to vary:

$$D_{ESO-LV} = 0.999(0.004)D_{Vela} - 5.16(0.27) \quad (2.13)$$

$$\sigma_D = 15\farcs7. \quad (2.14)$$

A linear least squares fit with a fixed slope of one gives

$$D_{ESO-LV} = D_{Vela} - 5.09(0.13) \quad (2.15)$$

$$\sigma_D = 15\farcs7. \quad (2.16)$$

The correlation coefficient is $r = 0.92$ for the data, which shows a strong linear relationship as expected from a comparison diameters of ESO-LV counterparts in the Hydra-Antlia, GA and Crux regions (Kraan-Korteweg 2000, Woudt & Kraan-Korteweg 2001). It is clear that the deviation from a 1:1 fit is negligible, which is in excellent agreement with the findings for the GA, Crux and Hydra-Antlia regions where it was also found that the diameters share a diameter cut-off at the twenty-fifth magnitude isophote, D_{25}.

Comparison with Hydra-Antlia Catalogue

Figure 2.5 shows the location of the 19 counterparts in Hydra-Antlia catalogue in the Vela region (green crosses). Figure 2.7 is the comparison between the diameters of the counterparts in the two catalogues. The outlier at approximately $(D_{Vela}, D_{Hydra}) \approx (54'', 74'')$ is Vela3664 (ESO-LV 2630040, RKK1949) and is a very large galaxy which makes estimating the diameter, and indeed the magnitude, more difficult by eye.

The least squares fit gives,

$$D_{Hydra} = 1.25(0.02)D_{Vela} - 5.25(0.55) \quad (2.17)$$

$$\sigma_D = 6''.31. \quad (2.18)$$

For a fixed slope of unity the least squares fit gives,

$$D_{Hydra} = D_{Vela} + 0.21(0.23) \quad (2.19)$$

$$\sigma_D = 6''.85. \quad (2.20)$$

The comparison between the Vela and Hydra diameters is displayed in Fig. 2.7, the relation has a correlation coefficient of 0.90.

The scatter agrees with what Woudt & Kraan-Korteweg (2001) found when comparing the Crux region to the Hydra-Antlia region ($\sigma \sim 6''$).

Concern that the outlier was effecting the fit revealed that excluding it from the data and allowing the slope to vary gives,

$$D_{Hydra\ excl\ outlier} = 0.79(0.03)D_{Vela\ excl\ outlier} + 3.36(0.72) \quad (2.21)$$

$$\sigma_{D\ excl\ outlier} = 4''.64 \quad (2.22)$$

$$r_D = 0.78 \quad (2.23)$$

which shows that the large uncertainty of large diameter galaxies does effect the slope, because of the small number statistics at the high end.

The one-one trend is expected, but there are two few points to make any interpretations of the fit. The scatter agrees with the expected combined uncertainty of the Hydra-Antlia diameters and the measurements on the sky survey plate. It is worth noting that these galaxies are located on the edges of the plates where projections starts becoming non-linear, thus the here determined differences can be seen as an upper limit.

Internal Comparison

Figure 2.5 shows the 170 overlap galaxies in blue 'Y' symbols. Figure 2.8 is the comparison of the diameters of the same galaxies measured on overlapping plates. The correlation coefficient, $r = 0.86$, shows linearity of the data. A least squares fit of a line to the data

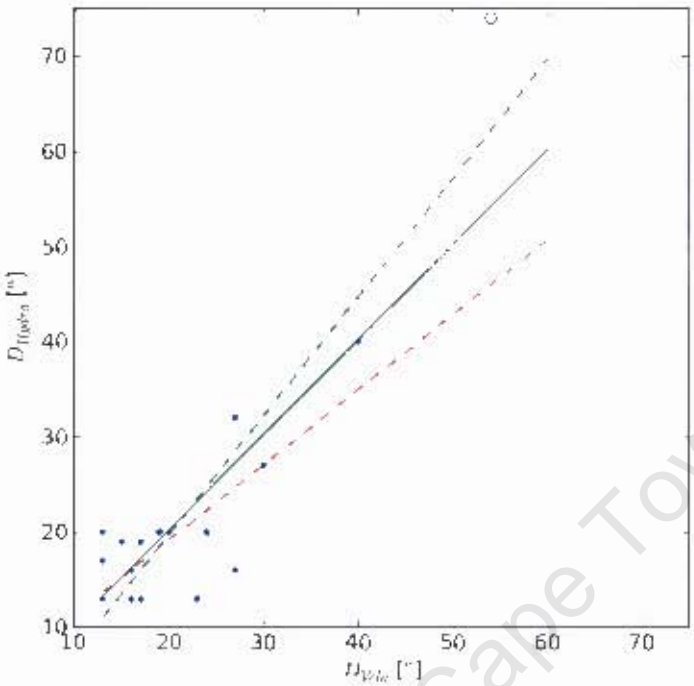

Figure 2.7: Hydra-Antlia Counterpart diameters compared to the Vela diameters. The dashed green line depicts the linear fit where the slope and the intercept were let free. The solid green line presents the linear fit, but with a fixed slope of 1.0. The red dashed line is the fit excluding the outlier at the top.

gives the result:

$$D_A = 0.908(0.006)D_B + 3.30(0.16) \quad (2.24)$$
$$\sigma_B = 6''.68. \quad (2.25)$$

A least squares fit of a line with a set slope of one gives a fit of:

$$D_A = D_B + 1.27(0.08) \quad (2.26)$$
$$\sigma_B = 6''.77. \quad (2.27)$$

The scatter is consistent with what was found by (Woudt & Kraan-Korteweg 2001) ($\sigma \sim 6''$) but more than (Kraan-Korteweg 2000) ($\sigma \sim 2''$) for internal checks.

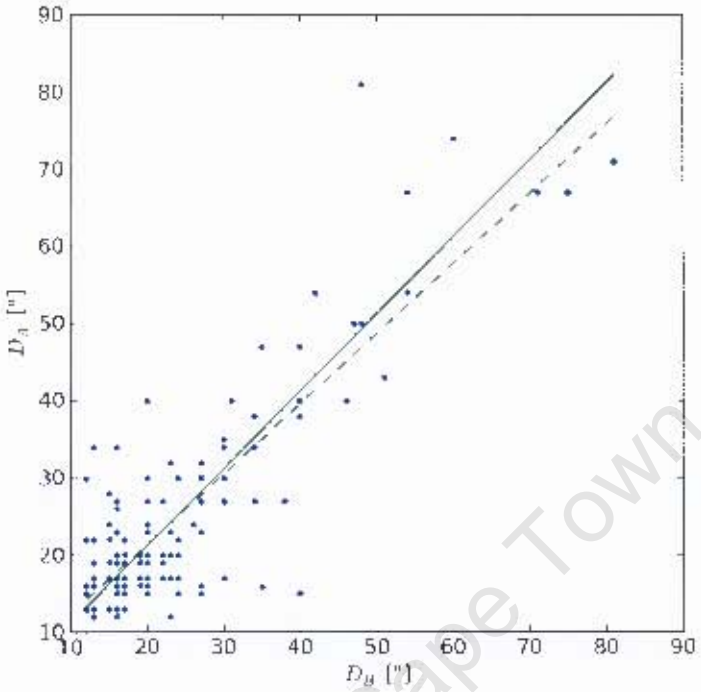

Figure 2.8: Diameter differences for internal counterparts on overlapping plates, the solid line is the line fit with a slope of unity and the dashed line is the line fit.

2.2.3 Magnitudes

How magnitudes are derived from surface density.

The magnitudes for the galaxies were obtained from the surface density (SD) of the emulsion on the photographic plates - the blacker the exposed photographic emulsion, the higher the intensity or flux. On the east and north-west edges of the plates are 7-step wedges that relate the surface density to log intensity (Table 2.2). Their calibration is given in the UK Schmidt Telescope Handbook (1983). An eye estimate was made between the finer-scaled, 21-step intensity-strip beside the milk glass screen (C in Fig. 2.2) and the blackness of the seven wedges on the east and north-west side of each plate. The relation between them is shown in Fig. 2.9. The top panel (a) shows the wedge estimates for all the individual plates, the bottom panel (b) shows the line fit between the surface density and the intensity, and also the averages between the east wedges of all the plates and average between all the north-west wedges. Experience has shown that the scatter is very big if magnitude calibration are made for each individual plate because the steps are quite rough. If the average of points is used, a more consistent magnitude is obtained (Kraan-Korteweg 2000). The advantage of using the finer intensity scale beside the milk glass is a more accurate magnitude. The derived and

Table 2.2: Intensity related to the 7-step wedges on the edges of the plates.

East $\log(I)$	North West $\log(I)$
1.49	1.52
1.35	1.35
1.19	1.19
1.00	1.00
0.79	0.78
0.56	0.55
0.36	0.32

henceforth adopted fit between intensity and 21-step surface density scale (bottom panel) is

$$\log(I) = 0.045 \text{ SD} + 0.437. \tag{2.28}$$

When galaxies are inspected on the plates, an eye estimate is recorded of the *average* surface density (blackness) over the whole extent of the galaxy, as well as the surrounding background on the scale of the 21-step intensity-strip beside the milk glass screen. This is straightforward for smaller galaxies whose surface brightness is usually quite smooth and constant over the extent of the galaxy. Estimating an *average* surface density for larger galaxies is more difficult, particularly starforming galaxies which show a lot of substructure, and therefore results, perhaps counter-intuitively, in a larger uncertainty. The relation (Eq. 2.28) between the logarithm of the intensity and the surface density is used to determine a flux intensity for the galaxies.

If individually sky-subtracted intensities are required, the following relation is used

$$\log(I_{IndSky}) = 0.045 \text{ (SD} - \text{SD}_{Sky}) + 0.437. \tag{2.29}$$

The area of the galaxy is given by

$$A = ab\pi = \frac{Dd\pi}{4}. \tag{2.30}$$

Where a is the semi-major axis of the galaxy, b is the semi-minor axis, D is the major diameter and d is the minor diameter.

We then use the equation

$$B = B_0 - 2.5(\log(I) + \log(A)) \tag{2.31}$$

to obtain the magnitude, where B_0 is the zeropoint.

For individually sky-subtracted magnitudes,we use the following calibration

$$B = B_{0,IndSky} - 2.5(\log(I_{IndSky}) + \log(A)) \tag{2.32}$$

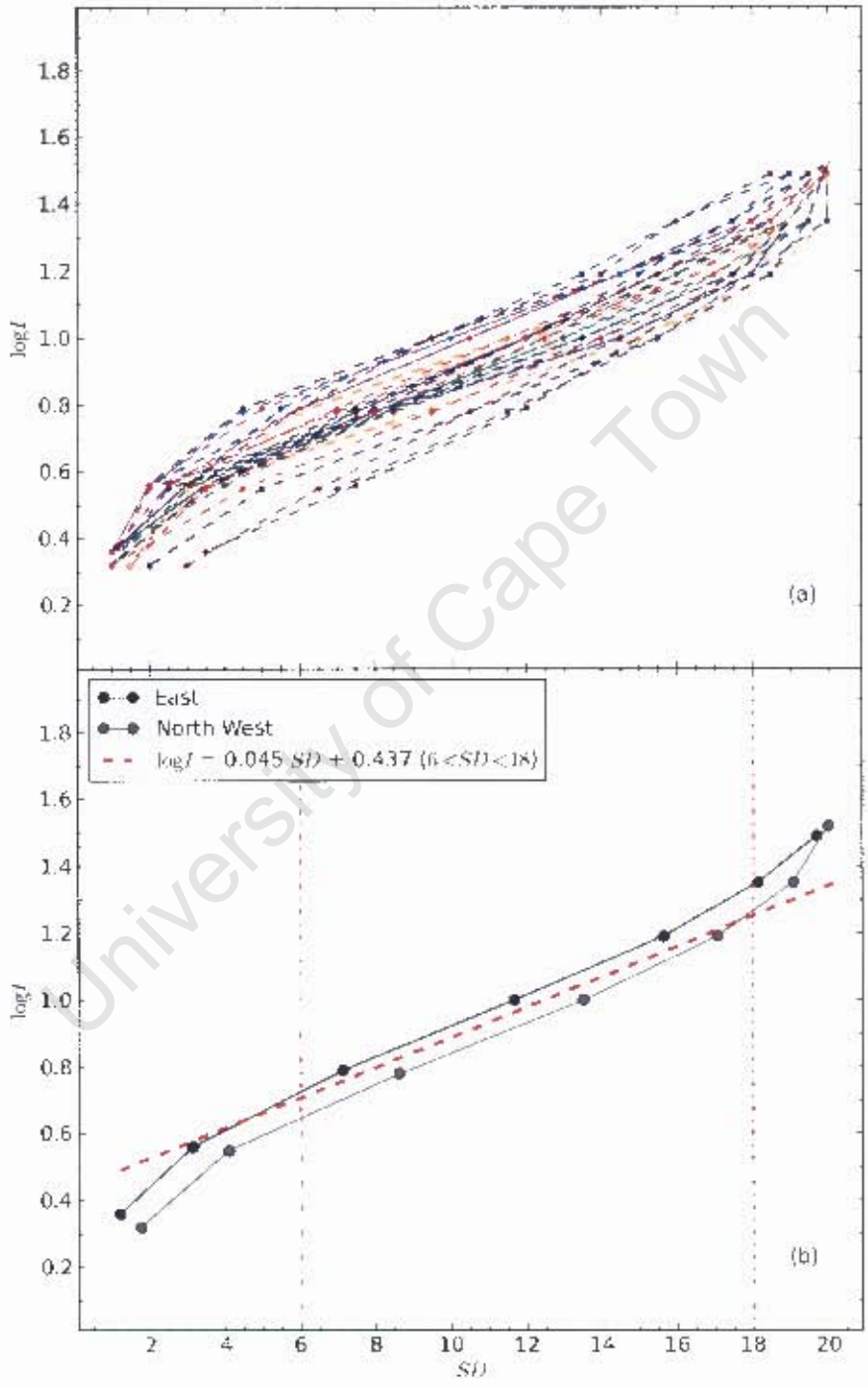

Figure 2.9: Intensity calibration with a linear fit to the wedge surface densities. Panel (a) shows all the intensity readings for the East and North West wedges. Panel (b) shows the linear fit to all the readings overplotted on the average of the East readings and the North West readings.

is used. where $B_{0.IndSky}$ is the zeropoint.

The zeropoints B_0 and $B_{0.\mathrm{skysub}}$ are derived in the next section.

Calibration with ESO-LV.

For the magnitude calibration I followed the same procedure as Kraan-Korteweg (2000) and Woudt & Kraan-Korteweg (2001). Calibration of the magnitude estimates, i.e. the determination of the zeropoints in Eq. 2.31 and 2.32, were done by comparing the Vela magnitudes to counterparts in the Lauberts catalogue[4]. In Eq. 2.31 an average sky background is assumed and therefore the background subtraction is accounted for in the zeropoint (B_0). In Eq. 2.32 the sky background, as measured around each individual galaxy, has been subtracted in the $\log I$ term. Both these methods are used to determine magnitudes to compare how much the small-scale sky background variations influence the outcomes.

The top panel (a) in Fig. 2.10 shows the resulting magnitudes for average sky-corrected magnitudes. The magnitudes from the two catalogues have a correlation coefficient of $r_B = 0.80$ indicating strong linearity. Two least-squares line fits are carried out, one with the slope left to vary (the dashed red line) and one with a fixed slope of unity (the solid blue line). The resulting fits are

$$B_{ESO-LV} = 0.81(0.11)B_{Vela(AveSky)} + 3.04(1.83) \quad (2.33)$$

$$\sigma_B = 0\overset{\mathrm{m}}{.}73, \quad (2.34)$$

and

$$B_{ESO-LV} = B_{Vela(AveSky)} + 0.02(0.13) \quad (2.35)$$

$$\sigma_B = 0\overset{\mathrm{m}}{.}75. \quad (2.36)$$

Where B_{ESO-LV} are the magnitudes for the galaxies from the Lauberts catalogue and $B_{Vela(AveSky)}$ are the average sky-corrected magnitudes calculated for galaxies in the Vela catalogue. The difference between the scatter are insignificant. We therefore use the fit with a slope of unity which gives the zeropoint $B_0 = 26\overset{\mathrm{m}}{.}1$.

The bottom panel (b) of Fig. 2.10 is the comparison of the individually sky background subtracted magnitudes with the B_{25} ESO-LV manitudes. The results of a least squares line fit are

$$B_{ESO-LV} = 0.78(0.11)B_{Vela(IndSky)} + 3.54(1.78) \quad (2.37)$$

$$\sigma_B = 0\overset{\mathrm{m}}{.}73 \quad (2.38)$$

[4]Counterparts are in Appendix A in table A.3.

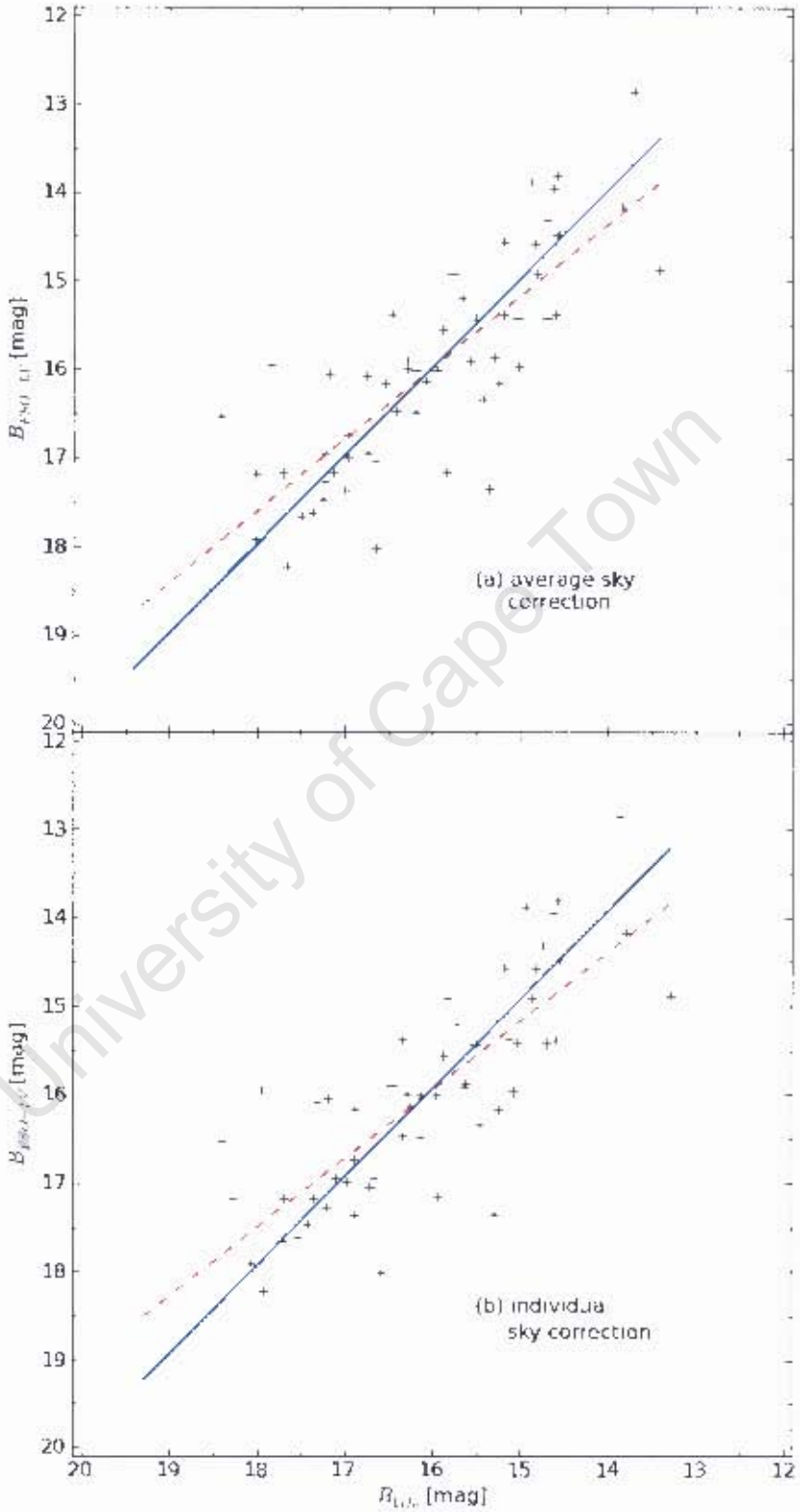

Figure 2.10: ESO-LV magnitudes of Vela counterparts. The solid line is a least square line fit with a fixed slope of unity and the dashed least square line fit with a free slope. The ESO-LV B_{25} magnitudes are compared to (a) the Vela magnitudes for average sky corrected magnitudes ($B_0 - 26.1^m$) and (b) individually sky background corrected magnitudes ($B_{0,IndSky} - 24.1^m$).

and

$$B_{ESO-LV} = B_{Vela(IndSky)} - 0.07(0.13) \quad (2.39)$$

$$\sigma_B = 0\overset{m}{.}79. \quad (2.40)$$

Where B_{ESO-LV} are the magnitudes for the galaxies from the Lauberts catalogue and $B_{Vela(IndSky)}$ are the individually sky-corrected magnitudes calculated for galaxies in the Vela catalogue. The correlation coefficient of these magnitudes is $r_B = 0.79$. The scatter of the fits are almost identical i.e. the dashed line and the solid (as in the top panel of the figure) have a difference of only $0\overset{m}{.}06$. A zeropoint of $B_{0,IndSky} = 24\overset{m}{.}1$ is determined.

The scatter in both the top and bottom panels of Fig. 2.10 are comparable, and fall within the expected combined uncertainty of the ESO-LV magnitudes, the galaxy areas measured used to calculate the Vela magnitude estimates as well as differences of measuring techniques and instruments.

Even though the Vela region is in the ZoA and hence small-scale background variations are expected to contribute to the magnitude, the difference between the magnitudes calculated using average and individual sky measurements is smaller than the uncertainty of the eye estimated magnitudes. We therefore use the average sky-corrected magnitudes for the catalogue, which also is consistent with the catalogues by Kraan-Korteweg (2000) and Woudt & Kraan-Korteweg (2001).

Comparison with Hydra-Antlia Catalogue

A comparison has been made between the observed magnitudes of the Hydra-Antlia and Vela catalogue counterparts (red 'x' symbols in Fig. 2.5). The correlation coefficient, $r = 0.79$, of these magnitudes shows a linear relationship. In Fig. 2.11 a least squares line fit is carried out. The fit with a varying slope gives

$$B_{Hydra} = 1.02(0.26)B_{Vela} - 0.68(0.55) \quad (2.41)$$

$$\sigma_B = 0\overset{m}{.}75 \quad (2.42)$$

and for a fit with a fixed slope of one the fit is

$$B_{Hydra} = B_{Vela} - 0.37(0.23) \quad (2.43)$$

$$\sigma_B = 0\overset{m}{.}75. \quad (2.44)$$

The outliers at the faint magnitudes are due to the magnitudes having been derived from the areas, and therefore diameters of the galaxies. When the diameters between Hydra-Antlia and Vela were compared (Fig. 2.7) there were some outliers at small diameters and therefore the scatter here is expected. The scatter in the magnitudes are comparable to the scatter seem between he magnitudes of ESO-LV and Vela.

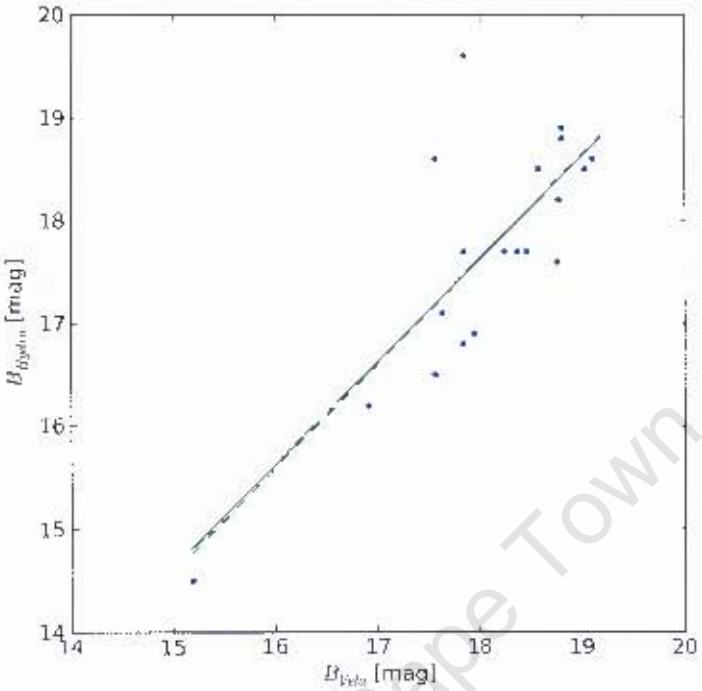

Figure 2.11: Hydra-Antlia magnitudes of Vela counterparts. The solid line is a least square line fit with a fixed slope of unity and the dashed least square line fit with a free slope.

Internal Comparison

Figure 2.12 is the comparison of the magnitudes of the same galaxies measured on overlapping plates. The correlation coefficient, $r = 0.85$, confirms linearity of the data. A least squares fit of a line to the data gives the result

$$B_A = 0.83(0.07)B_B + 2.90(1.22) \quad (2.45)$$

$$\sigma_m = 0\overset{m}{.}54 \quad (2.46)$$

$$(2.47)$$

for a fit with a varying slope. A least squares fit of a line with a fixed slope of unity gives

$$B_A = B_B \quad 0.02(0.08) \quad (2.48)$$

$$\sigma_B = 0\overset{m}{.}57. \quad (2.49)$$

The disribution is straight (within the scatter) over the whole magnitude range. The scatter is less between magnitudes from overlapping plates (internally) than seen between comparisons in the previous sections between Vela and Hydra-Antlia as well as Vela and

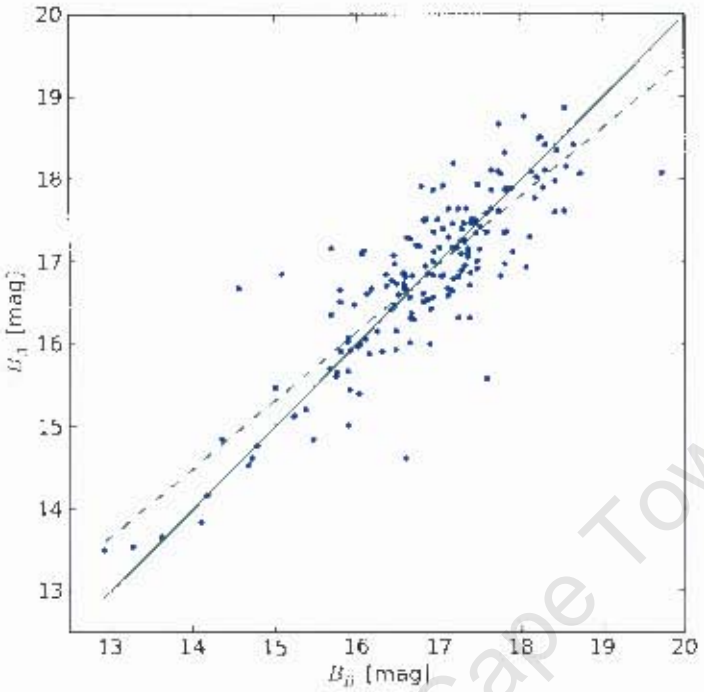

Figure 2.12: Magnitude differences for internal counterparts on overlapping plates. The solid line is a least square line fit with a fixed slope of unity and the dashed least square line fit with a free slope.

ESO-LV. This could be due to the galaxy magnitudes from this internal comparison having all been determined under the same conditions.

Table 2.3: Galaxy morphology

Main Type		Spiral Subtype		Inclination	
E	Elliptical	E	0/a-ab	E	Edge on
F	E/S0	M	b-d	N	Nearly edge on
K	S0/E	L	dm - Im	F	Face on
L	Lenticular			V	Nearly face on
SB	Barred Spiral				
S	Spiral				
I	Irregular				

The calibration of the Vela magnitudes and the subsequent comparison to the ESO-LV, Hydra-Antlia and internal magnitudes shows linearity over the whole magnitude range. The average scatter of the magnitude estimates is $\sigma \sim 0^m.75$ with the other catalogues and internally only $\sigma \sim 0^m.57$.

2.2.4 Morphology

Morphology classification is complicated by varying extinction. Due to the extinction, many low-surface brightness features are lost. Therefore what may be classified as an elliptical could very well be the bright bulge of an early spiral galaxy.

The morphology denotations are the same as used by Kraan-Korteweg (2000) and Woudt & Kraan-Korteweg (2001) and follows the RC2 (de Vaucouleurs et al. 1976) convention. With an additional code for spiral subtypes. Table 2.3 gives a complete description of the notation and in the catalogue each subtype is in a distinct column to avoiding confusion. The classifications are rough, reflecting the uncertainty in the determination of the morphology of galaxies where detail has been obscured.

The ratio of galaxy types for the Vela region is (E-S0 : S-I : Unclassified) = (6% : 74% : 19%). This result is very similar to that found for the Hydra-Antlia region (11% : 60% : 29%) and the GA-Crux regions (10% : 75% : 15%).

2.3 Sub-sample Integration

Out of the 4310 galaxies detected, 495 (11.5%) galaxies did not have parameters measured by Salem. The galaxy candidates with missing parameters were located on plates 209, 258, 262, 311, 314, 315 and 316. These are shown in red in Fig. 2.13.

Because the blinking machine (Fig. 2.2) has been relocated twice since Salem took the original measurements, the settings of the illumination are slightly different for the new measurements. For the sub-sample to be properly integrated into the main catalogue, a new calibration of the intensity scale, done in the exact same manner as presented in Sec. 2.2.3, was performed.

Figure 2.14 shows in top panel (a) the wedges for the seven individual plates, the bottom panel (b) shows the line fit between the surface density and the intensity, as well as the

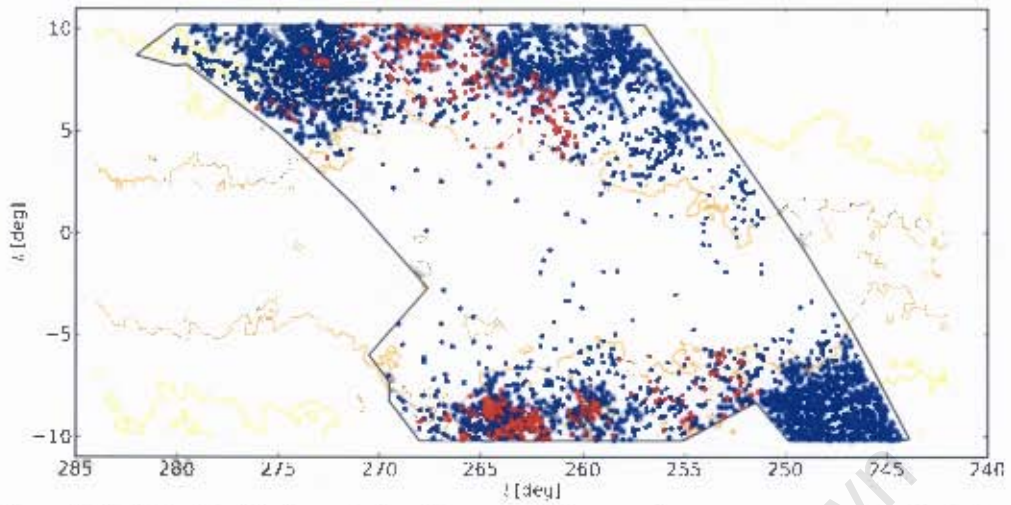

Figure 2.13: The distribution of the galaxy candidates with parameters recorded by Salem (blue) and those with parameters determined and calibrated by me (red).

averages between the east wedges of all the plates and average between all the north-west wedges. The derived and henceforth adopted fit between intensity and 21-step surface density scale (bottom panel) for the sub-sample is

$$\log(I) = 0.123\,SD + 0.736. \tag{2.50}$$

This relation between intensity and 21-step surface density scale is different from Eq. 2.28. This is expected since the blinking machine was moved between the first data capturing and the second, but (to be shown) after calibration the two samples result in a consistent dataset.

In the following subsections I will present first an internal check to test my own consistency. Secondly, the diameters are compared to those of the main catalogue. The magnitudes for the sub-sample are calibrated by comparison to the main catalogue. For both the comparison of the diameters and the magnitudes, the first ~ 50 galaxies that had parameters on each of the seven plates were remeasured by me (with the new settings).

Although the following discussion reveals that the new parameters are consistent with Salem's values within the quoted uncertainties those galaxies with parameters measured by me in this thesis are flagged in the final catalogue.

2.3.1 Consistency of parameters

Before starting to record the missing parameters, I first measured a random sample of 42 (big and small) galaxies three times to test my own consistency and train my eye to be as consistent as possible. This was done for plate 311.

The comparison of diameters are shown in the left panel of Fig. 2.15. A least squares fit

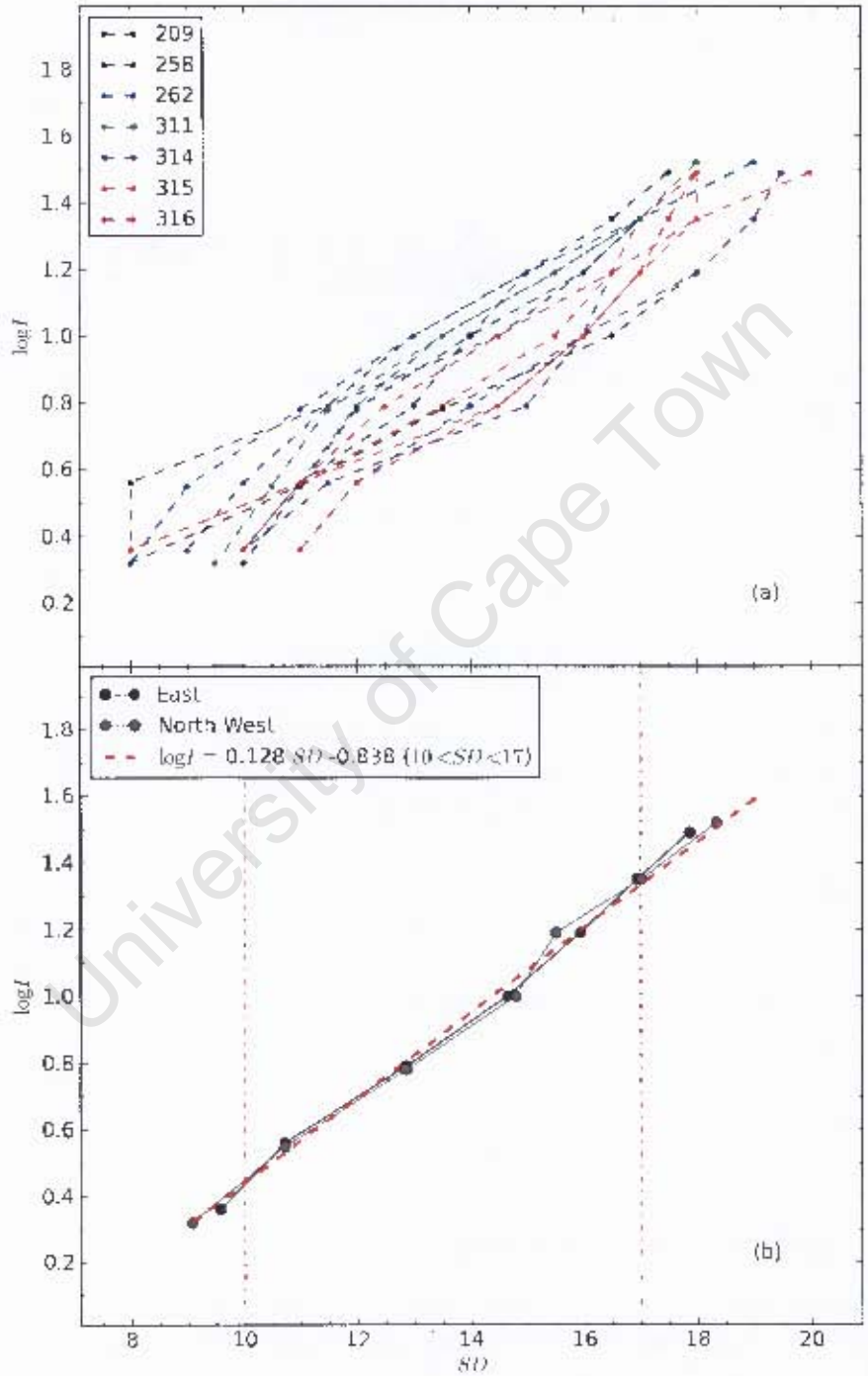

Figure 2.14: New Intensity calibration. Panel (a) shows all the intensity readings for the East and North West wedges. Panel (b) shows the linear fit to the average of the East readings and the North West readings.

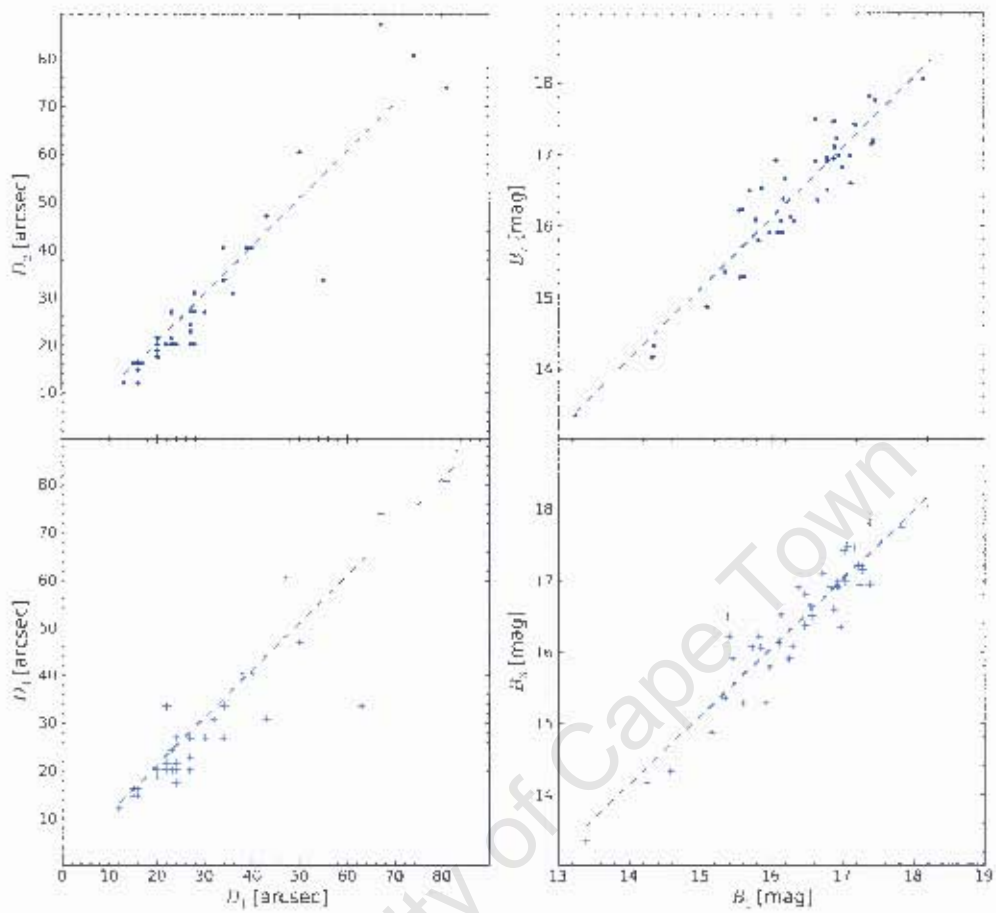

Figure 2.15: The differences in diameters (left) and magnitudes (right) measured three times for plate 311 to test consistency.

with a slope of unity is gives

$$D_2 - D_1 = 0.67(0.15) \quad (2.51)$$
$$\sigma_{12} = 6''.05 \quad (2.52)$$
$$r_{12} = 0.95 \quad (2.53)$$
$$D_3 - D_1 = 1.13(0.15) \quad (2.54)$$
$$\sigma_{13} = 6''.69 \quad (2.55)$$
$$r_{13} = 0.94. \quad (2.56)$$

The result has a scatter similar to the internal overlap galaxies in Sec.2.2.2.

The comparison of magnitudes are shown in the right panel of Fig. 2.15. A least squares

line fit gives

$$B_2 = 0.98(2.70)B_1 - 0.37(0.17) \quad (2.57)$$
$$\sigma_{12} = 0\overset{m}{.}36 \quad (2.58)$$
$$r_{12} = 0.93 \quad (2.59)$$
$$B_3 = 0.96(2.64)B_1 - 0.72(0.161) \quad (2.60)$$
$$\sigma_{13} = 0\overset{m}{.}37 \quad (2.61)$$
$$r_{13} = 0.93. \quad (2.62)$$

The scatter of $\sigma \sim 0\overset{m}{.}37$ is good in comparison to the scatter of $\sigma \sim 0\overset{m}{.}57$ found in the internal comparison of parameters in Sec. 2.2.3.

2.3.2 Diameters

Figure 2.16 show the comparison of the diameters. To check for deviations from plate to plate these evaluations were done for all plates individually. (The results for individual plates are shown in Fig. B.1 and B.2 in Appendix B.) While there is some variation from plate to plate, I find overall agreement between the parameters originally measured by Salem and those measured as part of this thesis.

The diameters of the two data sets have a correlation coefficient of $r = 0.88$. A least square line fit (dashed line) gives

$$D_1 = 0.71(0.00)D_2 - 3.43(0.11) \quad (2.63)$$
$$\sigma_D = 5\overset{''}{.}86. \quad (2.64)$$

A least square line fit with a fixed slope of one (solid line) gives

$$D_{Salem} = D_{New} - 3.72(0.06) \quad (2.65)$$
$$\sigma_D = 7\overset{''}{.}33. \quad (2.66)$$

The one-one relation describes the trend very well. As expected, the scatter is comparable to that found on overlapping plates in Sec. 2.2.2. Therefore the diameters of the sub-sample are comparable to the rest of the catalogue. It is worth reiterating that these galaxies are located on the edges of the plates where greater uncertainty is expected, thus these diameter differences can be seen as an upper limit.

2.3.3 Magnitudes

The equation

$$B = B_0 - 2.5(\log(I) + \log(A)) \quad (2.67)$$

is calibrated, hence the zeropoint determined by comparison to Salem's magnitudes.

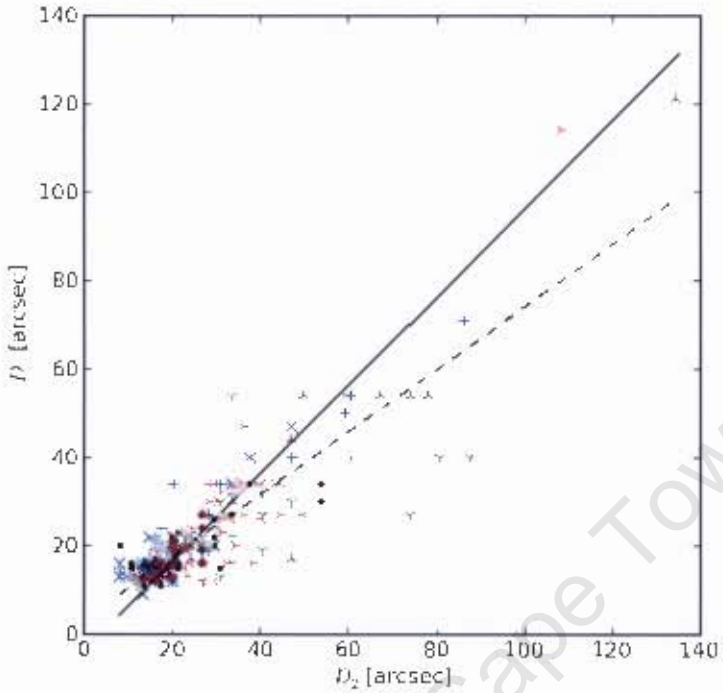

Figure 2.16: Diameter difference with a least square line fit (dashed line) and a least square fit with a fixed slope of one (solid line) to Plate 209, 258, 262, 311, 314, 315 and 316.

Figure 2.17 shows the comparison between observed magnitudes calculated in Sec. 2.2 and the remeasured magnitudes with the new settings. As for the diameters, the magnitudes were checked for all plates individually. (Appendix B presents the magnitude difference and least square fits to Plate 209, 258, 262 and 311 in Fig. B.3. Figure B.4 shows the magnitude difference and least square fits to Plate 314, 315 and 316, as well as the average fit combining all the plates.) Again there is some variation from plate to plate, but the overall agreement between magnitudes measured by Salem and those measured for this thesis is good.

The magnitudes of the two data sets have a correlation coefficient of $r = 0.81$. The least square line fit (dashed line) gives

$$B_{Salem} = 0.72(0.06)B_{New} + 4.83(0.94) \quad (2.68)$$

$$\sigma_B = 0^m.55. \quad (2.69)$$

A least square line fit with a fixed slope of one (solid line) gives

$$B_{Salem} = B_{New} + 0.01(0.06) \quad (2.70)$$

$$\sigma_m = 0^m.62. \quad (2.71)$$

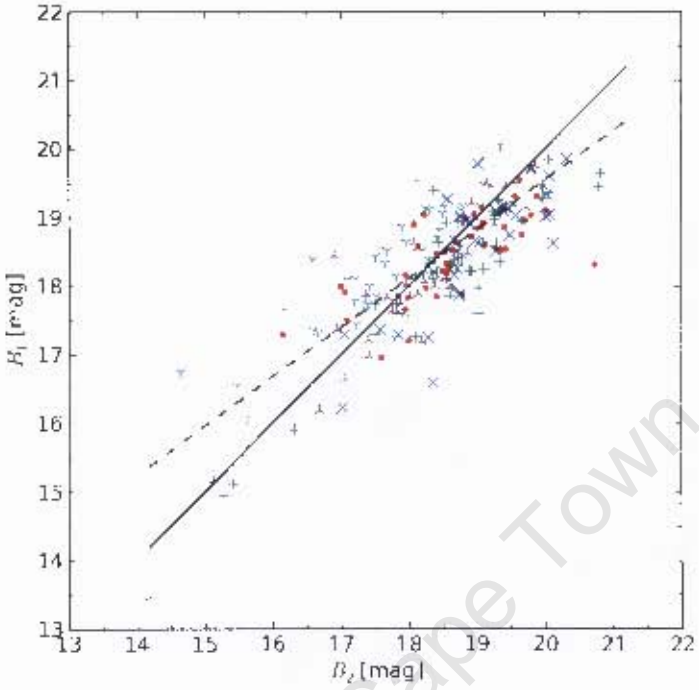

Figure 2.17: Magnitude difference with a least square line fit (dashed line) and a least square fit with a fixed slope of one (solid line) to Plate 209, 258, 262, 311, 314, 315 and 316.

The scatter is small and consistent with the other optical catalogues. It is often more difficult to estimate diameters and average brightness for larger galaxies. The displayed larger uncertainties for larger galaxies is not unexpected, in particular, for $B_J \lesssim 16^{\rm m}.5$.

2.4 Extinction corrections

The ZoA has varying degrees of extinction. Overall the extinction increases from the edges ($|b| \sim 10^{\circ}$) of the Galactic plane to the centre of the plane ($b = 0^{\circ}$). The distribution of dust is not homogeneous nor totally symmetric about the Galactic plane, with empty pockets such as the famous Baade's Window (Baade 1946) near the Galactic bulge giving a tantalizing hint of the hidden extragalactic sky, as well as dark clouds, and small-scale variations.

In the Vela region optically detected galaxies are traced down to $A_B = 3^{\rm m}$ (see Fig. 2.1), with only a handful detected at higher extinctions. This is consistent with the previous surveyed regions in the Southern ZoA, the Hydra-Antlia (Kraan-Korteweg 2000), GA and Crux (Woudt & Kraan-Korteweg 2001) regions.

The majority of the Vela region galaxy candidates lie between $1^{\rm m} \leq A_B \leq 3^{\rm m}$. To correct the magnitudes derived in Sec. 2.2.3 and 2.3.3 for Galactic foreground extinction we

use as a first approximation the DIRBE extinction maps by Schlegel et al. (1998). These have not been calibrated for $|b| < 5°$, but galaxies in the Vela region are mainly located between $5° < |b| < 10°$. The values for the reddening ($E(B-V)$) were downloaded from the NASA/IPAC Extragalactic Database[5]. The Galactic foreground extinction was determined following Cardelli et al. (1989),

$$A_B = 4.14 \cdot E(B - V). \tag{2.72}$$

Given that our diameters and magnitudes correspond to isophotal rather than total magnitudes, an additional correction is applied that accounts for flux loss from the low surface-brightness outer regions of galaxies as derived by Cameron (1990). Extinction causes the low-surface brightness edges of galaxies to be obscured completely such that the diameters are reduced, and in turn the magnitudes.

Dust extinction effects early type and late type galaxies differently. Spirals and ellipticals have different surface brightness profiles: ellipticals have surface brightness profiles that decrease as a function of $r^{1/4}$ and spirals have surface brightness profiles that decrease exponentially (Sparke & Gallagher 2007). Therefore spirals are more severely effected than spirals and therefore need to be treated differently from ellipticals. Galaxies with no morphological designation where assumed to be spirals, since late type galaxies are much more numerous than early type galaxies.

The reduction factor for observed (obscured) apparent diameters to the extinction-corrected (unobscured) diameters for extinction in the B-band according to Cameron (1990) is:

$$\frac{D^0}{D} = 10^{\alpha A_B^\beta}. \tag{2.73}$$

Spirals have coefficients $\alpha = 0.10 \pm 0.02$ and $\beta = 1.7 \pm 0.2$. Ellipticals and lenticulars have the coefficients $\alpha = 0.13 \pm 0.01$ and $\beta = 1.3 \pm 0.1$.

Magnitudes are reduced by a factor of

$$\Delta A = \phi A_B^\nu \tag{2.74}$$

over and above the value of A_B (Cameron 1990).

The coefficients for spirals are $\phi = 0.07 \pm 0.02$ and $\nu = 2.5 \pm 0.2$. Ellipticals and lenticulars have the coefficients $\phi = 0.08 \pm 0.0$ and $\nu = 1.8 \pm 0.2$.

It must be noted that for galaxies with large extinctions, $A_B \gtrsim 6\overset{\text{m}}{.}0$, this reduction factor grows too rapidly, not only overcompensating but becoming unreliable. Therefore an ad hoc cut-off for galaxies with extinctions greater than $A_B = 6\overset{\text{m}}{.}0$ was used for the calculation of both the extinction-corrected magnitudes and diameters. The galaxy candidates with $A_B > 6\overset{\text{m}}{.}0$ are very close to the Plane and mostly have some uncertainty of their galactic nature (green dots in Fig. 2.1).

[5] http://ned.ipac.caltech.edu/

Therefore the corrected magnitudes are given by

$$B^0 = B - A_B - \Delta A \text{ for } A < 6^{\mathrm{m}} \quad (2.75)$$

$$B^0 = B - A_B - \Delta A_{A=6} \text{ for } A \geq 6^{\mathrm{m}} \quad (2.76)$$

2.5 Catalogue Description

The Vela deep optical galaxy catalogue is given in the format shown in Table 2.4. A short description of each column is provided. The semi-colon ':' after a listed value indicates uncertainty in a measurement. The remarks in Column 20 are mostly self-explanatory, the most common abbreviations are listed in Table 2.5.

In Appendix A the catalogue itself is listed. Table A.1 gives the main catalogue for all galaxies with diameters greater than 12″ , Table A.2 lists the additional recorded galaxies with diameters smaller than 12″ .

Table 2.4: A short description of the entries in the catalogue.(Both Table A.1 and A.2)

Column		Description
1		Running number,ordered by RA (J2000)
2	α	Right Ascension (2000.0)
3	δ	Declination (2000.0)
4	l	Galactic longitude
5	b	Galactic latitude
6		Plate number
7	X	X-coordinate in mm as measured from centre of plate
8	Y	Y-coordinate in mm as measured from centre of plate
9		Flag for subsample N
10	D	Large diameter in arcseconds
11	d	Small diameter in arcseconds
12	A_B	Extinction in the B-band
13	D^0	Extinction corrected large diameter in arcseconds
14	B	Apparent magnitude
15	B^0	Extinction corrected isophotal magnitude
16		Uncertainty of extragalactic nature
17		Hubble Type
18		Hubble Subtype
19		Inclination
20		Number superimposed stars
21		Remarks (detailed in Table 2.5)

2.6 Chapter Conclusion

The Vela catalogue positional accuracy is 1.″2 in Declination and 1.″3 in RA. Comparison of diameters of Vela galaxy candidates with identified counterparts in the Lauberts and

Table 2.5: Explanation of common abbreviations in Column 20

Abbreviation	
* or **	star or stars
blg	bulge
br.	bright
nuc.	nucleus
cl.to br.*	close to bright star
dbl	double
diff.	diffuse
dist.	distinct
HSB	High surface brightness, vHSB for very HSB
LSB	Low surface brightness, vLSB for very LSB
neb?	nebula?
PN	Planetary Nebula
p.cov.by *	partly covered by star
poss.larger	possibly larger
struct.	structure

Hydra- Antlia catalogues show a scatter of 15.″7 and 6.″85 respectively. An internal analysis of diameters showed a scatter of 6.″8.

Vela magnitude estimates were calibrated by comparing magnitudes with identified counterparts in the Lauberts catalogue. The comparison of magnitude estimates with the Lauberts and Hydra catalogues both have a scatter of $\sim 0^{m}75$. Internal analysis shows a scatter of $0^{m}57$.

A sub-sample of 495 galaxy candidates' parameters were recorded under slightly different condition and were successfully integrated into the main catalogue.

Extinction corrections for both the diameters and magnitudes were done first by correcting for foreground extinction and then also correcting for loss of outer low surface-brightness features of galaxies by a reduction factor.

Chapter 3

Catalogue Discussion

This chapter presents a discussion of the Vela deep optical catalogue. In Sec. 3.1 the properties of the galaxy candidates are investigated, in particular how magnitudes and diameters are (a) distributed, (b) dependent on foreground extinction and (c) indicate completeness of the catalogue.

In Sec. 3.2 an analysis of the 2D distribution of galaxies is carried out in terms of different parameters for a first assessment of clustering and of LSS.

3.1 Properties of the Galaxies

3.1.1 Magnitude and diameter distribution

Figure 3.1 shows the distribution of the observed (top panel) and extinction-corrected (bottom) magnitudes (left) and diameters (right) of the 3922 galaxies with diameters greater than $12''$. The average observed diameter is $< D >= 20''$ and the extinction-corrected diameters is $< D^0 >= 53''$. The average observed magnitude is $< B >= 18\overset{m}{.}4$ and the extinction-corrected magnitude is $< B^0 >= 16\overset{m}{.}7$.

Table 3.1 shows the Vela properties with three other catalogues of this series i.e. for similarly detected, identified and measured galaxies, in the Hydra-Antlia (Kraan-Korteweg 2000), GA and Crux (Woudt & Kraan-Korteweg 2001) regions.

The Vela region on average has smaller diameters ($< D >= 20''$) than the other regions. The Vela region has a smaller stardensity than the other catalogues since it is further from the central bulge. Thus even though galaxies in the region have a higher average extinction $< A_B >= 1\overset{m}{.}48$ than e.g. in the Hydra-Antlia catalogue which has an average extinction of $< A_B >= 1\overset{m}{.}24$ (Kraan-Korteweg private communication), it is more 'transparent'. Therefore more galaxies closer to the limiting extinction level can be identified. It also contains many more small galaxies. This can be an effect of strong foreground extinction or an indication of distant overdensities. This is explored further in Sec. 3.2 and Chap. 4.

The average magnitude ($< B >= 18\overset{m}{.}4$) is similar the Hydra-Antlia and Crux regions,

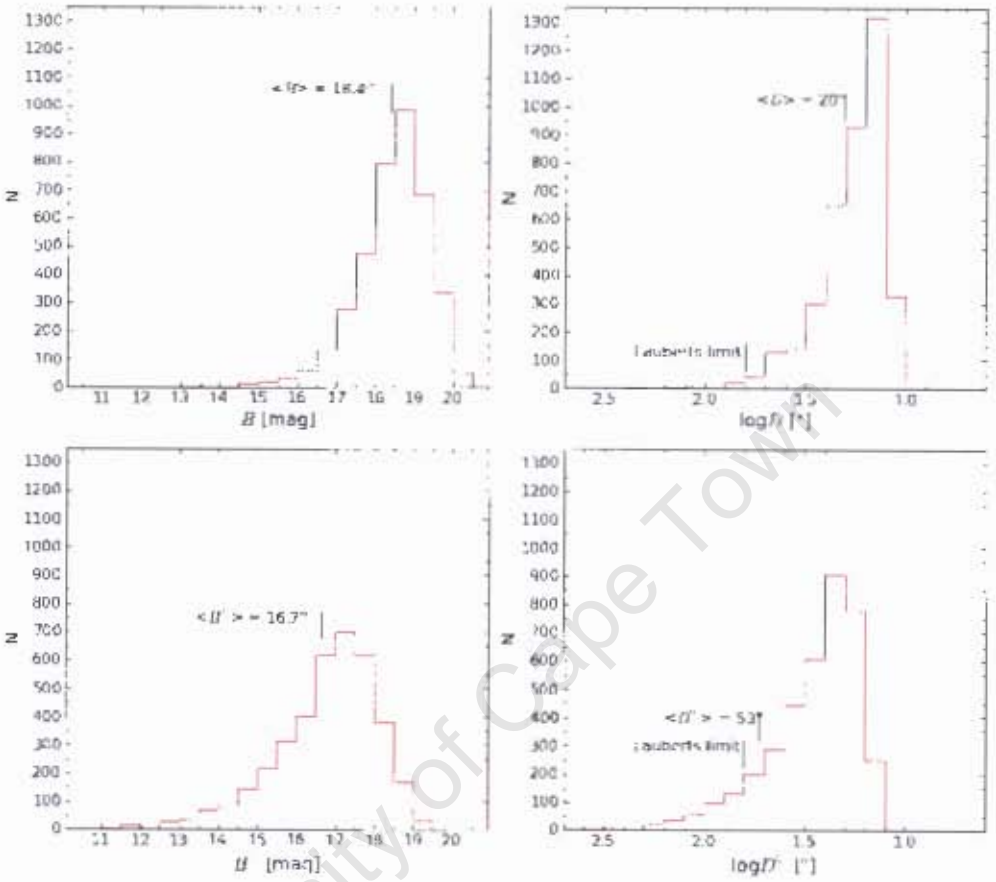

Figure 3.1: The distribution of the observed (top panels) and extinction-corrected (bottom) magnitudes (left) and diameters (right) of galaxies with diameters greater than 12″ .

Table 3.1: Comparison of the properties of optically detected galaxies in the Vela, Hydra-Antlia, GA and Crux regions.

	Vela	Hydra-Antlia	Crux	GA
Total ($D > 12''$)	3922	3279	3759	4423
$< A_B >$	1^m48	1^m27	1^m498	1^m22
$< D >$	20″	21″8	23″1	25″
$< D^0 >$	53″	34″7	41″	38″
$< B >$	18^m4	18^m2	18^m4	17^m5
$< B^0 >$	16^m7	16^m8	16^m4	16^m2
ESO-LV Counterparts	56 (1.4%)	97 (3.0%)	88 (2.3%)	108 (2.4%)
$D^0 > 60''$	490 (12.5%)	277 (8.4%)	593 (15.8%)	584 (13.2%)

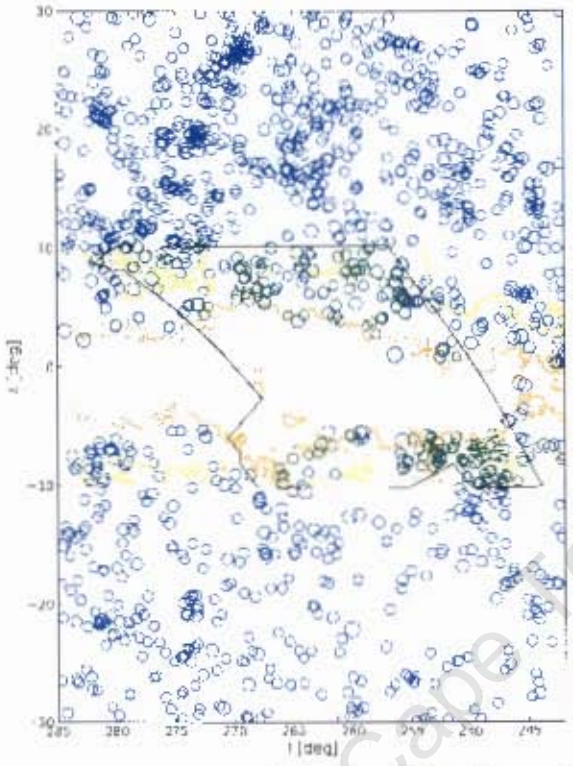

Figure 3.2: ESO-LV $D_{25} > 1.3'$ (blue) and Vela $D^0 \geq 1.3'$ (green).

but fainter than the GA region. This is expected for the GA region where the location of the nearby ($v \sim 4700 \mathrm{km\,s^{-1}}$) Norma cluster and GA-wall shifts the apparent magnitude distribution towards brighter magnitudes.

The average extinction-corrected diameter ($< D^0 >= 53''$) is much bigger than the other catalogues indicating more apparently small galaxies at higher extinction levels (as mentioned above). A total of 311 galaxies have extinction-corrected diameters greater than 13 (the Lauberts (1982) diameter limit). Therefore, in the absence of the ZoA, Lauberts would have detected significantly more galaxies than the catalogued 56 ESO-LV counterparts. These numbers show how incomplete the Lauberts catalogue is near the Galactic plane as well as the effectiveness of deep optical surveys in remedying this omission. Figure 3.2 shows how many more galaxies would have been found by Lauberts had it not been for the obscuration by the Milky Way.

3.1.2 Dependence on foreground extinction

Figure 3.3 shows the observed (top panel) and extinction-corrected (bottom), magnitudes (left) and diameters (right) of 4310 galaxies as a function of Galactic extinction ($E(B \quad V)$). The blue points indicate galaxies with $D \geq 12''$, green points indicate galaxy candidates (i.e. extended objects with uncertain natures) with $D \geq 12''$, and red points indicate galaxies

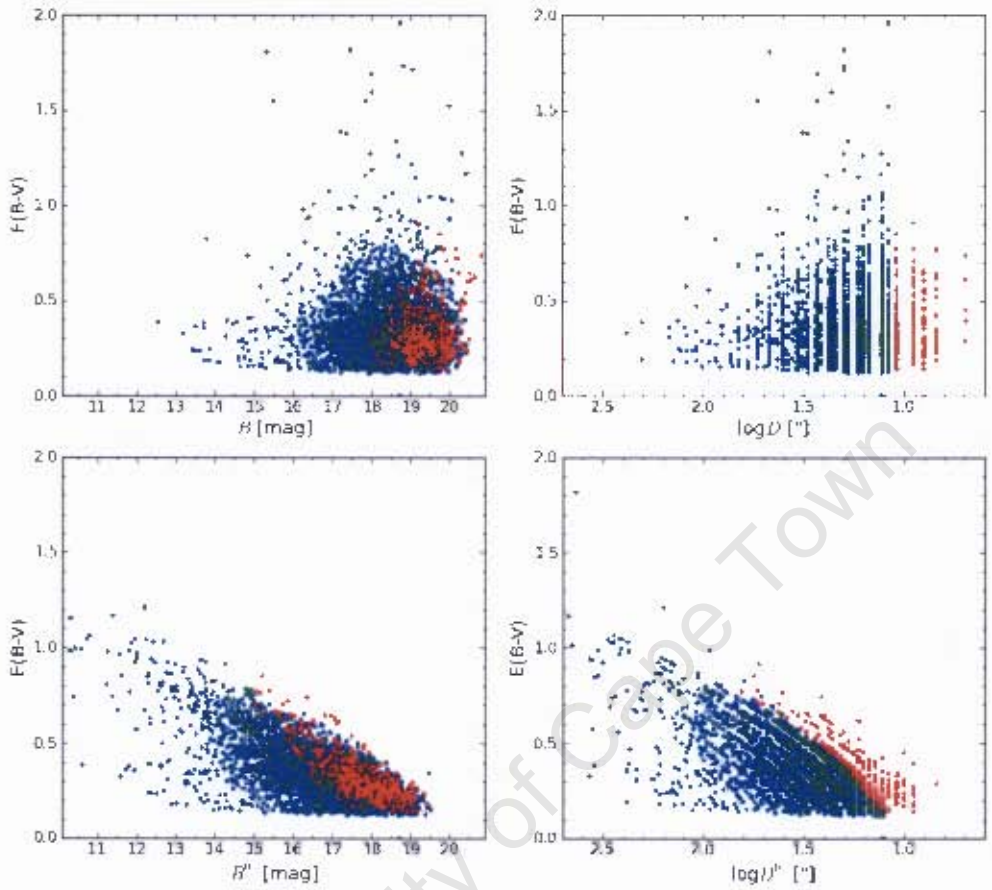

Figure 3.3: The distribution of the observed (top panels) and extinction-corrected (bottom) magnitudes (left) and diameters (right) of galaxies as a function of foreground extinction, $E(B-V)$. Blue indicates galaxies with $D > 12''$, green for galaxy candidates with uncertain natures with $D \geq 12''$ and red are galaxies with $D < 12''$.

parameters. This is comparable to the observed diameter and magnitude completeness limits for the Hydra-Antlia ($B = 18\overset{m}{.}5$ and $D = 14''$ for $A_B < 3^m$), Crux and GA ($B - 18\overset{m}{.}0 - 18\overset{m}{.}5$ and $D \approx 16''$ for $A_B \leq 3^m$) catalogues. However note when comparing the apparent diameter limits, the Vela catalogue has a lower diameter limit.

The bottom panel shows the cumulative number distribution of extinction-corrected magnitudes and diameters for the same extinction intervals. The completeness can again be read off where the linear increase flattens to a plateau for each extinction level. Here the turn-off is obviously correlated to the amount of extinction. At extinction levels $3^m < A_B \leq 4^m$ the catalogue becomes highly incomplete. Therefore for $A_B \leq 3^m$ the Vela catalogue is complete to $B^0 \approx 15\overset{m}{.}5$ and $\log D^0 \approx 1.6$ ($D^0 \approx 40''$). Comparison with the Hydra-Antlia ($B^0 \lesssim 15\overset{m}{.}5$ and $D^0 = 60''$ for $A_B < 3^m$), Crux and GA ($B^0 \lesssim 17^m$ and $D^0 \approx 20''$ for $A_B \leq 3^m$) catalogues shows a smaller diameter limit which is most likely to the region being

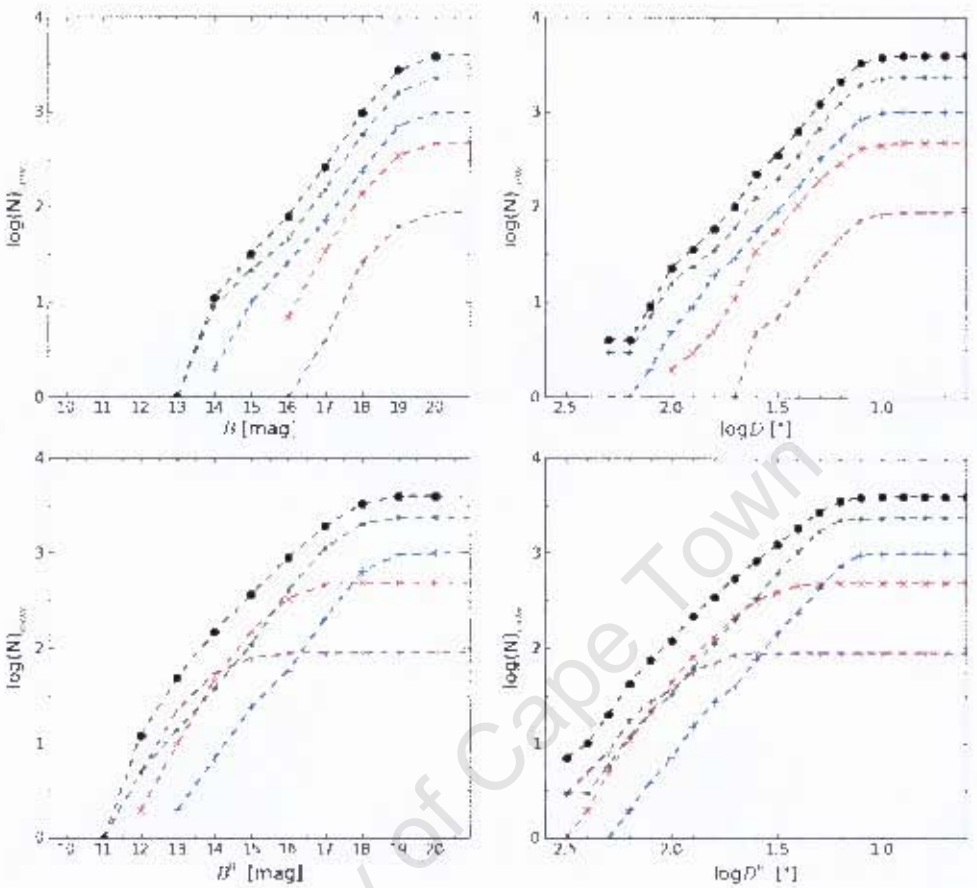

Figure 3.4: The distribution of the observed (top panels) and extinction-corrected (bottom) magnitudes (left) and diameters (right) of galaxies with diameters greater than $12''$. The different colours indicated galaxies than fall within different foreground extinction levels: black $A_B < 4^m$, green $A_B < 1^m$, blue $1^m < A_B < 2^m$, red $2^m < A_B \leq 3^m$ and magenta $3^m < A_B \leq 4^m$.

less star-crowded and therefore more 'transparent' to galaxies with smaller diameters.

3.2 First indications of structure

The on-sky positional (2D) distribution of the galaxy candidates in the Vela region can reveal first indications of LSS. Especially if we take parameters such as diameter (Sec. 3.2.1), morphology (Sec. 3.2.2) and magnitude (Sec. 3.2.3) into account. Each of these parameters trace LSS in some way and can be used as a rough first indication of structure (clusters, voids and approximate distance ranges), which can be used to plan follow-up observations.

3.2.1 Diameter distribution

Figure 3.5 shows the distribution of galaxy candidates with the size of the markers scaled in terms of relative diameter. Panel (a) shows the relative sizes of observed diameters across the Vela region with $D \geq 12''$. Panel (b) shows the relative sizes of extinction-corrected diameters for $D \geq 12''$. Comparing the top and middle panels it is clear that in higher extinction regions the intrinsically larger galaxies are observed. The orange contour is the $A_B = 3^{\rm m}$ extinction level. Note that galaxies at extinctions higher than the $A_B > 3^{\rm m}$ contour have been omitted since their diameters are over-corrected. (Some galaxies appear to be in $A_B > 3^{\rm m}$, but they are in small pockets of less obscuration.) There is some clumping of galaxies. For any further structure analysis only galaxies with $D \geq 12''$ will be regarded.

For completeness, Fig. 3.5 panel (c) highlights that the small galaxies ($D < 12''$) are prominent mostly at lower extinction levels. As such they are not a complete diameter sample. They also are more frequent in areas of apparent high density. These galaxies are not used in further structure analysis.

3.2.2 Morphology distribution

Figure 3.6 shows where the elliptical and spiral galaxies lie within the Vela region, as well as galaxies with unknown morphologies. Ellipticals are mostly found in high density environments and can be used for very rough indications of where clustering may occur. The elliptical galaxies seem strongly clustered in several areas. In particular two small clumps at $(l, b) \sim (273°, 8°), (274°, 8°)$, and another one on the opposite side of the Plane at $(l, b) \sim (264°, -8°)$ stand out. It is also worth noting the quite smooth or 'even' distribution in the area $245° < l < 250°$, $-10° < b < -8°$ which has a higher density than other areas of similar extinction (e.g. at higher longitudes and above the Galactic Plane).

The distribution of the more numerous spiral galaxies is evenly spread across the region though with some clear under-dense regions as well, especially where foreground extinction increases.

3.2.3 Two dimensional magnitude interval maps

I now investigate the LSS in the Vela region differently by looking at increasing extinction-corrected magnitude intervals. If, as a first approximation, we assume that all galaxies have the same luminosity, then galaxies of the same magnitude will be at the same distance, hence fainter galaxies will be more distant on average. For example, the same bright spiral or elliptical galaxy with an absolute magnitude of $M_B^* = -21^{\rm m}$ (Schechter 1976) will at $\sim 20\,000 {\rm km\,s^{-1}}$ have an extinction-corrected magnitude of $B^0 = 16^{\rm m}$ whereas at $\sim 8\,000 {\rm km\,s^{-1}}$ it would have an extinction-corrected magnitude of $B^0 = 14^{\rm m}$.

Figures 3.7 and 3.8 show panels of increasing magnitudes (decreasing brightness) in intervals of one magnitude. In Fig. 3.7: The galaxies with $B^0 \leq 15^{\rm m}$ i.e. the brightest galaxies in the catalogue are scattered across the whole region. This is expected since the intrinsically brightest galaxies will, although diminished in magnitude and diameter, still be

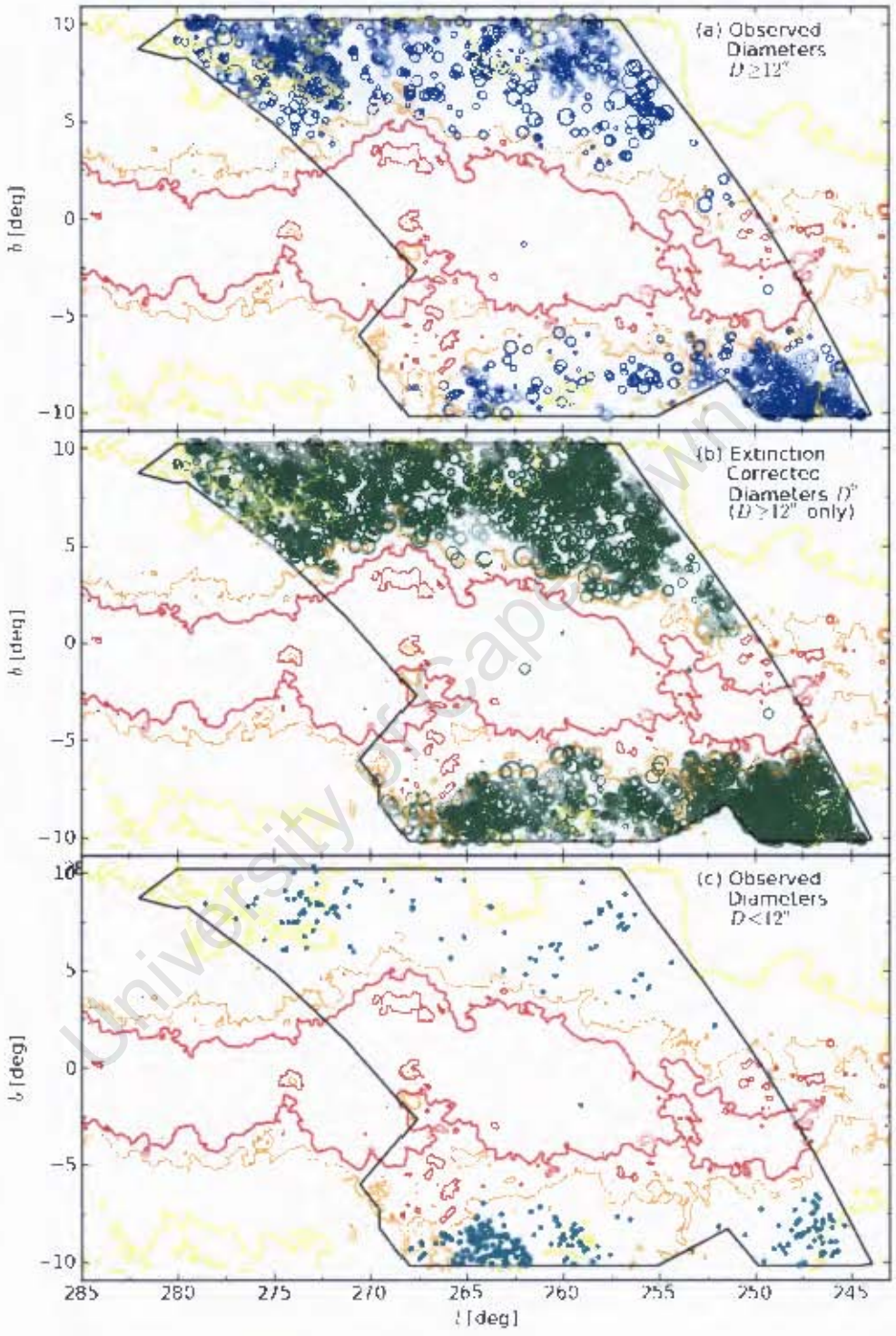

Figure 3.5: 2D Diameter distribution: Galaxy candidates with observed diameters (a) $D \geq 12''$ and (c) $D < 12''$. Frame (b) shows the extinction-corrected diameters for galaxies with apparent diameters $D \geq 12''$. The dust extinction contours are shown in red ($A_B = 5^m$), orange ($A_B - 3^m$) and yellow ($A_B = 1^m$).

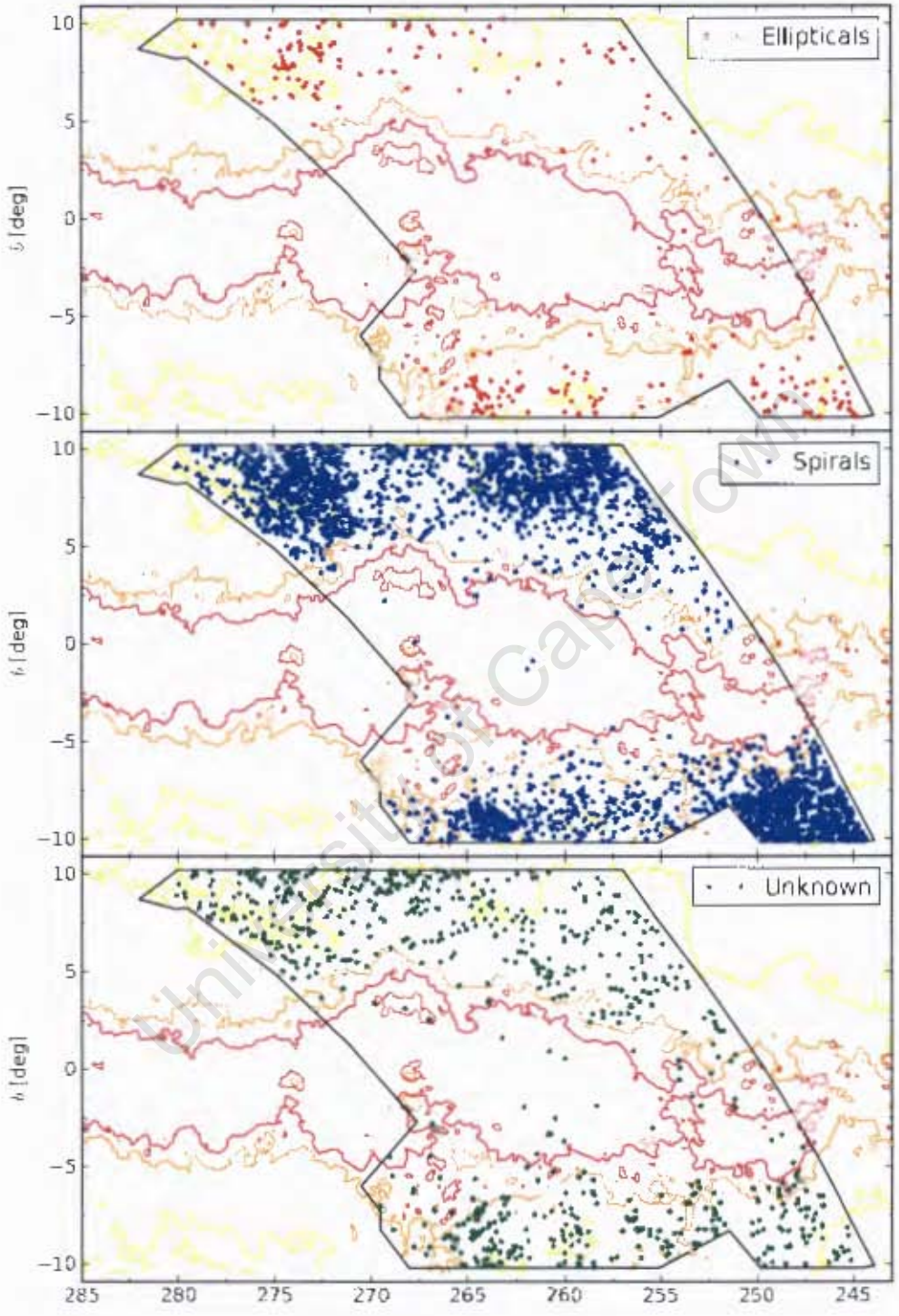

Figure 3.6: The distribution of the spiral (blue), elliptical (red) and unknown morphology (green) galaxies in the Vela region.

detected at higher extinction levels than their fainter counterparts. There is some apparent clumping at $(l, b) \sim (266°, -9°), (254°, -6°)$ and $(250°, -7°)$ below the Galactic Plane and another clump at $(l, b) \sim (269°, 7°5)$ above the Plane.

The next panel $15^{\rm m} < B^0 \leq 16^{\rm m}$ shows clumping in an area around $(l, b) \sim (248°, -7°)$ hinting at some nearby structure and this coincides with the even distribution of elliptical galaxies seen in top frame of Fig. 3.6. The galaxies with $16^{\rm m} < B^0 \leq 17^{\rm m}$ are spread quite evenly across the region.

In Fig. 3.8 the fainter magnitude intervals trace increasingly distant structure, but are hampered by the foreground extinction and thus appear more concentrated at lower foreground extinction regions. For $17^{\rm m} < B^0 \leq 18^{\rm m}$ there is apparent clustering at $(l, b) \sim (275°, 8°)$ across the $A_B = 1^{\rm m}$ extinction contour which coincides with the two clumps of elliptical galaxies in Fig. 3.6. At $(l, b) \sim (264°, -8°)$ a concentration of galaxies coincides with another elliptical clustering, and can be traced into the next frame where a a gap in the foreground extinction facilitates detection of the distant galaxies. The areas around $(l, b) \sim (264°, -8°)$ and $(245°, -9°)$ in the $17^{\rm m} < B^0 \leq 18^{\rm m}$ interval show a very high density of galaxies for $A_B > 1^{\rm m}$.

The galaxies with the faintest magnitudes, $B^0 > 18^{\rm m}$, appear in areas of least extinction where dim galaxies are less effected by foreground extinction and therefore more and more distant structures can be traced. The clumping at $(l, b) \sim (258°, 8°)$ has a high density of faint galaxies for $A_B > 1^{\rm m}$ where the rest of that extinction level is very sparsely populated.

3.3 Chapter Conclusion

The average diameter and magnitude in the Vela catalogue is similar to those of adjacent optical catalogues (Hydra-Antlia, Crux and GA; Table 3.1) with the greatest discrepancy being a larger than average extinction corrected average diameter. The distribution of optically detected galaxies in the Vela region follow the $A_B = 3^{\rm m}$ extinction contour of the ZoA well. The completeness of the catalogue as a function is comparable to the adjacent Hydra-Antlia catalogue.

The first indication of LSS in the Vela region can be seen particularly well by the clumping of the distribution of early type galaxies. Elliptical galaxies are mostly found in high density environments. Examination of extinction corrected magnitude intervals as a first approximation for distance intervals show promising hints of extended LSS especially the clustering in the $16^{\rm m} < B < 17^{\rm m}$ and $17^{\rm m} < B < 18^{\rm m}$ intervals.

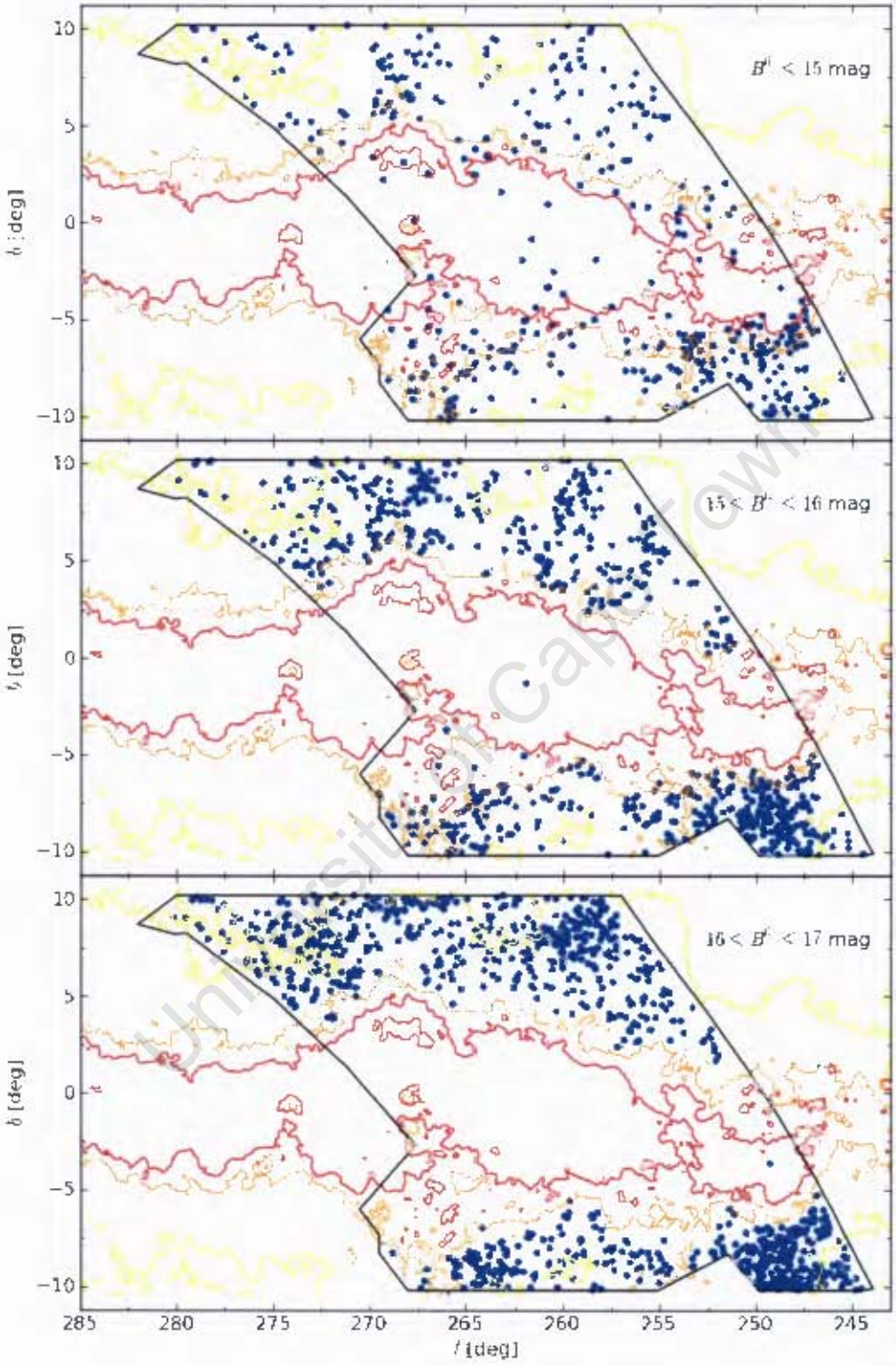

Figure 3.7: The blue dots are the positions of galaxies with extinction-corrected magnitudes less than $B = 15^{m}$ in galactic coordinates. The red, orange and yellow contours represent $A_B = 3^{m}$, $A_B = 2^{m}$ and $A_B = 1^{m}$ levels of extinction in the blue. The black outline describes the Vela region.

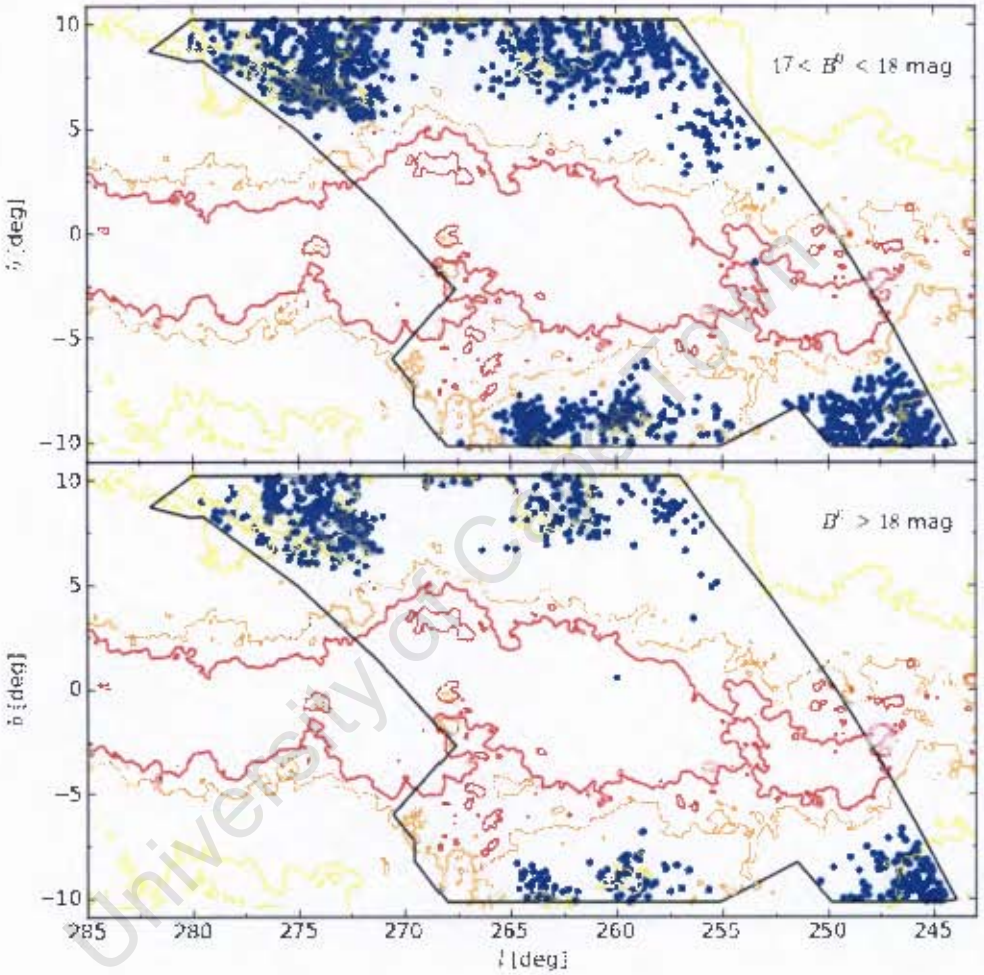

Figure 3.8: The blue dots are the positions of galaxies with extinction-corrected magnitudes greater than $B = 15^m$ and less than $B = 16^m$ in galactic coordinates. The red, orange and yellow contours represent $A_B = 3^m$, $A_B = 2^m$ and $A_B = 1^m$ levels of extinction in the blue. The black outline describes the Vela region.

Chapter 4

Redshift Survey

4.1 Introduction

The Vela deep optical galaxy catalogue provides an excellent basis for a redshift survey to fill in the missing LSS in the ZoA. Although, as seen in the previous chapter, the 2D distribution and accompanying parameter information can be used as a first indication of LSS, the best first proxy for distances are redshift measurements. A 3D-distribution (l, b, v) can be used to map the matter distribution in the Vela region which - with further analysis - can provide velocity flow maps of the region. In addition, this information can be added to the larger pool of known redshifts for a more complete all-sky picture of LSS and the dynamics in the local Universe.

Given that most of the galaxies in the ZOA are heavily obscured and previously uncharted, very few redshifts are known in this region compared to the rest of the sky. To trace the structures indicated in the Fig. 3.7 and 3.8, I did a small redshift survey with the grating spectrograph on the 1.9-m Radcliffe telescope in Sutherland. The aim of these observations were to complement the 6dF observations (shown in Sec. 5.1.1) which are confined to a small part of the Vela ZoA survey region. Even though it has a smaller aperture and a single slit, it is well suited to get good coverage by probing the region uniformly and following up on a few 6dF galaxies to confirm them, albeit being more sparsely sampled. Note that small aperture and old spectrograph does not allow to probe the faintest ($B \gtrsim 17\overset{\text{m}}{.}5$) and more distant ($v \gtrsim 10\,000$) galaxies.

After a general overview of spectroscopic observations in Sec.4.2, I will describe the data reduction and results of the 1.9-m observations in Section 4.3.

4.2 Spectroscopy

A redshift is obtained by observing a spectrum and measuring the shift, $\Delta\lambda$, in the absorption and/or emission lines from their known rest wavelengths, λ_0, as determined in the laboratory.

The redshift of a galaxy is defined as,

$$z = \frac{\lambda - \lambda_0}{\lambda_0} = \frac{\Delta\lambda}{\lambda_0} \tag{4.1}$$

where λ is the observed wavelength of the absorption/emission line and λ_0 is the rest wavelength of the line of the spectrum. The redshift is a measure of how the wavelength of light has shifted towards the longer, redder wavelengths due to motion of the source away from the observer or 'blue shifted' light for an approaching object. The red and blue shift of light is often interpreted as analogous to the Doppler effect, observed when sound waves are contracted or stretched due to the motion of the origin of the sound or observer.

The relationship between redshift and velocity is given by,

$$v = cz \tag{4.2}$$

where c is the speed of light.

In 1929 Hubble realized that the recession velocity of a galaxy is correlated to its distance. He found a linear relationship between distance (r) and velocity (v_H). This relationship, now called the Hubble law, is given as,

$$v_H = H_0 r \tag{4.3}$$

where H_0 is called the Hubble constant. It is now understood that the expansion of the Universe causes this observed recession velocity.

In addition to the expansion velocity, other factors may contribute to the observed radial velocity. A component is due to gravitational interaction with neighbouring galaxies. We observe velocity dispersion in groups ($\sim$150km s^{-1}; Abell 1975, Carroll & Ostlie 2007) and clusters ($\sim$800-1000km s^{-1}; Abell 1975, Carroll & Ostlie 2007), as well as large scale flows due to inhomogeneous mass distribution in the Universe (e.g. Peebles et al. 2001, Watkins et al. 2009, Feldman et al. 2010). This is called the peculiar velocity. Thus the radial velocity we observe is,

$$v = v_H + v_p \tag{4.4}$$

where v_H is the recession velocity and v_p is the peculiar velocity. This is especially important locally where v_H and v_p are of the same order of magnitude. v_p is usually hard to measure or correct for, we therefore use redshift space to map LSS. Thus redshift/velocity acts as a first proxy for distance and provides the third dimension to our on-sky positions of galaxies.

Spectra can be obtained with instruments through which light is dispersed with e.g. a prism or diffraction grating. The variation in the intensity of the light at different wavelengths gives the continuum shape, and the absorption and/or emission lines of a object. Both the shape of the continuum and spectral line strengths are dependent on the morphology of the galaxy. The location of line features provide redshift information. Typical absorption and emission lines in optical spectra of galaxies and their rest wavelengths in the

nearby Universe are listed in Table 4.1 and Table 4.2 (Fairall 1998). Both these tables have the name of the line in the first column and the rest wavelength in the second column.

Table 4.1: Typical absorption lines in galaxy spectra adopted from Fairall (1998).

Name	λ_0 [Å]
[CaII] (K)	3933.7
[CaII] (H)	3968.5
Hδ	4101.7
CaI	4226.7
G band	4304.4
Hγ	4340.5
Hβ	4861.3
MgI	5175.4
NaI (D)	5889.9
Hα	6562.8

Table 4.2: Typical emission lines in galaxy spectra adopted from Fairall (1998).

Name	λ_0 [Å]
[OII]	3727.3
[NeIII]	3869.7
[NeIII]+Hϵ	3970.1
[SII]	4068.6
[SII]	4076.2
Hδ	4101.7
Hγ	4340.5
[OIII]	4363.2
HeII	4685.7
Hβ	4861.3
[OIII]	4958.9
[OIII]	5006.8
[NII]	6548.1
Hα	6562.8
[NII]	6583.6
[SII]	6717.0
[SII]	6731.3

4.3 1.9m Radcliffe Telescope

In January 2010, observations were carried out over a period of two weeks with the 1.9-m Radcliffe telescope[1] at the South African Astronomical Observatory (SAAO) in Sutherland, South Africa. The single slit, grating spectrograph with the SITe CCD was used. The slit has a fixed angle and for maximum light capture a slit width of 300μm was used. Grating

[1] http://www.saao.ac.za/facilities/telescopes/19-m/

No. 7 was used for high dispersion (2.8Å/pixel) and tilted to an angle of 17.2° to cover the wavelength range of 3000 to 7500 Ångström. This wide wavelength range was chosen so that both the H and K lines, as well as the Hα line can potentially be identified. The SITe CCD has 266x1798 pixels.

Typical exposure times for galaxies were one to a few times 15 or 20 minutes. This is the maximum exposure time to avoid excess contamination from cosmic rays and saturation. Seeing was generally two arcseconds but could vary between one and five arcseconds. With 2 arcsecond seeing, a galaxy of $B \sim 16$ mag with 2x20 min exposures resulted in a S/N ratio of $\sim 6-7$.

Weather permitting, exposures of standard radial velocity stars were taken twice a night. Table 4.5 lists the standard stars that have been observed. The selected stars are very bright (5-8 mag) and their exposure times ranged between three and six seconds.

An arclamp exposure of 60 seconds was taken before and after each galaxy and standard radial velocity star exposure. Arclamp exposures are critical for wavelength calibration because of their well measured spectral features over range of 3500Å-7500Å (see Section 4.3.2). Arclamp exposures were done with a Copper Argon (CuAr) lamp.

Dome flat fields were taken every day (40 × 20sec exposures) to calculate the response function of the SITe CCD.

Of the two weeks of observing time allocated to this project, 51% of the time yielded good data. 49% of the time was lost due to bad weather conditions and technical problems. The majority of clear time was photometric.

4.3.1 Sample Selection

The observing sample was chosen from the Vela optical catalogue presented in Chapter 2. The aim was to get an uniform spread across the Vela region. Galaxies were selected from the optical catalogue that have (a) an apparent magnitude below of $B \leq 17\overset{\mathrm{m}}{.}5$ and (b) an extinction-corrected apparent magnitude below $B^0 = 16\overset{\mathrm{m}}{.}5$. The apparent magnitude cut-off was made due to the long exposure times required for fainter galaxies when using the 1.9-m telescope. Therefore only the brightest compact galaxies were chosen. Since spirals often have LSB disks the sample was dominated by spirals with prominent bulges and early type (E/S0) galaxies.

The apparent magnitude of a bright spiral or elliptical galaxy with an absolute magnitude of $M_B^* = -21^{\mathrm{m}}$ (Schechter 1976) behind 1^{m} of extinction in the B-band at $\sim 20\,000\mathrm{km\,s^{-1}}$ would be 17^{m}. The magnitude limits were also chosen with the aim of sampling the brightest galaxies at the distance of the unexpected overdensity found in the 6dF data, our limit should therefore *just* allow us to obtain redshifts for these galaxies.

The initial cutoff resulted in 714 candidates. This was reduced to 202 when a extinction-corrected apparent magnitude limit of $B^0 \leq 15^{\mathrm{m}}$ was applied. Galaxies previously observed in the 6dF fields were omitted from the observing list, except for four galaxies which were re-observed for comparison purposes.

The final observed sample comprised of 56 galaxies (Table 4.3). Figure 4.5 shows the distribution of observed galaxies across the Vela region. Table 4.4 shows the cross identification of the observed galaxies from other catalogues, as well as the 14 published velocities found in NED[2]. Galaxies with published velocities provided data to calibrate uncertainties in the velocity determination.

Table 4.3: Galaxies observed at SAAO.

Vela ID	l [deg]	b [deg]	Type	B [mag]	A_B [mag]	B^0 [mag]	Exp. Time [s]
23	245.17	-9.82	E	16.5	0.62	15.9	2x1200
71	245.18	-9.45	E	15.9	0.60	15.3	2x1200
115	247.41	-10.01	S	15.9	1.23	14.6	2x1200
168	246.38	-9.20	S	15.6	0.87	14.7	2x1200
173	256.59	3.23	S	16.1	1.73	14.1	2x1200
175	246.62	-9.30	F	15.3	1.01	14.3	2x1200
178	246.53	-9.25	S	15.9	0.93	14.9	2x1200
181	246.50	-9.22	S	16.3	0.92	15.3	2x1200
189	245.96	-8.93	F	16.4	0.77	15.6	2x1200
235	247.88	-9.58	S	16.3	1.23	14.9	1x1200
276	245.51	-8.10	S	15.5	0.79	14.7	2x1200
284	247.41	-9.03	F	16.8	1.52	15.1	2x1200
297	248.52	-9.52	S	14.7	1.26	13.3	1x1200
310	249.38	-9.88	F	15.0	1.46	13.4	2x1200
339	249.33	-9.88	S	15.0	1.51	13.3	1x1200
341	245.57	-7.78	S	14.8	1.03	13.7	1x1200
374	247.39	-8.53	E	16.1	1.10	14.9	2x1200
396	248.24	-8.84	S	14.8	1.76	12.8	1x1200
406	248.77	-9.08	F	15.8	1.71	13.9	1x1200
466	249.55	-9.01	E	16.7	1.62	14.9	2x1200
489	248.17	-8.22	E	16.6	1.24	15.3	2x1200
670	250.32	-8.31	S	16.7	1.65	14.8	1x1200
676	248.69	-7.44	S	14.4	1.61	12.6	2x1200
738	250.63	-8.00	S	17.3	1.94	15.0	2x1200
763	249.70	-7.57	E	16.4	1.80	14.4	1x1200
824	249.75	-6.80	S	17.2	2.60	13.9	2x1200
825	249.71	-6.77	S	17.0	2.58	13.7	2x1200
832	252.31	-8.11	S	17.3	2.06	14.8	2x1200
869	250.62	-6.85	S	17.5	2.40	14.5	2x1200
909	257.70	-10.14	S	16.3	1.37	14.8	2x1200

continued on next page...

[2]http://ned.ipac.caltech.edu/

Table 4.3 – continued

Vela ID	l [deg]	b [deg]	Type	B [mag]	A_B [mag]	B^0 [mag]	Exp. Time [s]
921	252.30	-7.04	S	17.6	2.87	13.7	2x1200
948	253.06	-7.10	K	16.6	2.73	13.0	2x1200
968	252.20	-6.36	S	18.0	2.72	14.4	2x1200
1001	253.68	-6.89	E	17.4	3.09	13.8	2x1200
1006	253.47	-6.73	S	17.4	2.89	13.5	1x1200
1007	253.47	-6.73	S	17.7	2.87	13.9	1x1200
1386	259.53	-6.34	S	16.2	1.90	14.0	2x1200
1463	265.97	-9.75	E	16.8	3.19	12.9	2x1200
1635	251.55	2.01	F	15.8	2.64	12.7	1x1200
1636	251.56	2.01	L	17.9	2.60	14.5	2x1200
1803	255.25	5.48	L	16.4	1.57	14.7	2x1200
1823	255.77	5.58	S	16.1	1.50	14.4	2x1200
1836	255.67	5.65	E	13.5	1.58	11.7	1x1200
1860	258.14	4.57	S	16.9	2.24	14.1	2x1200
1880	257.01	6.12	S	13.2	1.43	11.6	2x1200
1891	257.47	5.81	S	16.3	1.62	14.4	1x1200
2107	261.82	5.65	S	16.9	1.89	14.6	2x1200
2429	259.79	10.18	S	16.0	1.15	14.7	2x1200
2520	263.35	8.00	S	13.5	1.03	12.4	1x1200
2524	263.92	7.52	S	15.2	1.00	14.1	1x1200
2609	264.44	8.13	S	16.4	0.95	15.3	2x1200
2657	264.70	8.29	L	16.5	1.14	15.3	2x1200
2658	266.57	6.42	L	15.7	1.44	14.1	2x1200
3376	272.61	8.91	E	17.9	1.18	16.7	1x1200
3520	274.44	7.89	E	18.1	0.88	17.1	1x1200
3650	274.72	8.59	E	16.5	0.64	15.8	1x1200

Table 4.4: Cross-identifications and other published redshifts if available.

Vela ID	l [deg]	b [deg]	Cross ID	Velocity [km/s]	Reference
23	245.17	-9.82	2MASX J07153155-3303471		
71	245.18	-9.45	2MASX J07170726-3254197		
115	247.41	-10.01			
168	246.38	-9.20	NVSS J072045-335008		
173	256.59	3.23	FAIRALL 1146	9467 ± 75	Fairall (1988)
175	246.62	-9.30	PKS 0718-34	8500 ± 15	Collobert et al. (2006)
178	246.53	-9.25	2MASX J07204877-3400418		
181	246.50	-9.22	2MASX J07205431-3358308		
189	245.96	-8.93	2MASX J07205902-3321421		
235	247.88	-9.58	ESO 367- G 020		
276	245.51	-8.10	ESO 367- G 021		
284	247.41	-9.03			
297	248.52	-9.52	ESO 367- G 023		
310	249.38	-9.88	2MASX J07241276-3648420		
339	249.33	-9.88	ESO 367- G 024	3116	Crook et al. (2008)
341	245.57	-7.78	ESO 428- G 031	1915 ± 4	Theureau et al. (1998)
374	247.39	-8.53	2MASX J07254650-3426426		
396	248.24	-8.84	ESO 368- G 001	2861 ± 7	Theureau et al. (1998)
406	248.77	-9.08	2MASX J07262635-3554214	8815 ± 20	Yamada et al. (1994)
466	249.55	-9.00	2MASX J07282923-3633334		
489	248.17	-8.21	2MASX J07285196-3459058		
670	250.32	-8.31	2MASX J07331844-3654533		
676	248.70	-7.44	ESO 368- G 005		
738	250.63	-7.99	2MASX J07352639-3702267		

continued on next page...

Table 4.4 - continued

Vela ID	l [deg]	b [deg]	Cross ID	Velocity [km/s]	Reference
763	249.70	-7.57	2MASX J07350805-3601496		
824	249.75	-6.80	2MASX J07383700-3541587	8287	Crook et al. (2008)
825	249.71	-6.77	2MASX J07383791-3539137		
832	252.31	-8.11	2MASX J07385499-3833501		
869	250.62	-6.85			
909	257.70	-10.14			
921	252.30	-7.04			
948	253.06	-7.10	2MASX J07451544-3843199		
968	252.20	-6.35	2MASX J07462675-3736461	5773	Crook et al. (2008)
1001	253.68	-6.89	2MASX J07474884-3909277		
1006	253.47	-6.73			
1007	253.47	-6.73			
1386	259.53	-6.34	2MASX J08061128-4352169		
1463	265.97	-9.75	2MASX J08085396-5105056		
1635	251.55	2.01			
1636	251.56	2.01			
1803	255.26	5.48	ESO 371- G 008		
1823	255.77	5.59	2MASX J08451082-3354402		
1836	255.67	5.65	NGC 2663	2102 ± 26	de Vaucouleurs et al. (1991)
1860	258.14	4.57	2MASX J08482835-3623084		
1880	257.01	6.12	ESO 371- G 020	2368 ± 4	Theureau et al. (1998)
1891	257.47	5.81	ESO 371- G 021		
2107	261.82	5.65	2MASX J09043331-3829221	4805 ± 5	Fisher et al. (1995)
2429	259.78	10.18	ESO 372- G 010	2260 ± 45	Jones et al. (2009)
2520	263.35	8.00	NGC 2845	2530 ± 6	Bottinelli et al. (1993)

continued on next page...

Table 4.4 continued

Vela ID	l [deg]	b [deg]	Cross ID	Velocity [km/s]	Reference
2524	263.92	7.52	ESO 314- G 011		
2609	264.44	8.13	ESO 315- G 002		
2657	264.70	8.29	HIPASS J0924-38	4814 ± 9	Meyer et al. (2004)
2658	266.57	6.42	ESO 315- G 007		
3376	272.61	8.91	2MASX J09574119-4330074		
3520	274.44	7.89	2MASX J10021129-4524581		
3650	274.72	8.59	IRAS 10038-4446		

4.3.2 Data Reduction and Single Slit Analysis

IRAF reduction

The reduction of the raw data was carried out using the Image Reduction and Analysis Facility (IRAF)[3]. The reduction steps from the raw CCD image to a two dimensional, wavelength calibrated spectrum are outlined in detail in Appendix C.

Figure 4.1: The raw CCD image of galaxy Vela1836. The SITe CCD has 266×1798 pixels.

In brief the raw CCD image (Fig. 4.1) was first corrected for the CCD bias and the CCD response. The rows containing the galaxy spectrum as well as a few rows of the sky background spectrum were extracted. Once background subtracted, the arc spectrum (Fig. 4.2) was used to wavelength calibrate the spectrum. After which cosmic rays were removed, and for those objects with multiple exposures, the spectra were stacked.

Individual spectra are plotted in Appendix B.

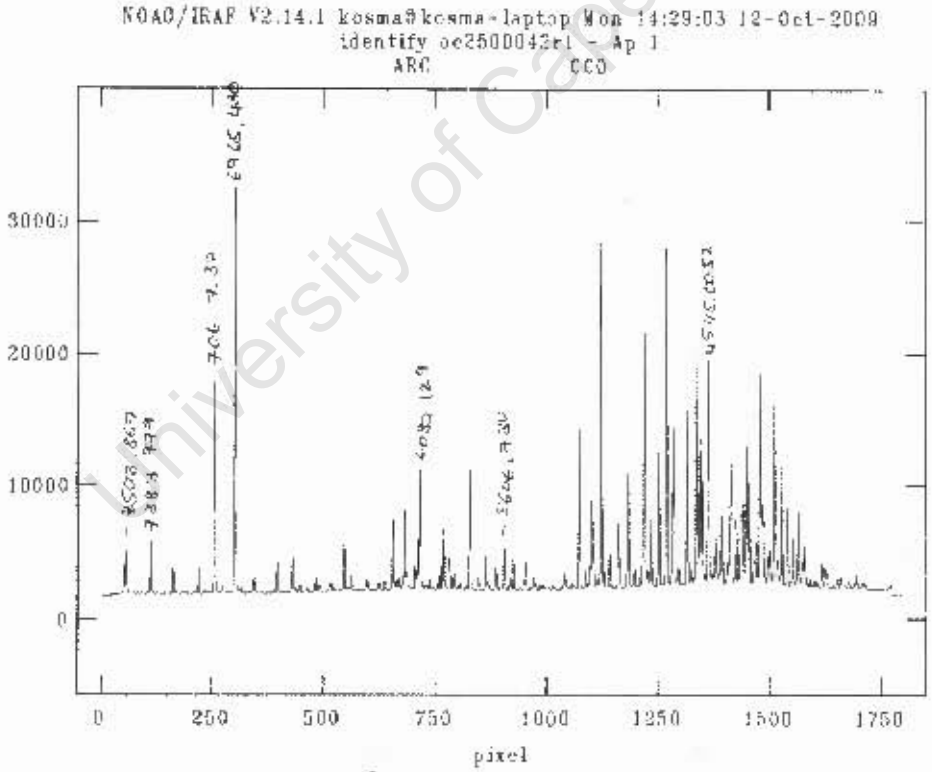

Figure 4.2: An example of a arc lamp spectrum used to relate pixel number to wavelength.

[3]IRAF is distributed by the National Optical Astronomy Observatories, which are operated by the Association of Universities for Research in Astronomy, Inc., under cooperative agreement with the National Science Foundation.

Cross-correlation for absorption line galaxies

The redshifts of the galaxies with absorption lines were determined by cross-correlation. With cross-correlations you compare positions of absorption and/or emission features in two spectra, of which one of the spectra has a known radial velocity. The difference leads to the velocity of the object with the unknown velocity. For the absorption galaxies observed, cross-correlation is done by using the standard radial velocity stars observed as templates. These stars have well determined radial velocities and clear spectral absorption line features. A typical radial star spectrum is presented in Fig. 4.3. The standard radial stars observed are listed in Table 4.5.

Table 4.5: Standard Radial Stars observed.

HD	RA [h m s]	Dec [d m s]	Spectral Type
24331	3 50 57	-42 31 57	K2.5V
48381	6 42 6	-33 28 49	K0IV
51250	6 56 36	-14 3 28	K2/K3III
83516	9 38 29	-35 7 28	G8IV

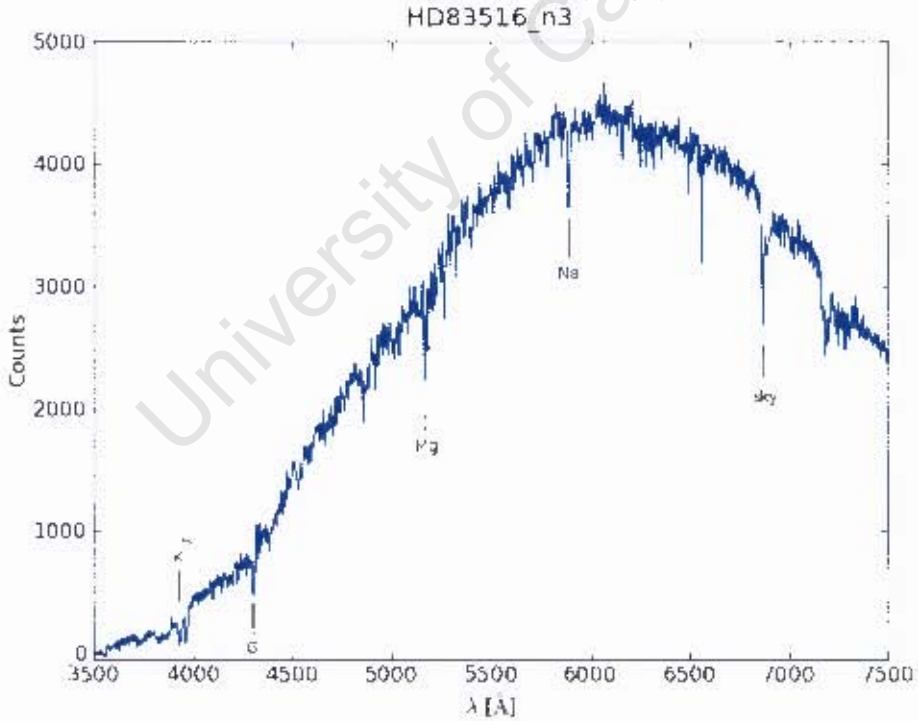

Figure 4.3: The spectrum of the velocity standard star HD83516 observed on night 3.

The IRAF task xcsao within the package rvsao (Kurtz & Mink 1998) was used to

calculate the recession velocities and their uncertainties of the galaxies.

Over the 2 week observing run two standard radial velocity stars were observed every night (when clear). The stellar spectra were used as templates for cross-correlation with the galaxy spectra.

To select the most reliable stellar spectra to use as templates, the following procedure was implemented. For N observed standard radial velocity stars, with known velocities, v_i

1. Each of the N stars were cross-correlated with the other $N-1$. Star i would then have $N-1$ velocities, $v_{calc,j}$. The difference, $v_{diff,i}$, between v_i and the average velocity,

$$v_{ave,i} = \frac{1}{N-1} \sum_{i \neq j} v_{calc,j}. \tag{4.5}$$

   was calculated for each star.

2. Step 1 was repeated for the M stars with the lowest $v_{diff,i}$. The $v_{diff,i}(M)$ for this smaller sample was averaged and the standard deviation, σ_M, was calculated.

3. For the final template sample, 10 of the 19 stars with $v_{diff,i}$ within $1.5\sigma_M$ were chosen.

All the galaxies were cross-correlated with the ten templates. Thirteen spectra were either very weak detections ($S/N < 4$) or so low S/N that they were discarded. Two galaxy spectra were contaminated with light from a nearby star.

Fit for emission line galaxies

The redshifts from emission lines were measured using the task `emsao` in the package `rvsao` of IRAF. `emsao` identifies individual line and gives their velocity. When the lines were too broad and overlapped at their bases, I used the `splot` task in the `noao` package to fit Gaussian curves to the peaks. Heliocentric correction were made. I then took the average of all the line velocities to calculate the galaxy's redshift.

Uncertainty analysis

The redshifts obtained by cross-correlation have a contrast factor, R (Tonry & Davis 1979). Woudt (1998a) shows how the velocity uncertainties obtained at the 1.9m Radcliffe relate to the R parameter. This curve is reproduced in Figure 4.4. It traces the upper limit to the velocity uncertainty for any given value of R. The red circles represent the difference between the newly determined and literature redshifts for six previously observed galaxies. Note that except for one outlier, they are all constrained to lie below the curve. The outlier is the elliptical galaxy Vela0178 which has been cross-identified with PKS 0718-34. The redshift was determined with a wide-beam radio telescope and the emission more likely originates from an adjacent spiral seen in the optical image.

The uncertainties of redshifts obtained from emission lines were calculated depending on the number of lines identified. An uncertainty of 100 km/s was assumed for a single line and if the number of emission lines was N the uncertainty was reduced by a factor of $1/\sqrt{N}$.

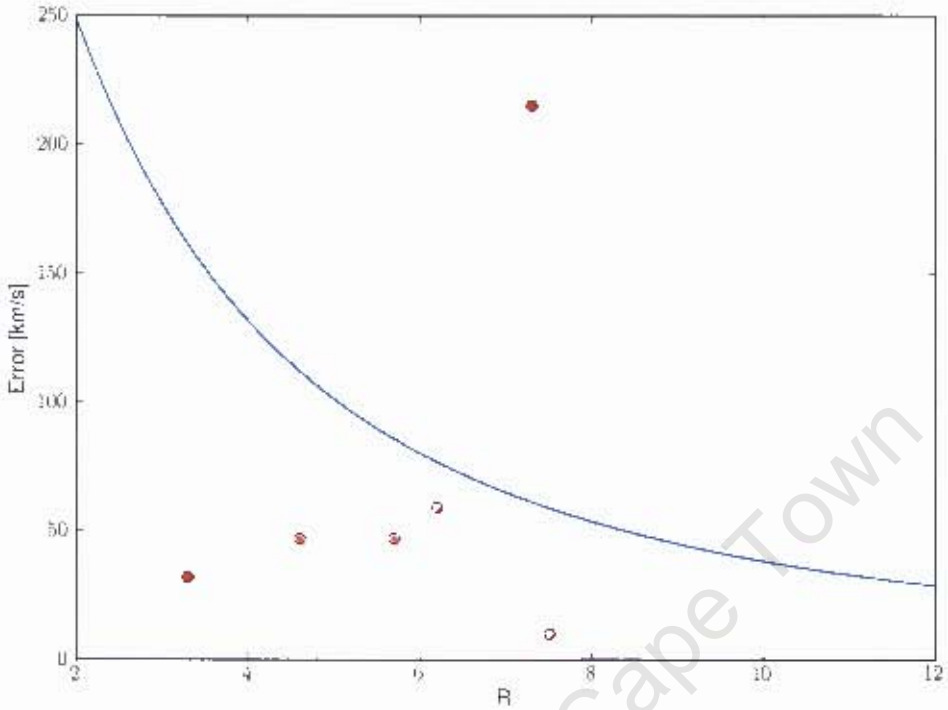

Figure 4.4: Relation between R and velocity uncertainty for the 1.9-m Radcliffe as determined by Woudt (1998a). The red dots indicate the difference between the SAAO redshifts and previously published redshifts determined by absorption features.

The uncertainties for redshifts obtained from emission lines are generally lower ($\sigma_{em} \sim 50 \mathrm{km\,s^{-1}}$) than uncertainties for redshifts obtained from absorption lines ($\sigma_{ab} \sim 150 \mathrm{km\,s^{-1}}$). This is due to emission lines by nature being sharper and clearer whereas absorption lines for galaxies are generally broadened and less pronounced.

4.3.3 Results

Table 4.6 lists the obtained redshifts. The morphology and magnitude of each galaxy is also indicated, as well as whether emission or absorption lines were used for the redshift calculation. Figure 4.5 shows the distribution of the 56 galaxies observed. The spectra resulted in 41 redshifts (circles), 2 star contaminated spectra (stars) and 13 non-detections (crosses).

Table 4.7 lists the two galaxies with star contaminated spectra. Table 4.8 lists the galaxies observed that did not have sufficient S/N to show any spectral line features.

A comparison between the redshifts obtained during this observing run and those in the

Table 4.6: Redshift results from SAAO observations.

Vela ID	Absorption [km/s]	Emission [km/s]	Literature [km/s]
23		10432 ± 58	
71		2321 ± 38	
168	8745 ± 163		
173		9524 ± 33	9467 ± 75
175	8715 ± 100		8500 ± 15
178	9236 ± 173	9278 ± 100	
181	8827 ± 116		
189	8612 ± 197		
235	8417 ± 216	8365 ± 71	
276	8691 ± 81		
297	8715 ± 153		
310	2812 ± 120		
341		1976 ± 50	1915 ± 4
374	9864 ± 123		
396		2888 ± 45	2861 ± 7
406		8907 ± 33	8815 ± 20
466	9329 ± 223		
489	1077 ± 163		
670	7096 ± 112		
676	8379 ± 134		
763		1499 ± 50	
948	2932 ± 156		
1001	5882 ± 181		
1386		11365 ± 35	
1463	8400 ± 244	8258 ± 71	
1803	2387 ± 114		
1823	2117 ± 138		
1836	2043 ± 114		2102 ± 26
1860		10973 ± 58	
1880	2400 ± 183		2368 ± 4
1891	1965 ± 133		
2107		4804 ± 38	4805 ± 5
2429	2250 ± 97		2260 ± 45
2520	2483 ± 122		2530 ± 6
2524	5078 ± 116		
2609	4817 ± 98		
2657	4767 ± 143		4814 ± 9
2658	4963 ± 147		
3376	11279 ± 178		
3520	19709 ± 154		
3650		4001 ± 41	

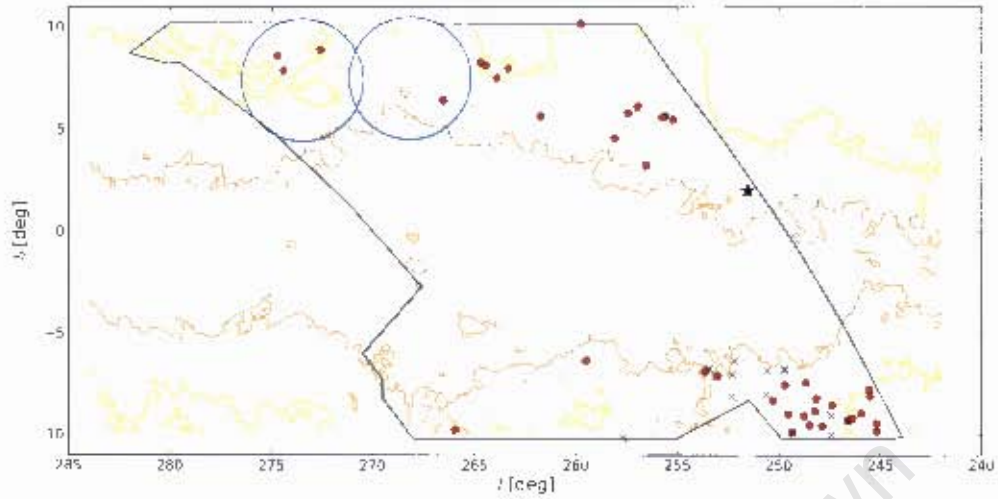

Figure 4.5: The figure shows the distribution of galaxies observed at SAAO. The red circles indicate observations that resulted in confirmed redshifts, the crosses indicate non-detections and the stars are galaxies whose spectra were star contaminated. The two blue circles indicate where the two ZoA 6dF fields lie (see Sec. 5.1.1).

literature describe a linear relationship with a slope of unity and no significant scatter.

$$v_{LIT} = v_{SAAO} - 30.5(0.3) \quad (4.6)$$

$$\sigma_v = 75.3 \mathrm{km\,s^{-1}} \quad (4.7)$$

$$r_v = 0.9998 \quad (4.8)$$

Table 4.7: Galaxies that have star contaminated spectra.

Vela ID	l	b
1635	251.55	2.01
1636	251.56	2.01

4.3.4 Special Cases

Several of the spiral galaxies display characteristics of having active nuclei, in particular those of Seyfert galaxies. Seyfert galaxies are active galaxies and are characterized by the presence of strong emission lines originating from ionized hydrogen, helium, nitrogen and oxygen. Two types are recognized. Type 1 have broad hydrogen, helium and nitrogen lines and narrow forbidden lines such as oxygen. Type 2 Seyfert galaxies exhibit only narrow lines (Carroll & Ostlie 2007). Figures 4.6 and 4.7 show the two examples of the (non-flux calibrated) spectra of Seyfert 1 candidate galaxies.

Table 4.8: Galaxies that were non-detections.

Vela ID	l	b
115	247.41	-10.01
284	247.41	-9.03
339	249.33	-9.88
738	250.63	-7.99
824	249.75	-6.80
825	249.71	-6.77
832	252.31	-8.11
869	250.62	-6.85
909	257.70	-10.14
921	252.30	-7.04
968	252.20	-6.35
1006	253.47	-6.73
1007	253.47	-6.73

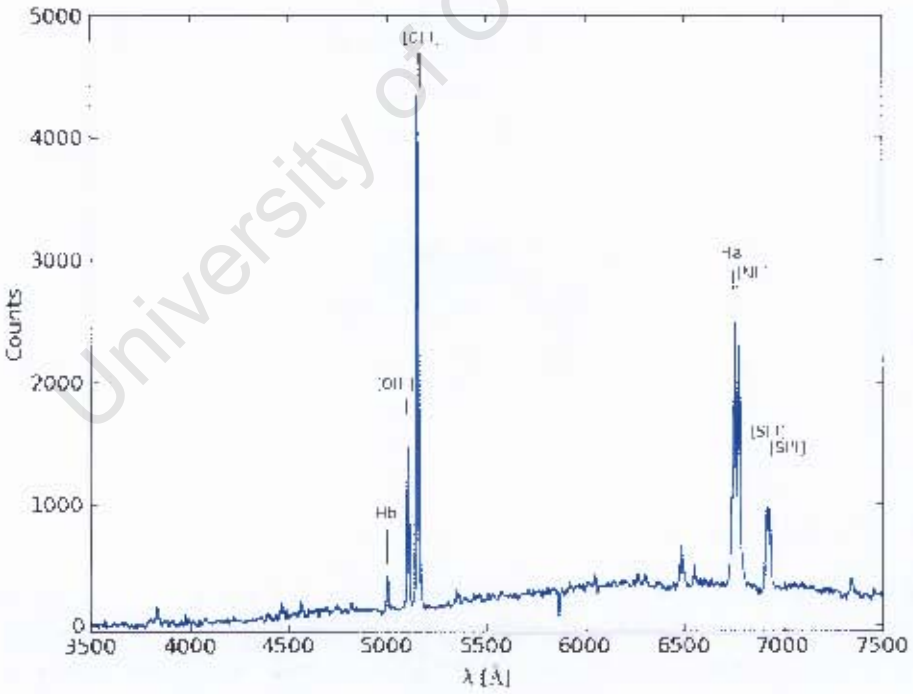

Figure 4.6: Spectrum of a Seyfert galaxy candidate, Vela0406.

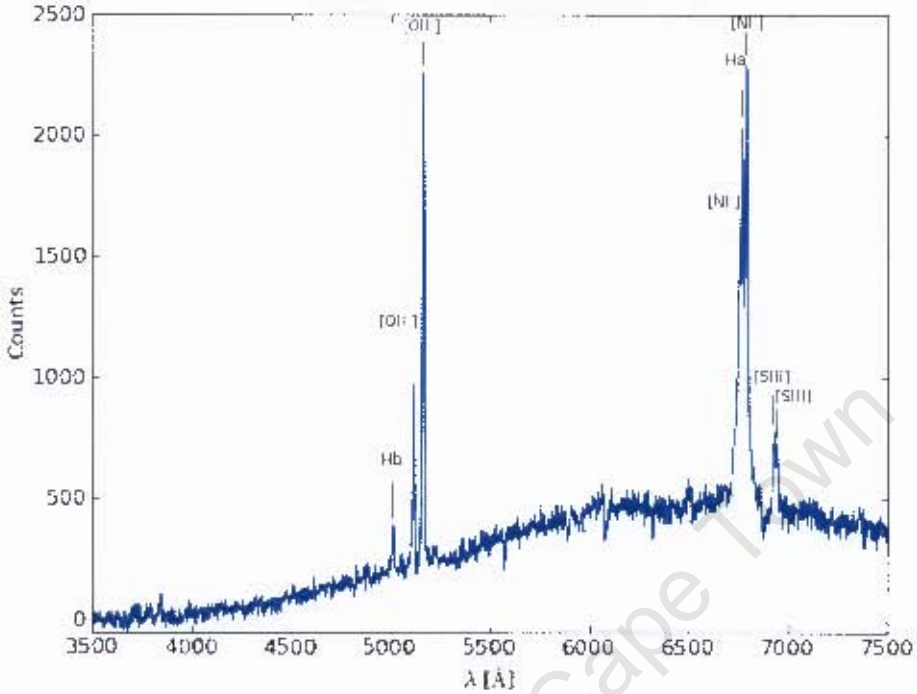

Figure 4.7: Spectrum of a Seyfert galaxy candidate, Vela0173.

4.3.5 Galaxy velocity distribution

Figure 4.8 shows the number density of galaxies per velocity bin. It appears that there is a concentration at $\sim 8\,500\mathrm{km\,s^{-1}}$. Figure 4.9 shows the distribution of the redshifts across the Vela region and clearly indicates the majority of galaxies at $\sim 8\,500\mathrm{km\,s^{-1}}$ lie around $(l, b) \sim (247°, -7°)$. The implications of such a overdensity are discussed in Chapter 5.

4.4 Chapter Conclusion

I observed a sample of galaxies for the pilot redshift survey for the Vela region with the 1.9-m Radcliffe telescope in Sutherland. The raw spectra were reduced using IRAF. Thirty new redshifts were obtained. It was found that this telescope is most sensitive for surveying galaxies with velocities below $10\,000\mathrm{km\,s^{-1}}$. In the next chapter these new redshifts are added to other known redshifts in and surrounding the Vela region to explore the LSS.

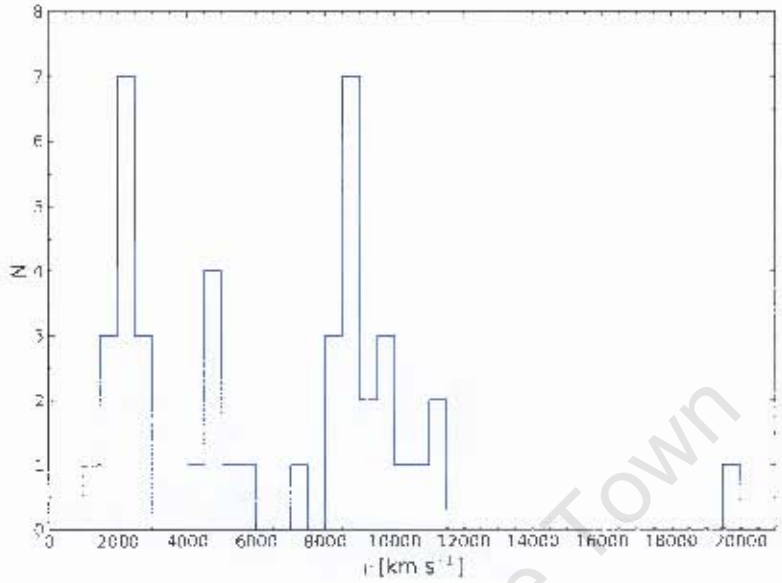

Figure 4.8: Histogram of the velocities obtained at SAAO.

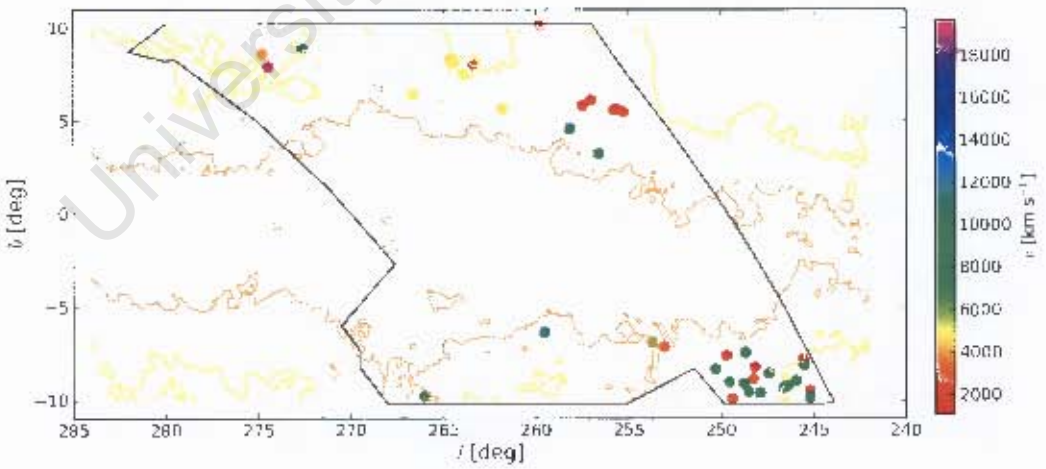

Figure 4.9: Velocity distribution from SAAO observations across the Vela region.

Chapter 5

Large Scale Structure Discussion

In this chapter the newly derived redshift distribution is discussed. The velocities available in the literature from the HYPERLEDA[1] database (Paturel et al. 2003), 6dFGS (Jones et al. 2009) and 2MRS (Macri et al., priv. comm.; Huchra et al. 2011) are combined with the two 6dF fields observed in the Vela region (Kraan-Kortweg, in prep.), unpublished data taken with OPTUPUS in the Hydra-Antlia region (Kraan-Korteweg, priv. comm.) and the new SAAO observations presented in Sec. 4.3.

The redshifts are discussed in connection to structure adjacent to the Milky Way as well as the on-sky 2D distribution of galaxies given in Figs. 3.7 and 3.8. Different figures presenting the 3D distribution in velocity space are shown to highlight the LSS in the region. These include histograms, redshift slices and wedges.

5.1 Histograms

5.1.1 Results from two ZoA 6dF fields

Data was obtained in the Vela region in two six-degree fields with the 6dF instrument mounted on the Anglo Australian Telescope (AAT) [2] during commissioning time (blue circles in Fig. 1.5). The first analysis of the spectra was done by R.C. Kraan-Korteweg and leads to the radial velocity histogram displayed in Fig. 5.1.

Here I compare the resulting velocity histogram with that of the redshift galaxy distribution of the 6dF Galaxy Survey (6dFGS). As part of 6dFGS, Jones et al. (2009) observed 136 304 galaxies in the southern sky ($|b| > 10°$). They derived the galaxy number distribution as a function of redshift for their sample of galaxies complete to $K \leq 12\overset{m}{.}65$. Since the two ZoA fields were observed with the same instrument as that used for the 6dFGS

[1] We acknowledge the usage of the HyperLeda database (http://leda.univ-lyon1.fr)
[2] http://www.aao.gov.au/AAO/ukst/6dF_instrument.html

this relation is a good indicator of the expected distribution for a uniformly filled volume of galaxies. The expected galaxy redshift distribution is therefore over-plotted on the histogram (in red, scaled to the counts in the histogram). Note that the histogram does not conform to the expected galaxy distribution: at $v \sim 18\,000\mathrm{km\,s^{-1}}$ there is an unexpected highly significant peak of ~ 5 times the expected number. This indicates prominent LSS at quite a high redshift (also visible in the bottom right panel of Fig. 5.4).

If one were to ignore the galaxies that so clearly lie above the expected (red) curve, the galaxy number distribution would be substantially ($\sim 30\%$) lower. The resulting expected number of galaxies as a function of redshift (green) is shown in Fig. 5.1 and brings into relief the significance of the overdensity indicated between $3\,500\mathrm{km\,s^{-1}} \lesssim v \lesssim 9\,000\mathrm{km\,s^{-1}}$. This peak corresponds to the peak seen in the SAAO redshifts.

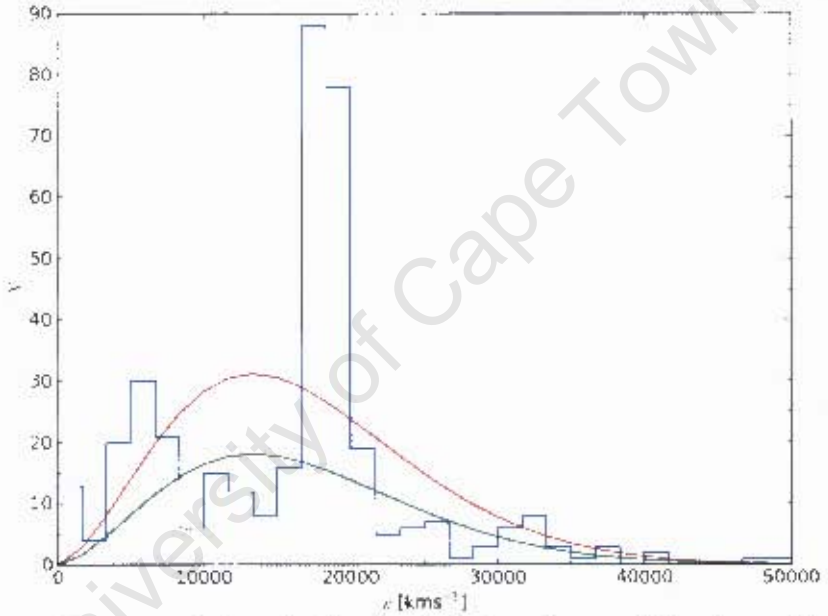

Figure 5.1: Histogram of the velocities obtained from the two fields observed in the Vela region with the 6dF instrument. Over-plotted in red is the redshift galaxy distribution found by Jones et al. (2009) for the 6dFGS normalised for the number of Vela redshifts. This same relation but normalized to the number of Vela redshifts excluding the overdensity is shown in green.

5.1.2 Combining all the redshifts

Figure 5.2 shows the normalised velocity histograms of the Galactic longitudes $260^\circ < l < 300^\circ$ and Galactic latitudes $10^\circ \leq b \leq 30^\circ$ (top panel), $-10^\circ \leq b \leq 10^\circ$ (middle panel), $30^\circ \leq b \leq -10^\circ$ (bottom panel). The top and bottom panels are the redshifts from 6dFGS. These do not cover the ZoA ($|b| < 10^\circ$), therefore I added all available redshifts to the middle panel. The histogram in the middle panel (blue) represents velocities from the

HYPERLEDA database, OPTOPUS data, ZoA 2MRS, the new SAAO redshifts, and two ZoA 6dF fields observed in the Vela region. The contribution of velocities from the two 6dF fields observed in the Vela region are shown in red, whereas the green histogram shows the contribution of velocities from the SAAO observations.

From below the Plane (bottom panel) a peak at $\sim$11 000 km s^{-1} suggests a filament crossing the Plane, where a similar peak, at a slightly lower velocity, $\sim$10 000 km s^{-1} is seen. The SAAO observations are still sensitive for this velocity range (see also Fig. 4.8) though it is at the limit for this spectrograph.

Of note are the peaks at $\sim$18 000 km s^{-1} in both the top and middle panels, as well as a hint of a marginal continuation in the bottom panel, which indicates a structure entering the ZOA from above the Plane. The red histogram in the middle panel illustrates the contribution of the two 6dF fields and the prominent peak at 18 000km s^{-1} in this region. These structures are further explored in Sec. 5.2 and 5.3.

5.2 Velocity grids

Figure 5.3 shows the SAAO observations in an on-sky distribution, colour-coded by velocity. The velocities from the HYPERLEDA database, OPTOPUS, the two 6dF ZoA fields, ZoA 2MRS and 2MRS for the region have been added as smaller points. These galaxies would not have been observed with the SAAO 1.9-m redshift programme since they already have redshifts. This figure highlights how the galaxies in green, i.e. around $v \sim$ 8000km s^{-1}, were sampled in both the SAAO observing run and the two 6dF ZoA fields.

Figure 5.4 then subdivides the distributions of galaxies between $240° < l < 300°$ and $-30° < b < 30°$ in velocity intervals of Δv =3 500km s^{-1} for $v <$ 21 000 km s^{-1} to study the various LSS and their connections with known structures in further detail. The longitudinal range of the panels covers both the Hydra-Antlia and Vela regions (outlined in grey). In the interval 0 km s^{-1} $< v <$ 3 500 km s^{-1} (top left panel) the Hydra and Antlia clusters can be clearly identified at $(l, b) = (269.^{\circ}6, 26.^{\circ}5)$ and $(l, b) = (272.^{\circ}9, 19.^{\circ}2)$. The next velocity interval from 3500 km s^{-1} to 7000 km s^{-1} (top right panel) shows an interesting branching of three structures 'behind' the Antlia cluster into the ZoA, the left structure connecting up with the Vela cluster (Stein 1996). In the velocity interval 7000 km s^{-1} $< v <$ 10 500 km s^{-1} (middle left panel) a distinct filament can be traced into the Vela region at $(l, b) \approx (245°, -10°)$, this feature can clearly be seen in the bottom panel of the histogram presented with Fig. 5.2. At $(l, b) = (248°, -11°)$ there is a known galaxy cluster, CIZA J0717.1-3621, at a redshift of v = 9593 km s^{-1}.

In the velocity interval 10 500 km s^{-1} $< v <$ 14 000 km s^{-1} (middle right panel) a filament appears to disappear into the ZoA at $(l, b) \approx (270°, -10°)$ below the Plane. In the velocity interval 14 000 km s^{-1} $< v <$ 17 500 km s^{-1} (bottom left panel) there appears to be a void between $262° < l < 282°$ above and into the Plane with an increased galaxy population surrounding it. A clear filamentary structure crosses the Hydra-Antlia region at this velocity.

In the next panel (17 500 km s^{-1} $< v <$ 21 000 km s^{-1}: bottom right panel) the overall

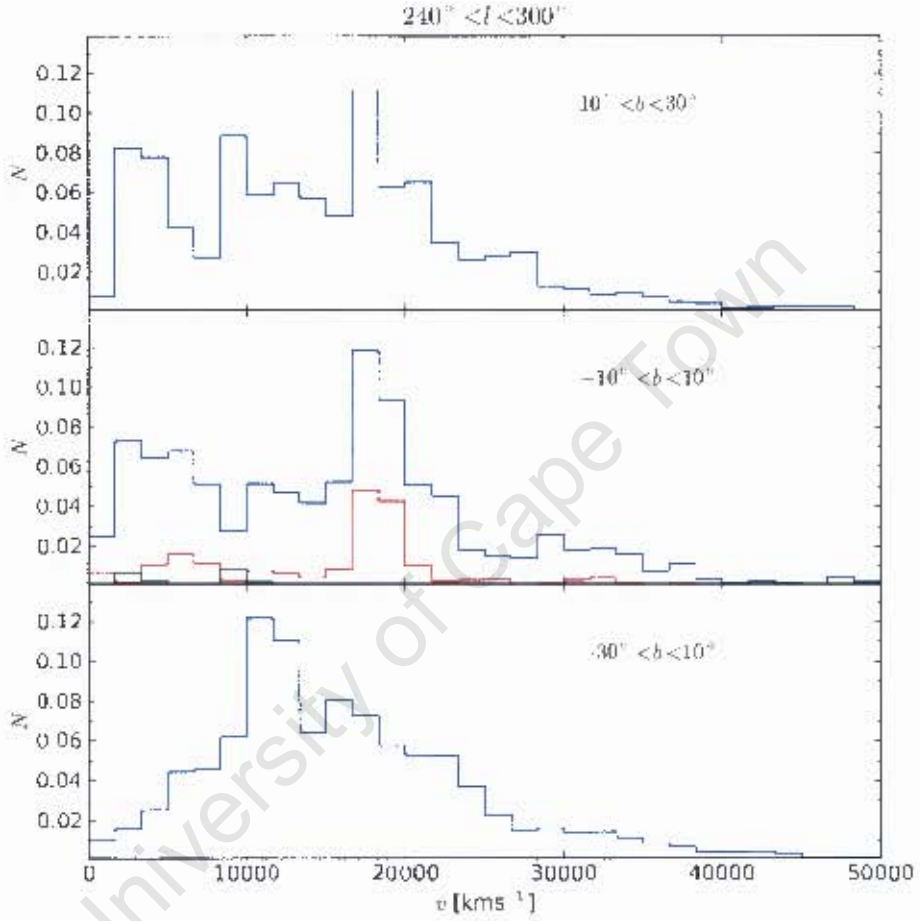

Figure 5.2: Velocity histogram of the Galactic longitudes $260° < l < 300°$ and Galactic latitudes $10° \leq b < 30°$ (top panel), $10° < b < 10°$ (middle panel), $30° < b < 10°$ (bottom panel). The top and bottom panels are the redshifts from 6dFGS. The middle panel blue represents all velocities from the HYPERLEDA database, OPTOPUS data, SAAO redshifts and two 6dF fields observed in the Vela region. The velocities from the two 6dF fields observed in the Vela region are shown in red, whereas the green histogram shows the SAAO redshifts.

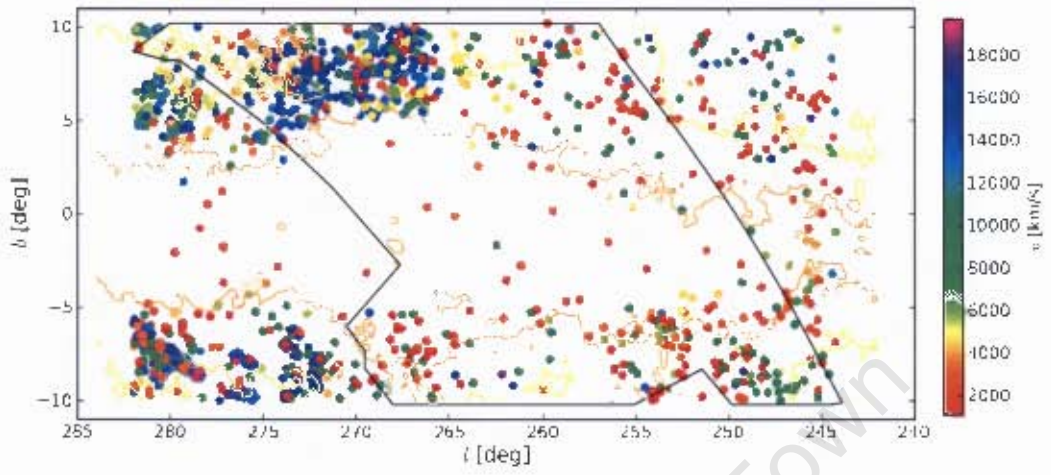

Figure 5.3: Colour coded velocity distribution from SAAO observations, the two ZoA 6dF fields, OPTOPUS data, the ZoA 2MRS and 2MRS, and the HYPERLEDA redshifts across the Vela region.

galaxy count starts to decrease since the 6dFGS peak median velocity ($\sim 14\,000\,\mathrm{km\,s^{-1}}$) has been passed (see Fig. 4.8). Nevertheless some clustering is evident below the Plane, entering the Hydra-Antlia region at $(l, b) \approx (270^\circ, -10^\circ)$. However, above the Plane the two 6dF fields reveal a very extended ($\sim 25^\circ \times 5^\circ$), surprisingly smoothly distributed prominent overdensity of galaxies. Its overall extent is unclear. This coincides with the distribution of elliptical galaxies (Fig. 3.6) and the clustering seen in the on-sky magnitude distribution of galaxies with extinction-corrected magnitudes between 17^m and 18^m(Fig. 3.8).

Moreover, comparison of the overdensity in the $17\,500\,\mathrm{km\,s^{-1}} < v < 21\,000\,\mathrm{km\,s^{-1}}$ panel to the same area in the $10\,500\,\mathrm{km\,s^{-1}} < v < 14\,000\,\mathrm{km\,s^{-1}}$ panel, where 6dF reaches its peak sensitivity, indicates that at lower velocities the area is remarkably sparsely populated. This emphasizes that this overdensity is not just due to the sampling depth of the 6dF instrument.

The overdensity may well extend below the Plane in the Vela region but that area has only been surveyed with the 1.9-m Radcliffe telescope which is not sensitive enough to probe such velocities.

5.3 Velocity wedges

The volume of space probed increases with velocity-distance as radius cubed. To visualise the extent of LSS, redshift wedges for the relevant Galactic longitude and latitude ranges display structures in an opening volume quite well. Figures 5.5a and 5.5b show how the

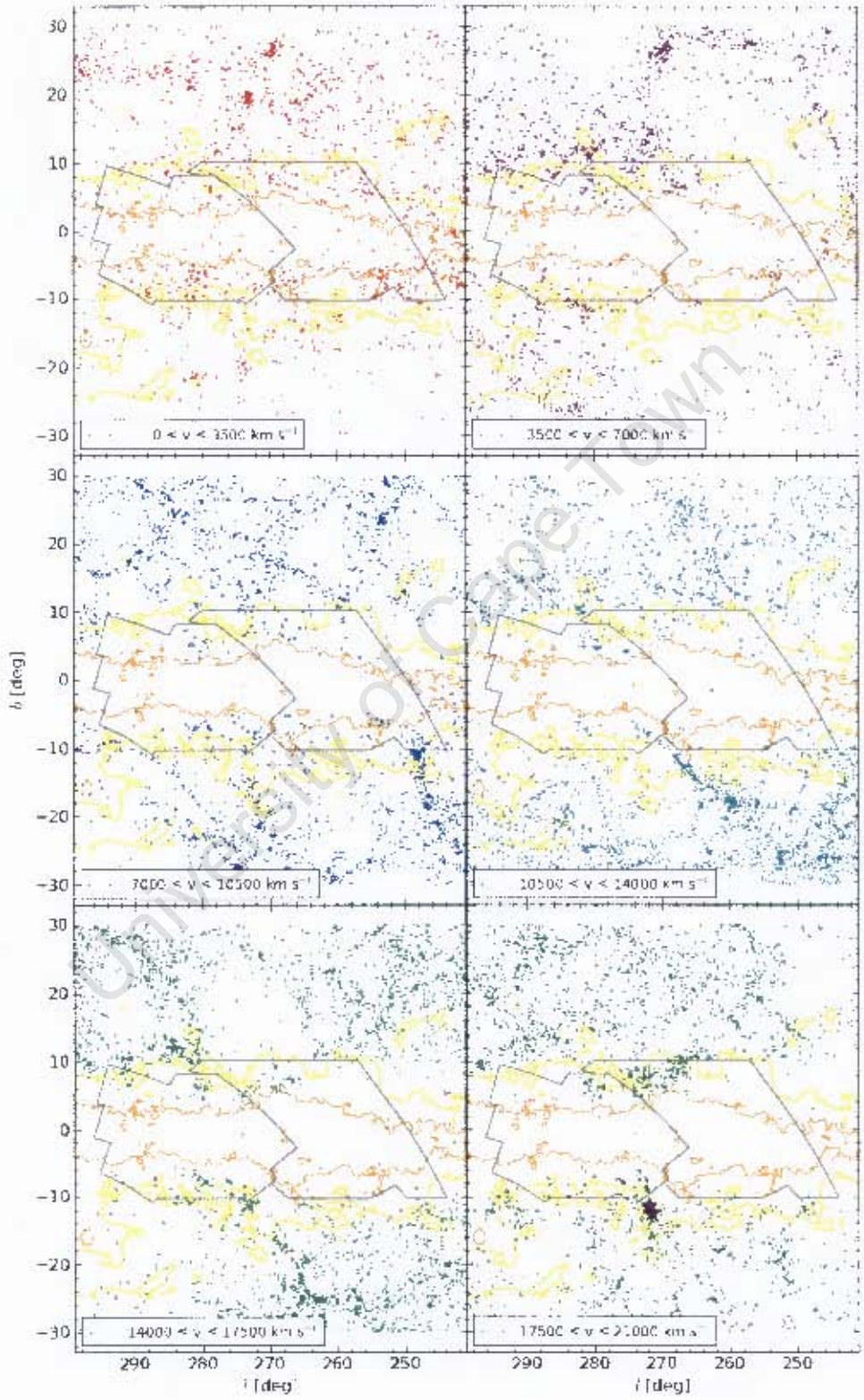

Figure 5.4: Distributions of galaxies between $240^\circ < l < 300^\circ$ and $-30^\circ < b < 30^\circ$ in velocity intervals of Δv 3 500 km s^{-1} from 0 km s^{-1} to 21 000 km s^{-1}. In the bottom right panel (green: $14000 < v < 17500$ km s^{-1}) are the two CIZA (CIZA J0812.5-5714 and CIZA J0820.9-5704, cyan stars) clusters.

area between $240^\circ < l < 300^\circ$ and $-30^\circ < b < 30^\circ$ has been divided to produce the wedges.

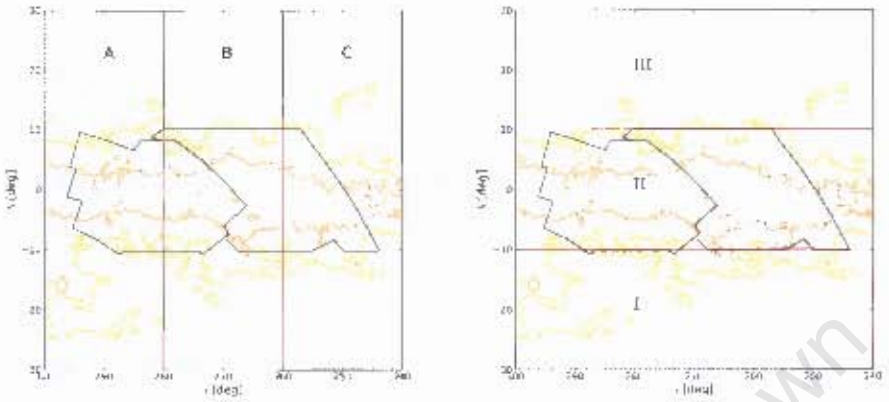

(a) (b)

Figure 5.5: The area $240^\circ < l < 300^\circ$ and $-30^\circ < b < 30^\circ$ divided into (a) three intervals of 20° in Galactic longitude (red lines) which corresponds to the velocity wedges in Fig. 5.6 and (b) into three intervals of 20° in Galactic latitude (red lines) which corresponds to the velocity wedges in Fig. 5.7.

Figure 5.5a corresponds to the wedges in Fig. 5.6 which shows velocity wedges of 20° widths for the Galactic longitude range $240^\circ < l < 300^\circ$. The top row displays the velocity space for $v < 12\,000\,\mathrm{km\,s^{-1}}$ (a-c) and the bottom row $v < 25\,000\,\mathrm{km\,s^{-1}}$ (A-B). In this way the top row highlights the nearby structures whereas the bottom row highlights more distant structures.

I first examine evidence of nearby structure. The velocity wedge from $260^\circ < l < 280^\circ$, labelled (b), shows evidence of a filament crossing the ZoA at very small velocities ($\sim$2 500 km s^{-1}). In the velocity wedge from $240^\circ < l < 260^\circ$, labelled (c), there appears to be some structure bridging the ZoA at $\sim$7 200 km s^{-1}.

In the $280^\circ < l < 300^\circ$ interval, labelled (A), at high velocities ($16\,000\,\mathrm{km\,s^{-1}} < v < 23\,000\,\mathrm{km\,s^{-1}}$) there is a hint of a structure coming into the ZoA ($b \sim -10^\circ$) from below the Plane at $\sim$18 000 km s^{-1}. There is a possibility that this structure could be crossing the Plane since there is evidence of more clustering above the Plane ($b > 10^\circ$) at $\sim$18 000 km s^{-1}. Looking at high velocities at the Galactic longitude interval of $260^\circ < l < 280^\circ$, labelled (B), there appears more of the structure seen in the wedge labelled (A), perhaps crossing the Plane at $\sim$18 000 km s^{-1}. Above the Plane this overdensity is particularly evident, and as described in Fig. 5.4 in the previous section. The velocity interval in front of the overdensity ($10\,500\,\mathrm{km\,s^{-1}} < v < 16\,000\,\mathrm{km\,s^{-1}}$) is sparsely populated indicating that the overdensity is not due to the deep sampling in the 6dF fields.

The ZoA slice ($|b| < 10^\circ$) in the wedge labelled (C) at high velocities $v > 12\,000\,\mathrm{km\,s^{-1}}$ the Galactic longitude interval $240^\circ < l < 260^\circ$ has very few redshifts since very few galaxies

have been observed in this area. The available redshifts are from the 1.9-m Radcliffe telescope at Sutherland which becomes increasingly poor at detecting galaxies beyond 11 000 km s^{-1}. It is however interesting to note that above the Plane there is a structure disappearing into the ZoA at $v \sim$16 500 km s^{-1}. And at $v \sim$ 10 000 km s^{-1} there is evidence of filaments leading into the ZoA from above and below the Galactic plane.

The wedges in Fig. 5.7 correspond to the subdivision in Galactic longitude and latitude as depicted in Fig. 5.5b. Figure 5.7 shows velocity slices in 20° intervals of Galactic latitude between $-30° < b < 30°$. The rows of wedges again show in the top row the velocity space for $v < 12\,000$ km s^{-1} in the wedges labelled (i-iii) and in the bottom row for $v <$ 25 000 km s^{-1} in the wedges labelled (I-III).

The velocity wedge for the Galactic latitude interval of $-30° < b < -10°$, labelled (I), shows the same structure seen in the wedge labelled (A) at 10 000 km s^{-1} $< v <$ 12 000 km s^{-1}. Above the Galactic Plane, $10° < b < 30°$ labelled (III), the structure seen disappearing into the ZoA at $v \sim$16 500 km s^{-1} in the wedge labelled (C) is evident in the clustering in (III).

In the ZoA ($-10° < b < 10°$) in the wedge labelled (II), the overdensity at $v \sim$18 000 km s^{-1} is very prominent between $270° < l < 280°$. The extent and prominence of the overdensity in Galactic longitude (crossing both the Vela and Hydra-Antlia regions) is highlighted in this panel.

5.4 Implications

The most prominent structures in the Vela region are (a) those leading into the ZoA at 9 000 km s^{-1} $< v <$ 11 000 km s^{-1}, especially between $240° < l < 260°$, and (b) the overdensity at $v \sim$ 18 000 km s^{-1} which appears to extend over a very wide region. The extent of this overdensity is not clear and may well be much larger than what could be mapped here. As yet no fingers of god have been found. On the contrary, the distribution is surprisingly smooth. It is striking that this overdensity extends *at least* 25 degrees in Galactic longitude and five degrees in Galactic latitude, which translates, at a distance of $\sim$ 200 Mpc, to a massive conglomeration of galaxies over an area of minimally $\sim$ 1500 Mpc^2. The extinction-corrected magnitude slices (Figs. 3.7 and 3.8 in Sec. 3.2.3) and surrounding LSS suggests that this overdensity may well extend to the other side of the Galactic Plane. Additional redshift observations are needed to map the true extent of this overdensity.

Of interest is the overdensity at $v \sim$ 18 000 km s^{-1}. It is located where recent bulk flow studies consistently claim that attractor(s) are needed to explain flow fields that seem to significantly contribute to the peculiar velocity of the LG from beyond 100 Mpc (Hudson et al. 2004, Feldman et al. 2010, Macaulay et al. 2011). This overdensity at $\sim$ 200 Mpc is also unexpected in terms of the expected homogeneity of the Universe on scales of 100 Mpc, required by the current cosmological model (Joyce et al. 2005, Hogg et al. 2005).

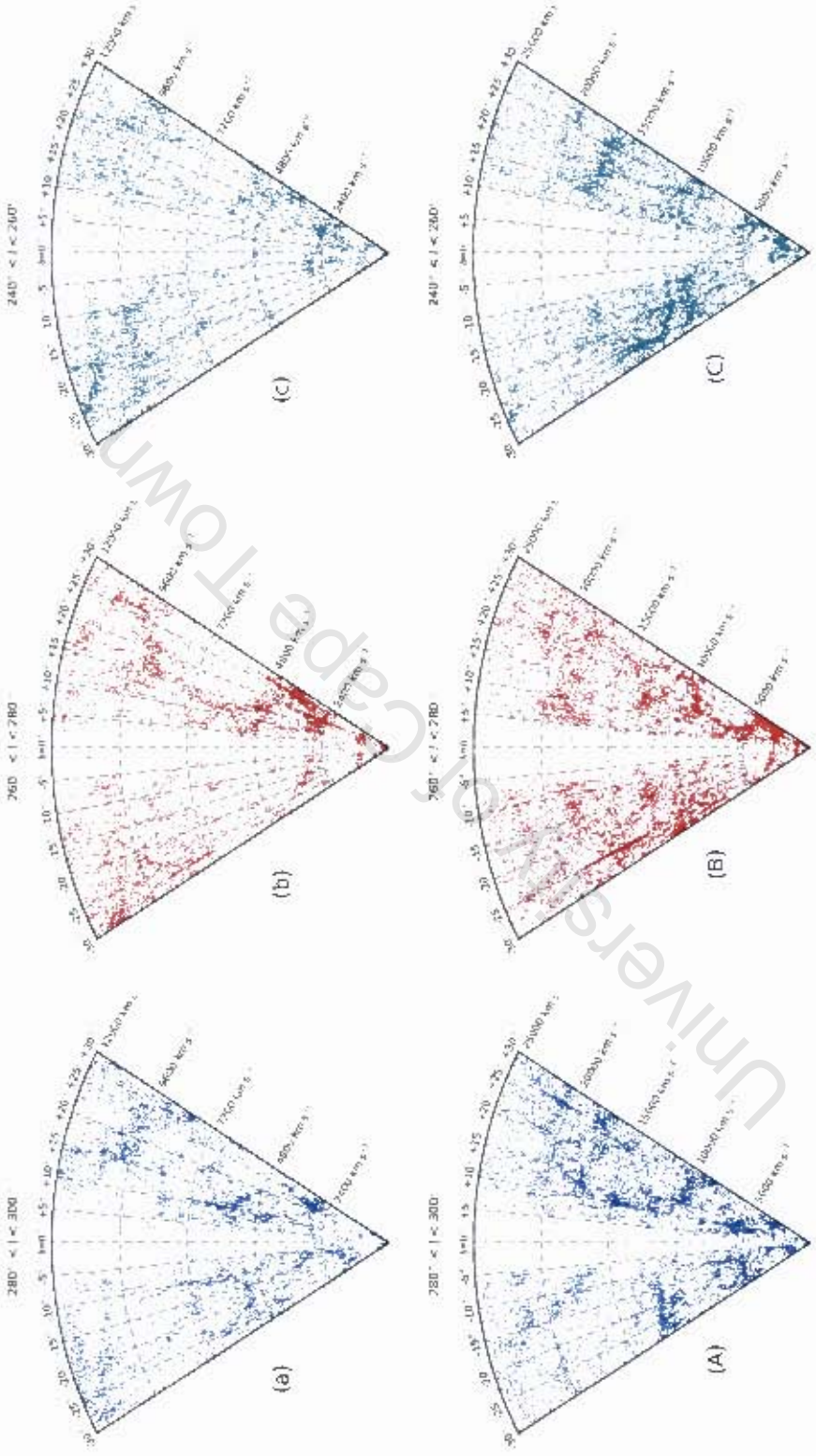

Figure 5.6: Redshift wedges in 20° intervals of Galactic longitude for the Galactic latitude range $-30° < b < 30°$, with v <12 000 km s^{-1} (top panel) and v <25 000 km s^{-1} (bottom panel).

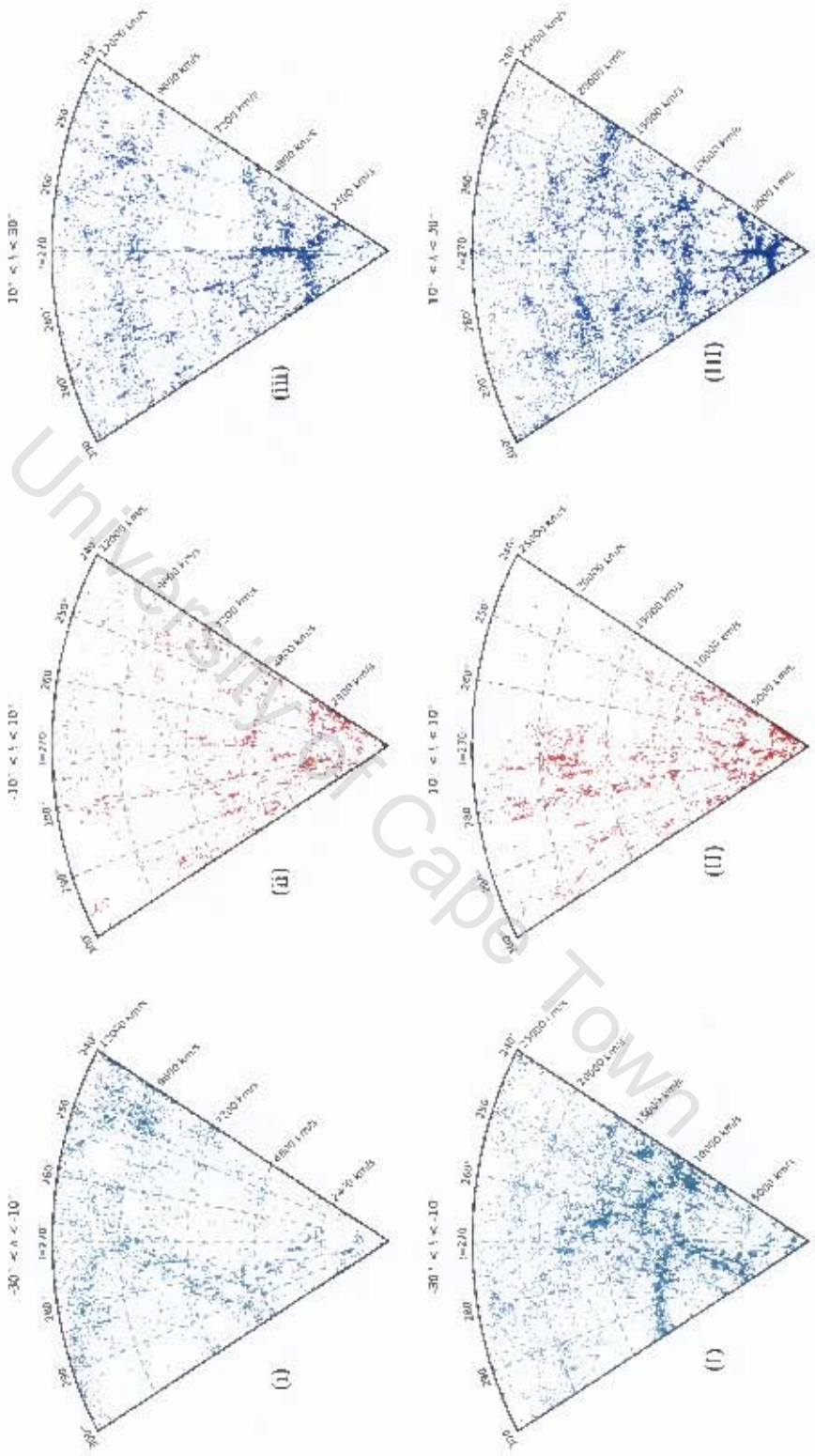

Figure 5.7: Redshift wedges in 20° intervals of Galactic latitude for the Galactic longitude range $300° > l > 240°$, with $v < 12000\,\mathrm{km\,s^{-1}}$ (top panel) and $v < 25000\,\mathrm{km\,s^{-1}}$ (bottom panel).

Chapter 6

Conclusions

The deep optical Vela galaxy catalogue was presented in this thesis. The Vela catalogue lists 3922 galaxy candidates to the apparent diameter completeness limit of 12″. An additional 388 smaller galaxies are listed with diameters below the 12″ limit.

Of the galaxies in the Vela catalogue, $\sim$ 50% (2106) have counterparts in 2MASX. This high fraction of counterparts is the result of the lower star density in the Vela region compared to regions closer to the Galactic bulge. A comparison of the positions determined from DSS to the positions of their 2MASX counterparts finds the positional accuracy of 1.″3 for the Vela catalogue.

The calibration of the Vela magnitudes and the subsequent comparison to the ESO-LV, Hydra-Antlia and internal magnitudes shows linearity over the whole magnitude range ($13^{\rm m} - 19^{\rm m}$). The average scatter of the magnitude estimates is $\sigma \sim 0\overset{\rm m}{.}75$ when compared to other catalogues, although internally the scatter is only $\sigma \sim 0\overset{\rm m}{.}57$.

The average observed diameter is $< D >= 20''$, which is smaller than the average diameters in the Hydra-Antlia, Crux and GA regions. This is due to the Vela region's 'transparency' since it is not as star-crowded, which allows the identification of fainter and smaller galaxies. The average extinction-corrected diameter is $< D^0 >= 53''$. The average observed magnitude is $< B_J >= 18\overset{\rm m}{.}4$ and the average extinction-corrected magnitude is $< B_J^0 >= 16\overset{\rm m}{.}7$.

The Vela catalogue has 56 galaxy counterparts in the ESO-LV catalogue, which is complete to $D^0 = 1.'3$ away from the Galactic plane. The Vela catalogue shows 311 galaxies with extinction-corrected diameters greater than $D^0 > 1.'3$. Had the Milky Way not obscured the extragalactic sky, Lauberts would have recorded another 255 galaxies within the ESO-LV completeness diameter limit.

Extinction-corrected diameters and magnitudes were analysed for completeness. The cumulative histograms (Fig. 3.4) show that the catalogue is complete to $B \sim 18\overset{\rm m}{.}5$ and $D \sim 12.''6$ for extinction levels $A_B \leq 3^{\rm m}$. Up to extinction levels of $A_B \leq 3^{\rm m}$, the extinction-corrected parameters in the Vela catalogue are complete to $B^0 \approx 15\overset{\rm m}{.}5$ and $D^0 \approx 40''$.

The elliptical galaxies appear strongly clustered in several areas (Fig. 3.6) and well

aligned with nearby and distant structures seen in the extinction-corrected magnitude slices (Figs. 3.7 and 3.8) and the velocity slices (Fig. 5.4) and wedges (Figs. 5.6 and 5.7). A prominent filament can be traced into the ZoA at $10\,000\,\mathrm{km\,s^{-1}}$ at $(l, b) \approx (247°, 10°)$, adjacent to a CIZA galaxy cluster. A very large and extended overdensity at $18\,000 - 20\,000\,\mathrm{km\,s^{-1}}$ is present in all the visualisations of the 3D distribution (where data is available). The whole extent of this overdensity is as yet unknown, but it is located at the distance and coordinates where recent bulk flow studies consistently claim that attractor(s) are needed to explain the peculiar velocity of the LG from beyond 100 Mpc (Hudson et al. 2004, Feldman et al. 2010, Macaulay et al. 2011) and even 300 Mpc (Kashlinsky et al. 2008; 2010; 2011, Abate & Feldman 2012). This overdensity at ~ 200 Mpc is also unexpected in terms of the expected homogeneity of the Universe on scales of 100 Mpc, for the current cosmological model (Joyce et al. 2005, Hogg et al. 2005).

6.1 Looking towards the Future

The Vela catalogue provides the basis for doing an extensive redshift survey across the whole region. In combination with the adjacent Hydra-Antlia region the targets are available to map the extent and richness of the overdensity at $18\,000 - 20\,000$ km s^{-1} so evident in the ZoA 6dF data. Several instruments can be used. The optimal instrument would be the AAOmega multifibre spectrograph at the Anglo Australian Telescope (AAT) that can capture up to 392 spectra in one exposure. Figure 6.1 shows the number density of galaxies in one degree radius circles, the aperture of AAOmega.

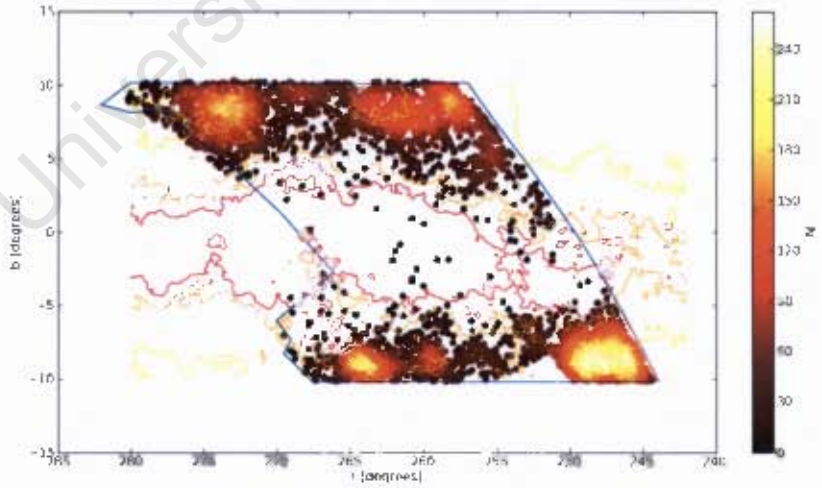

Figure 6.1: Number density of Vela catalogue galaxies within a radius of one degree. The dust extinction contours are shown in red ($A_B = 5^m$), orange ($A_B = 3^m$) and yellow ($A_B = 1^m$).

Alternatively the Southern African Large Telescope has Multi-Object Spectroscopy (MOS) capability, although it has a small field of view (8′). The radio regime, through the 21-cm line emission of the HI gas in galaxies, can probe the most obscured regions where the distant overdensity may well be crossing, and with the SKA Pathfinders - MeerKAT and ASKAP, there will be instruments with enough sensitivity and bandwidth to detect HI emission in gas rich galaxies to large distances. In particular The WALLABY project (Koribalski & López-Sánchez 2009) with ASKAP, a proposed deep HI all-sky survey, with it's large field of view will be optimally suited to probe the overdensity.

The deep optical Vela galaxy catalogue shows that, despite the problems in mapping LSS in the ZoA, a wealth of information is available. With the new data new insights can be achieved about the dynamics in the Local Universe.

Appendix A

Catalogue

In this appendix:

A.1 First page of the Vela Catalogue $D \geq 12''$.

A.2 First page of the Vela Catalogue $D < 12''$.

A.3 First page of the counterparts in 2MASX and ESO-LV.

The full tables can be found at:

```
http://www.ast.uct.ac.za/~kosma/
    user: guest
password: guest2readthesis
```

Table A.1: The Vela Catalogue $D \geq 12''$.

Ident	α [h :m :s]	δ [° :′ :″]	l °	b °	RCS	X	Y	Flag	D [″]	d [″]	A_B [mag]	D^0 [″]	B [mag]	B^0 [mag]		Type Class.		Sup. Stars	Remarks
(1)	(2)	(3)	(4)	(5)	(6)	(7)	(8)	(9)	(10)	(11)	(12)	(13)	(14)	(15)	(16)	(17,18,19)		(20)	(21)
1	07 12 38.9	-32 31 28	244.4102	−10.1261	367	−20.3	137.4		35	30	0.6	39	16.4	15.7		S	V		ring ? LSB disk
2	07 12 41.2	-32 29 17	244.3805	−10.103	367	−20.2	139.3		27	8	0.7	30	17.9	17.2		S			p.cov.by *
3	07 12 54.1	-32 35 41	244.4981	−10.1086	367	−11.2	133.7		34	11	0.6	37	17.0	16.4		I			
4	07 13 05.7	-32 44 12	244.6459	−10.1339	367	−10.6	125.9		16	4	0.6	17	19.5	18.9		S	E		LSB
5	07 13 11.9	-32 25 55	244.377	−9.9814	367	−10.4	142.4		24	7	0.7	27	17.8	17.1		S E			
6	07 13 13.4	-32 53 06	244.7934	−10.1742	367	−10.2	118.1		20	17	0.6	23	16.9	16.3		E			HSB
7	07 13 43.7	-33 01 38	244.9704	−10.1409	367	−8.7	110.5		27	5	0.6	30	18.7	18.1		S	E		vLSB disk
8	07 13 44.1	-32 28 26	244.4656	−9.8979	367	−8.8	140.3		22	5	0.7	25	18.9	18.2		S	N		p.cov.by * ; vLSB disk
9	07 14 11.0	-32 58 20	244.9624	−10.0311	367	0.9	113.5		13	5	0.6	15	18.8	18.2		F			HSB
10	07 14 26.1	-32 47 45	244.8249	−9.9063	367	1.7	122.9		16	3	0.6	17	19.7	19.1		S	E		
11	07 14 27.8	-33 17 55	245.2866	−10.121	367	1.8	95.9		16	4	0.6	18	19.2	18.5		S	E		p.cov.by *
12	07 14 27.9	-33 20 01	245.3188	−10.136	367	1.8	94.0		13	5	0.6	14	19.7	19.1		S			vLSB
13	07 14 41.5	-32 26 58	244.5331	−9.7058	367	2.4	141.6		13	4	0.7	15	19.6	18.9		S			LSB
14	07 14 42.7	-32 59 54	245.0355	−9.9429	367	2.5	112.2		16	13	0.6	18	17.8	17.1		S			
15	07 14 47.5	-32 59 58	245.044	−9.9283	367	2.7	112.1		22	3	0.6	24	19.5	18.8		S	E		LSB
16	07 14 49.8	-33 09 25	245.1913	−9.9901	367	2.9	103.7		17	8	0.6	19	18.2	17.6		S			
17	07 14 52.2	-32 32 15	244.6301	−9.7107	367	3.0	137.0		13	5	0.6	14	19.5	18.9		S			vLSB disk
18	07 15 00.8	-33 07 00	245.1716	−9.9379	367	11.7	105.8		20	11	0.6	22	18.4	17.8	?	S			vvLSB ; p.cov.by *
19	07 15 04.6	-33 14 24	245.2901	−9.9801	367	11.8	99.2		15	5	0.6	17	19.2	18.6		S			LSB disk
20	07 15 17.8	-33 05 57	245.1821	−9.8769	367	12.5	106.8		19	5	0.6	21	18.8	18.1		S	N		br.blg.
21	07 15 24.1	-33 37 00	245.6641	−10.0841	367	12.8	78.9		19	7	0.6	21	18.3	17.7		S			
22	07 15 25.4	-33 27 50	245.5266	−10.0131	367	12.8	87.1		27	16	0.6	30	16.9	16.2		S			
23	07 15 27.7	-33 01 01	245.1225	−9.8097	367	13.0	111.1		13:	5	0.6	14	19.4	18.8					LSB
24	07 15 31.5	-33 03 47	245.1705	−9.8181	367	13.2	108.7		30	16	0.6	35	16.5	15.9		E			HSB
25	07 15 32.3	-33 12 57	245.311	−9.8827	367	13.2	100.4		30	7	0.6	33	17.7	17.0		S			
26	07 15 34.4	-32 49 54	244.9642	−9.7072	367	13.3	121.1		16	5	0.6	18	18.7	18.1		S			
27	07 15 35.3	-33 01 05	245.1354	−9.7864	367	13.4	111.2		20	15	0.6	22	17.4	16.8		S			br.blg. ; LSB disk
28	07 15 39.4	-33 18 39	245.4087	−9.9022	367	13.5	95.3		22	16	0.7	25	17.8	17.1		S			vvLSB ; cl.to a br.* ; int.to observe in HI
29	07 15 41.1	-32 37 36	244.788	−9.5958	367	13.7	132.1		30:	16	0.5	33	17.2	16.7		S		S	br.blg. or * ; vvLSB disk
30	07 15 42.1	-33 27 11	245.5426	−9.9562	367	13.7	87.6		15	5	0.6	17	18.7	18.0		S			
31	07 15 46.6	-33 38 35	245.7229	−10.0255	367	13.9	77.5		16	11	0.6	18	18.0	17.4	?	S			br.blg.and vLSB disk or *
32	07 15 48.8	-32 55 16	245.0681	−9.7013	367	14.0	116.3		19	5	0.6	21	18.4	17.8		S M			
33	07 15 53.7	-33 32 08	245.6358	−9.9562	367	22.4	83.2		20	12	0.6	22	18.1	17.5		S			vLSB disk ; neighb.of 351
34	07 15 56.2	-33 19 14	245.4436	−9.8539	367	22.6	94.8		32	16	0.7	36	16.8	16.1		S M			p.cov.by * ; vLSB disk ; br.blg.
35	07 16 02.3	-33 57 03	246.0281	−10.1116	367	22.8	61.1		17	11	0.7	19	18.2	17.5		S			
36	07 16 03.2	-33 31 22	245.6389	−9.9209	367	22.9	84.0		40	4	0.6	44	18.1	17.5		S	E		neighb.of 352
37	07 16 05.4	-34 02 07	246.11	−10.139	367	22.9	56.5		16	5	0.7	18	18.6	17.8		S			

Table A.2: The Vela Catalogue $D < 12''$.

Ident	α [h :m.s]	δ [° :′:″]	l °	b °	RCS	X	Y	Flag	D [″]	d [″]	A_B [mag]	D^0 [″]	B [mag]	B^0 [mag]		Type Class.	Sup. Stars	Remarks
(1)	(2)	(3)	(4)	(5)	(6)	(7)	(8)	(9)	(10)	(11)	(12)	(13)	(14)	(15)	(16)	(17,18,19)	(20)	(21)
3923	07 18 02.7	-33 45 23	246.0372	−9.6519	367	45.2	71.5		11	5	0.8	13	19.1	18.3				group of 309, 310, 311, 313
3924	07 18 24.7	-33 20 09	245.6893	−9.3969	367	46.5	94.0		11	11	0.7	13	18.3	17.5		E		group of 294, 295, 296, 297, 298, 299
3925	07 18 29.9	-33 21 51	245.7232	−9.3933	367	46.7	92.4		9	4	0.8	10	19.5	18.7	?			neighb.of 292
3926	07 18 31.2	-33 31 31	245.8716	−9.4608	367	46.7	83.7		11	11	0.7	13	18.5	17.7		S		vLSB disk ; neighb.of 287, 288, 290
3927	07 18 32.2	-33 20 21	245.7041	−9.375	367	46.8	93.8		8	5	0.8	9	19.4	18.6	?			or * ; group of 293, 295, 296, 297, 298, 299
3928	07 18 32.9	-33 21 49	245.7274	−9.3837	367	46.9	92.5		11	5	0.8	13	19.0	18.2	?	S	E	neighb.of 291
3929	07 18 36.1	-33 31 51	245.8843	−9.4481	367	46.9	83.4		9	5	0.8	10	19.6	18.8				neighb.of 287, 288, 289
3930	07 19 11.7	-34 11 44	246.5437	−9.6329	367	56.5	47.7		11	5	0.9	13	19.0	18.1	?	S		or ** ; neighb.of 274
3931	07 19 33.9	-35 26 40	247.7145	−10.1177	367	56.8	−19.3		9	9	1.1	12	18.9	17.7		S		
3932	07 19 34.3	-34 00 51	246.414	−9.4824	367	57.7	57.5		9	7	0.8	11	19.0	18.1				group of 242, 243, 245
3933	07 19 35.0	-35 10 10	247.4656	−9.9928	367	57.0	−4.5		11	8	1.2	15	18.8	17.5		S		group of 249, 250, 251
3934	07 19 56.6	-34 08 15	246.5607	−9.4684	367	66.9	50.7		11	7	0.8	13	18.9	18.0		S		neighb.of 232
3935	07 20 33.0	-33 14 18	245.8031	−8.9535	367	69.4	99.0		11	7	0.7	13	19.0	18.2	?	S		
3936	07 21 23.7	-33 29 08	246.1069	−8.907	367	79.9	85.5		11	3	0.9	13	19.9	19.0		S		neighb.of 162, 164
3937	07 21 23.8	-33 28 42	246.1005	−8.9034	367	79.9	85.9		9	9	0.8	11	18.9	18.0		S		neighb.of 162, 163
3938	07 21 57.5	-33 50 50	246.4872	−8.965	367	89.4	66.1		11	8	1.0	14	18.8	17.8				
3939	07 22 15.6	-34 33 11	247.1542	−9.2266	367	89.6	28.2		11	11	1.3	16	18.7	17.3		S		neighb.of 133
3940	07 23 14.4	-32 27 03	245.351	−8.0936	367	103.0	140.9		11	4	0.8	13	19.8	19.0		S		
3941	07 23 19.0	-34 11 32	246.9274	−8.8693	367	101.2	47.3		9	9	1.1	12	19.0	17.8		S		neighb.of 109
3942	07 23 28.0	-33 51 40	246.6428	−8.6918	367	102.1	65.2		9	8	1.0	11	19.1	18.0		S		or * ; neighb.of 112, 113
3943	07 23 51.3	-35 49 05	248.448	−9.5036	367	108.9	−40.0		11	11	1.2	15	18.6	17.3		S		obscured by *
3944	07 24 15.8	-33 04 28	246.0108	−8.1863	367	114.1	107.1		9	5	0.8	11	19.6	18.7				
3945	07 24 26.2	-36 59 06	249.5594	−9.9225	367	109.2	−102.4		11	5	1.5	18	19.5	17.7		S		neighb.of 392, 393
3946	07 25 06.4	-35 49 40	248.5727	−9.2815	367	120.5	−40.7		9	9	1.4	14	19.1	17.5		S		
3947	07 25 07.2	-35 30 15	248.2815	−9.1327	367	121.0	−23.5		11	11	1.6	18	18.3	16.5		K		HSB
3948	07 25 14.3	-33 35 01	246.5624	−8.2375	367	124.1	79.6		11	8	1.1	14	18.9	17.8		S		
3949	07 25 27.1	-35 30 05	248.31	−9.0713	367	122.0	−23.4		11	7	1.7	19	19.0	17.1				w.comp.
3950	07 25 28.7	-33 48 39	246.7897	−8.2969	367	124.5	67.4		9	9	1.1	12	18.8	17.6				HSB
3951	07 25 30.7	-32 54 02	245.9756	−7.874	368	−144.7	115.8		9	9	1.1	12	19.5	18.2				LSB
3952	07 25 51.8	-34 42 05	247.6276	−8.6326	367	132.4	19.3		11:	4	1.4	16	19.6	18.1	?	S		p.cov.by * ; neighb.of 36
3953	07 25 52.6	-34 44 17	247.6618	−8.6469	367	132.4	17.4		9	9	1.4	13	18.9	17.4				group of 38, 40
3954	07 25 58.2	-36 14 26	249.0257	−9.3125	368	−129.4	−63.3		11	3	1.6	19	19.9	18.0		S		
3955	07 26 01.6	-32 56 18	246.0595	−7.7953	368	−134.8	114.2		9	5	1.2	13	20.0	18.6				LSB ; poss.larger
3956	07 26 02.7	-34 16 15	247.2575	−8.4028	367	133.6	42.4		9	9	1.0	12	18.8	17.8	?	E		or *
3957	07 26 06.2	-32 53 33	246.0259	−7.7599	367	135.9	116.5		11	7	1.3	16	19.1	17.7				
3958	07 26 13.5	-35 54 10	248.7444	−9.1135	368	−129.2	−45.0		11	4	1.7	19	19.8	17.9				neighb.of 377

Table A.3: Galaxy Counterparts

Vela	2MASX	ESO-LV
1	08165172-4750417	
2	07124122-3229181	
4	08173064-4831283	
5	07131338-3253061	
9	08170610-4924329	
11	08162622-4847170	
13	08164820-5036409	
14	07144274-3259548	
17	08154944-5035581	
19	08152717-5037111	
23	07153155-3303471	
25	08131876-4759185	
26	07153537-3301042	
28	08131024-4918105	
29	07154111-3237362	
33	08125719-5012328	
34	07155628-3319133	
37	07161630-3324374	
40	08120552-4910178	
41	08115962-4914508	
42	07163514-3235312	
43	08121993-4923398	
44	08120767-4939278	
45	07160535-3402074	
46	07165665-3228242	
47	08114036-5038078	
48	08113691-5005087	
49	07171390-3436347	
52	08112988-4904309	
54	07172515-3323267	
56	08110730-4718344	
57	07173022-3304007	
59	07173643-3345146	
60	07170426-3401392	
61	08111136-4915200	
62	08105767-4915219	
63	07174603-3411486	
64	07175143-3314486	
65	07175311-3332026	
66	08110109-4931289	
68	07175724-3313346	
69	08112431-5022189	
71	07170726-3254197	
72	07170971-3338507	
74	08104263-4923538	
75	08103853-4924268	
76	07181204-3429100	
78	08102175-4916248	
79	07182542-3336161	
81	08103051-5038089	
82	07182951-3436051	
83	07182966-3332311	
84	08094933-4921041	
87	08093370-5100490	
88	08093012-5041010	
89	07183357-3319051	
90	08084979-4835316	
91	07183644-3317591	
95	07184755-3509396	
96	07184823-3454106	2090170
97	08083602-5001060	
98	08085855-5037146	
99	07185147-3503016	
100	07185312-3246487	
102	07185557-3328536	
103	07180790-3306076	

Appendix B

Figures

Figures in this appendix:

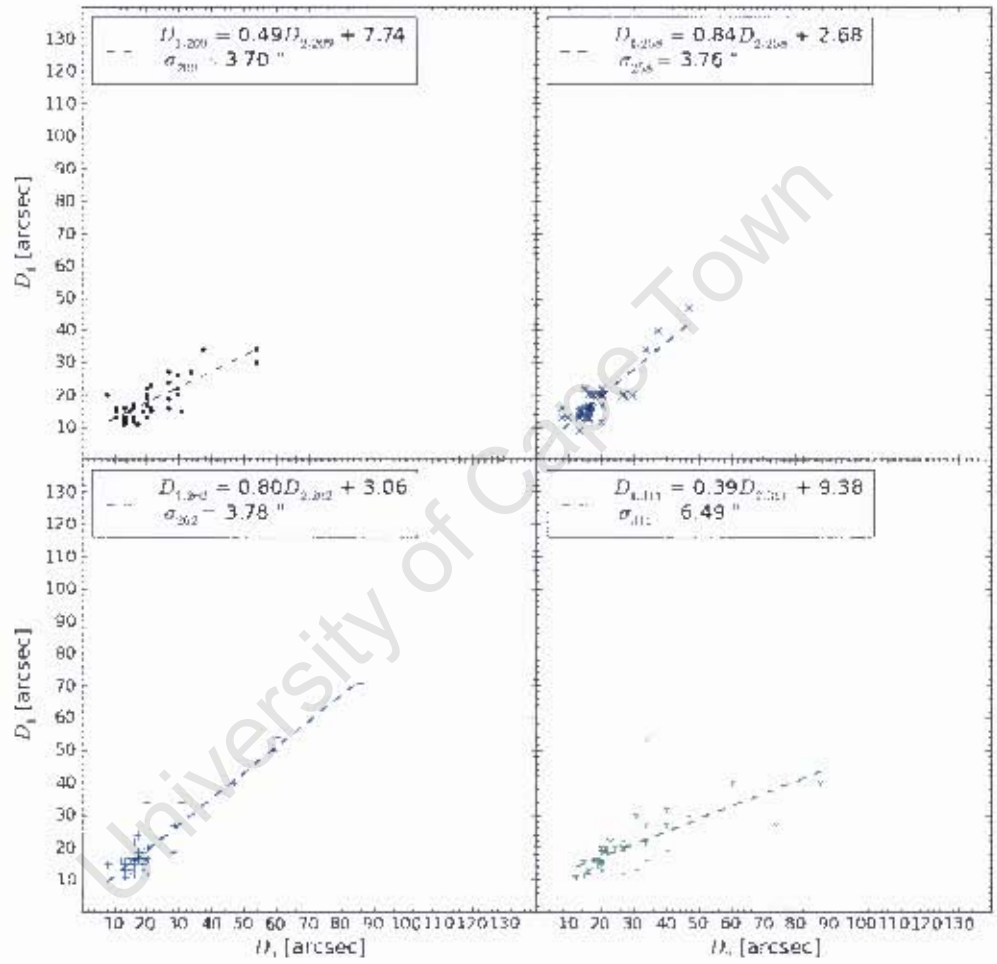

Figure B.1: Diameter difference and least square fit to Plate 209, 258, 262 and 311.

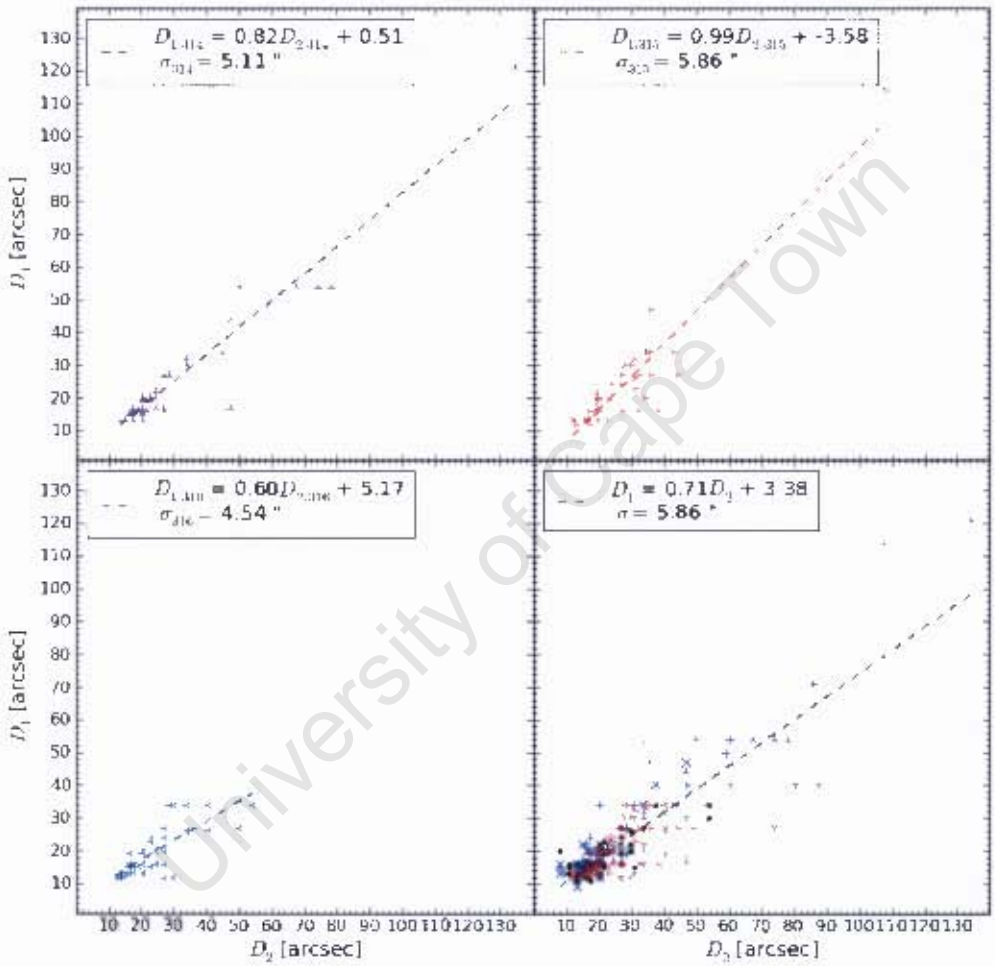

Figure B.2: Diameter difference and least square fit to Plate 314, 315, 316 and all plates.

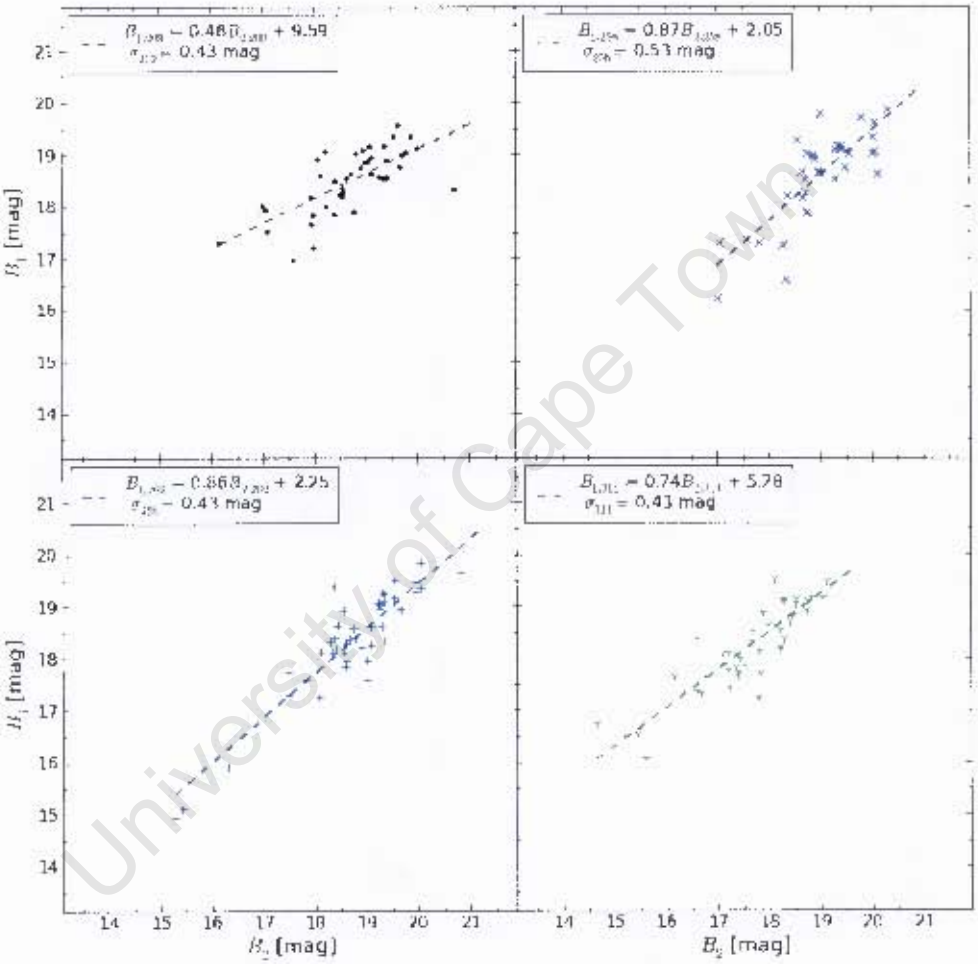

Figure B.3: Magnitude difference and least square fit to Plate 209, 258, 262 and 311.

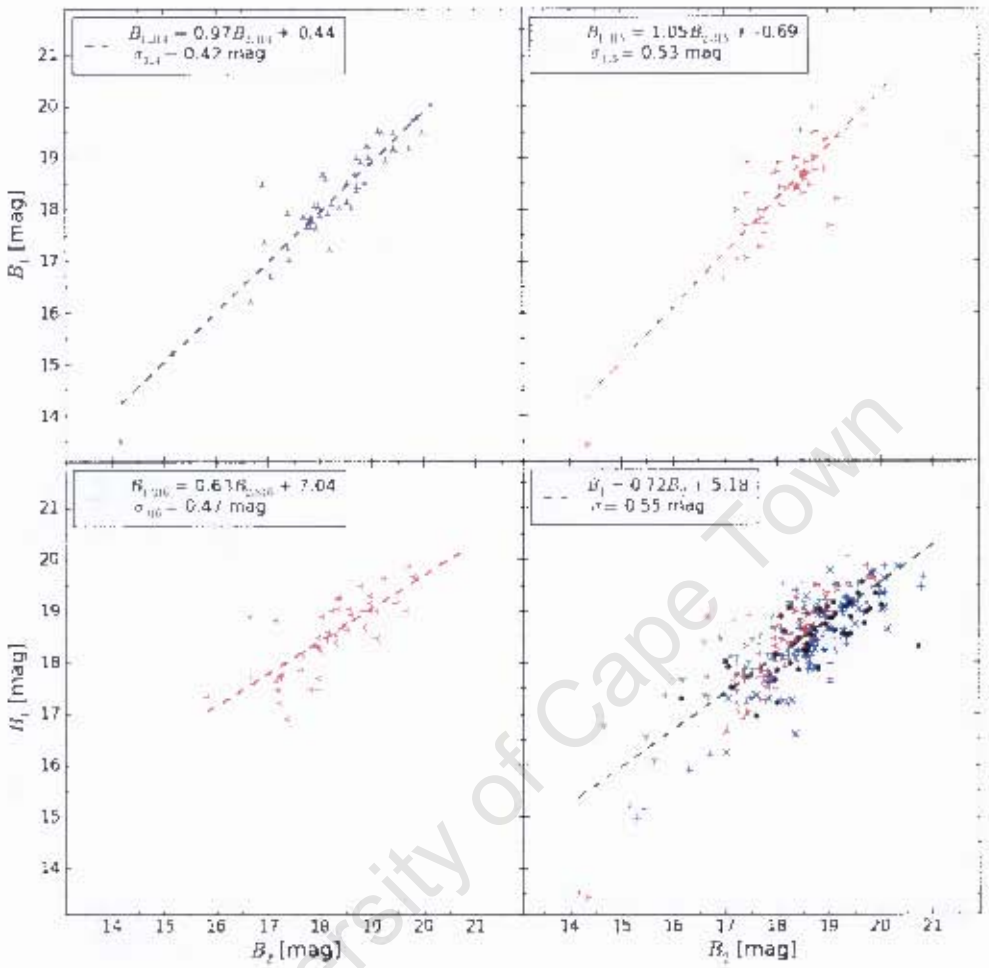

Figure B.4: Magnitude difference and least square fit to Plate 314, 315, 316 all plates.

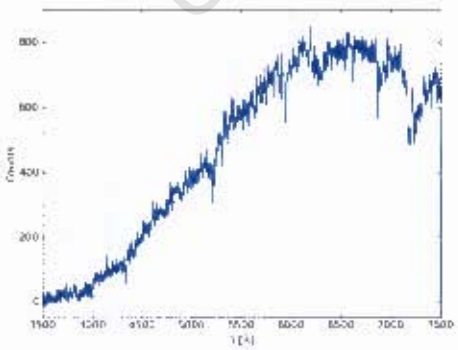

Figure B.5: Spectra for Vela2429

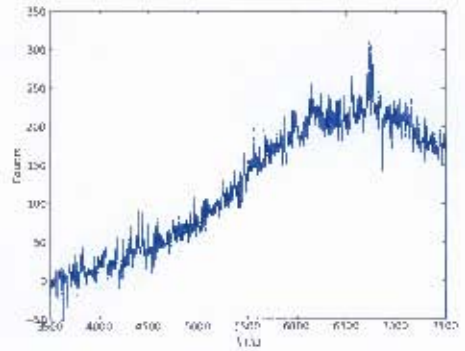

Figure B.6: Spectra for Vela1463

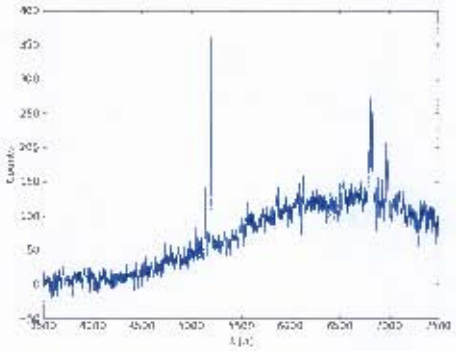

Figure B.7: Spectra for Vela1386

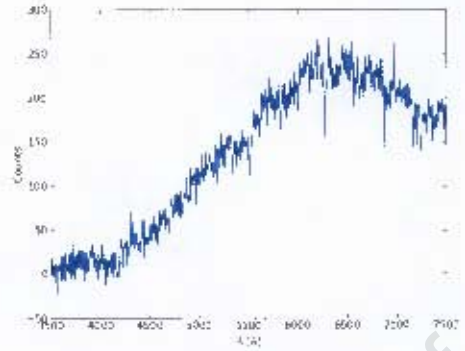

Figure B.8: Spectra for Vela3520

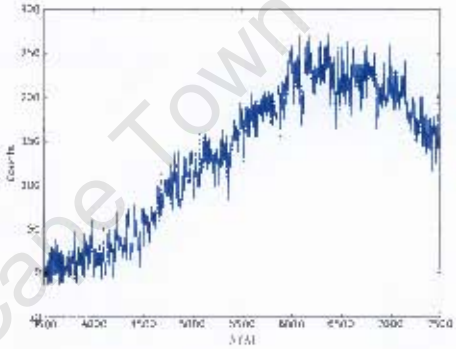

Figure B.9: Spectra for Vela3376

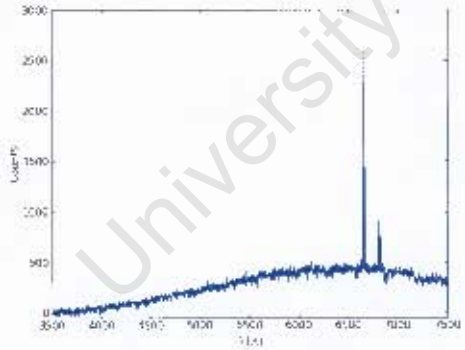

Figure B.10: Spectra for Vela3650

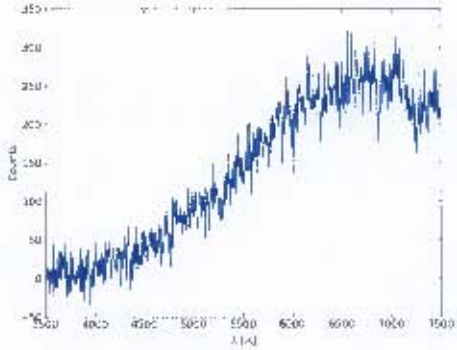

Figure B.11: Spectra for Vela1001

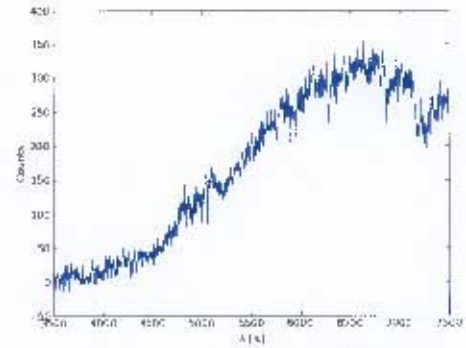

Figure B.12: Spectra for Vela0948

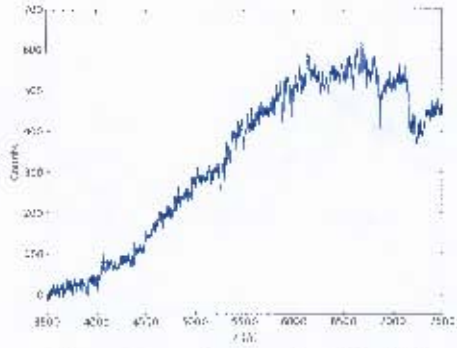

Figure B.13: Spectra for Vela2524

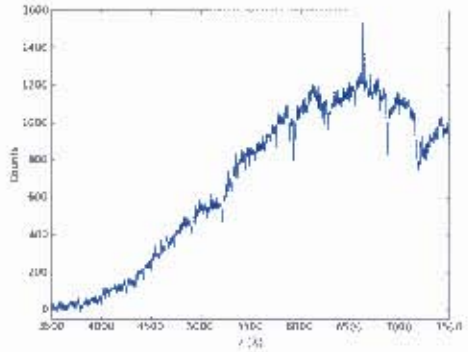

Figure B.14: Spectra for Vela2520

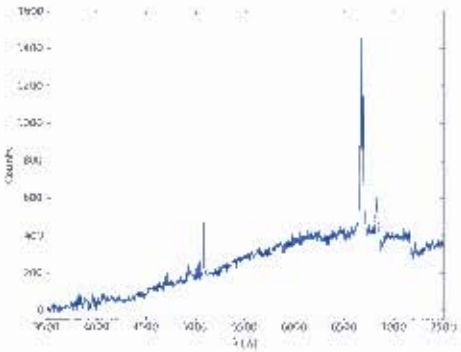

Figure B.15: Spectra for Vela2107

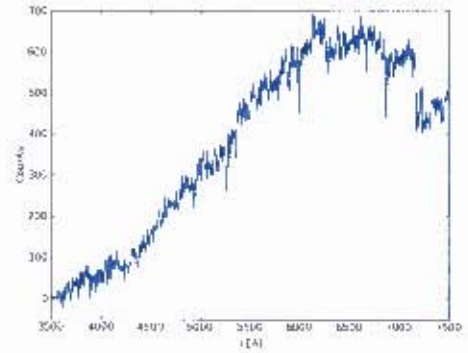

Figure B.16: Spectra for Vela2609

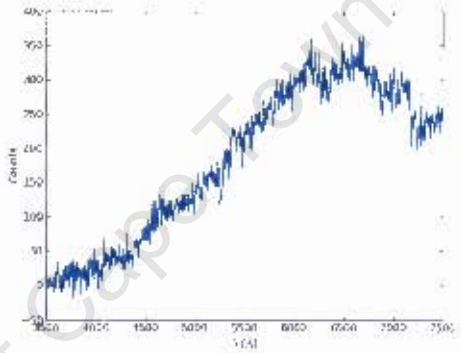

Figure B.17: Spectra for Vela2657

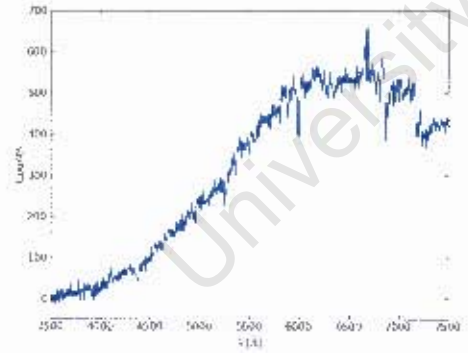

Figure B.18: Spectra for Vela2658

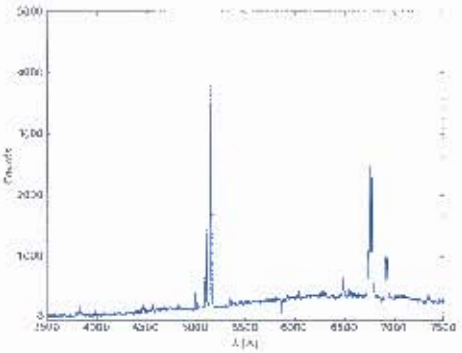

Figure B.19: Spectra for Vela0406

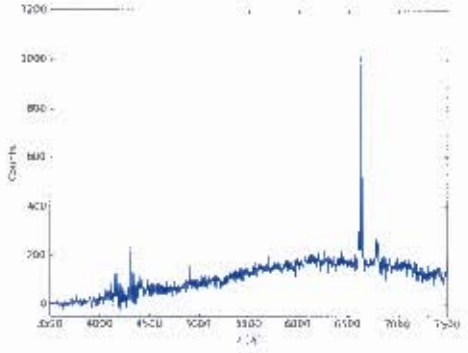

Figure B.20: Spectra for Vela0369

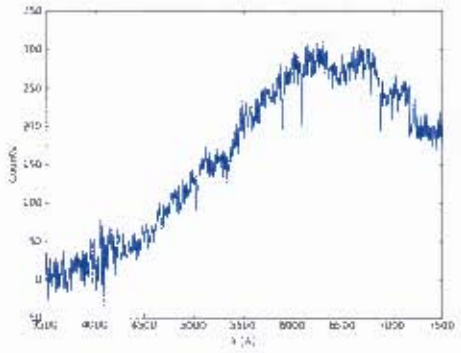

Figure B.21: Spectra for Vela0374

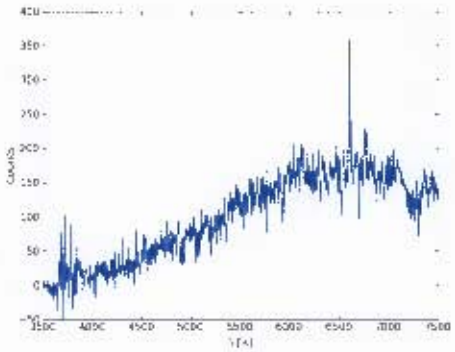

Figure B.22: Spectra for Vela0341

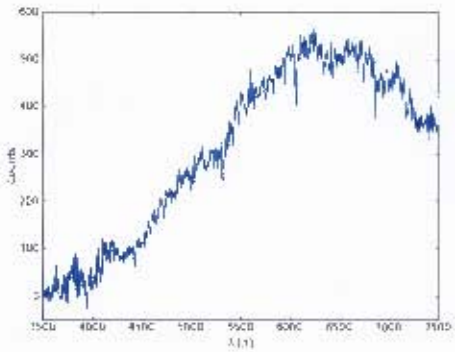

Figure B.23: Spectra for Vela0276

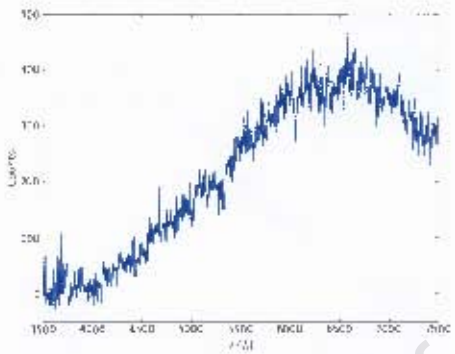

Figure B.24: Spectra for Vela0297

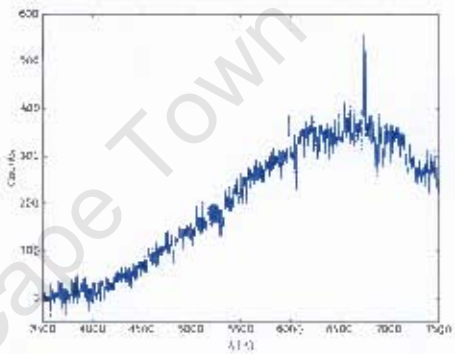

Figure B.25: Spectra for Vela0235

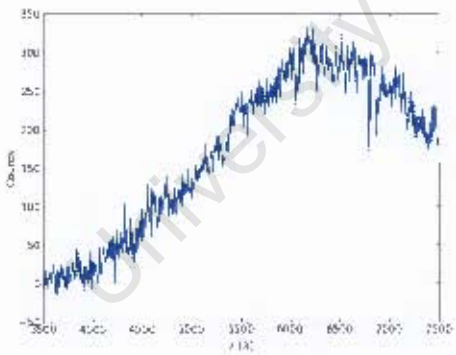

Figure B.26: Spectra for Vela0189

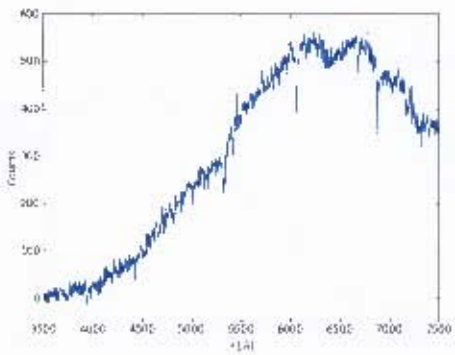

Figure B.27: Spectra for Vela0175

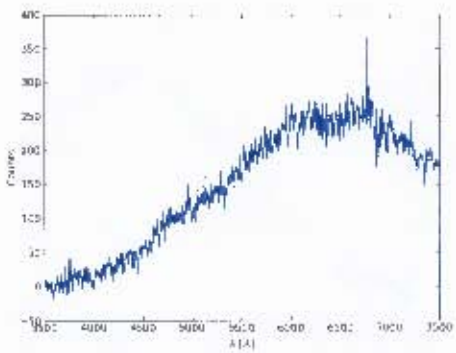

Figure B.28: Spectra for Vela0178

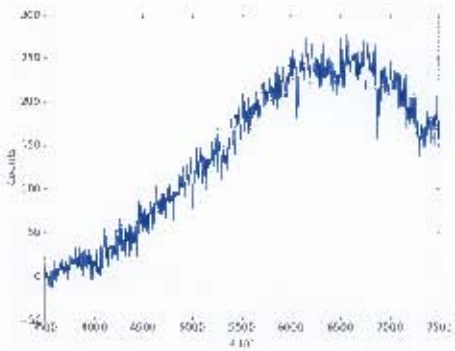

Figure B.29: Spectra for Vela0181

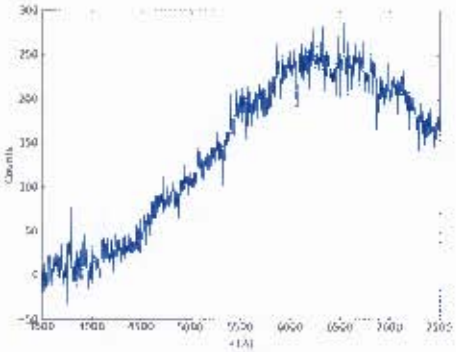

Figure B.30: Spectra for Vela0168

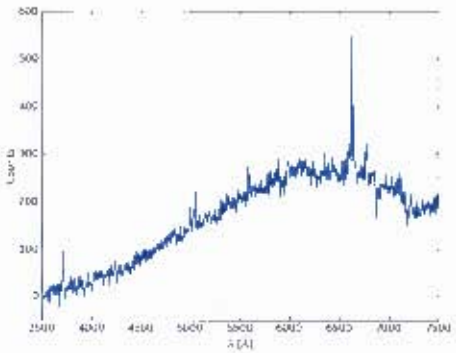

Figure B.31: Spectra for Vela0071

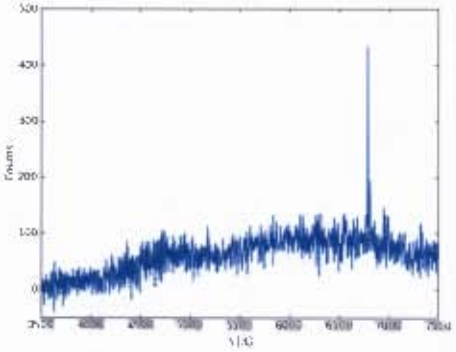

Figure B.32: Spectra for Vela0023

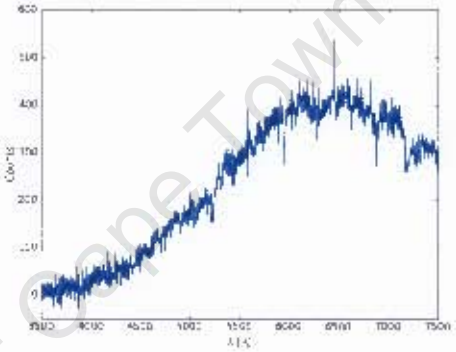

Figure B.33: Spectra for Vela0310

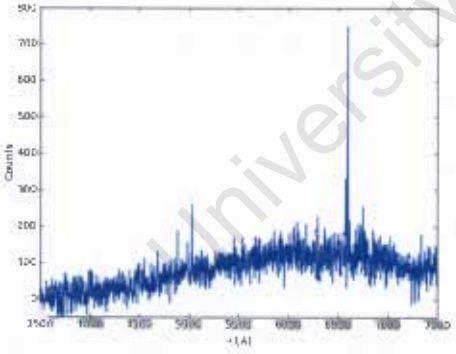

Figure B.34: Spectra for Vela0763

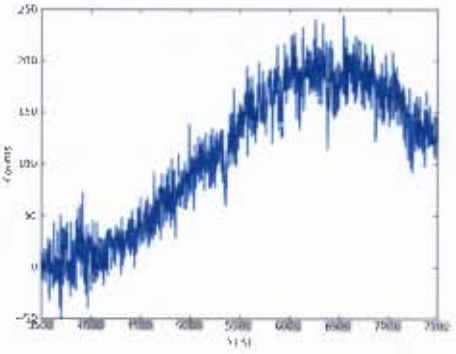

Figure B.35: Spectra for Vela0489

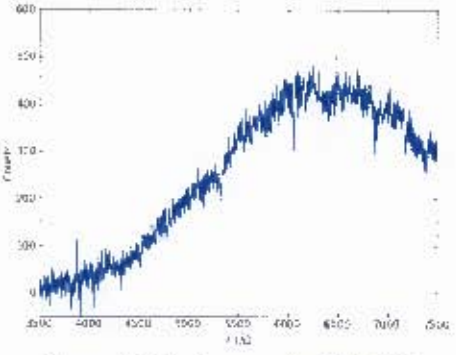

Figure B.36: Spectra for Vela0676

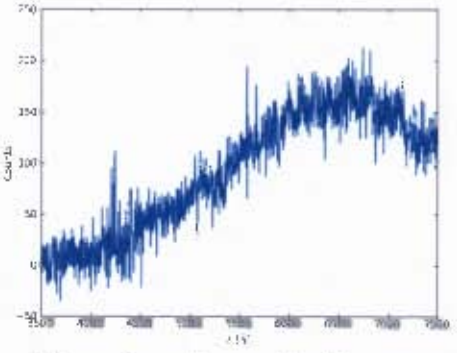

Figure B.37: Spectra for Vela0466

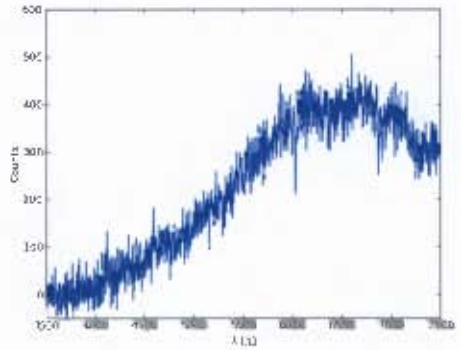

Figure B.38: Spectra for Vela0670

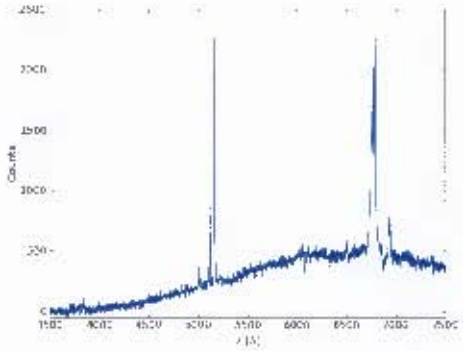

Figure B.39: Spectra for Vela0173

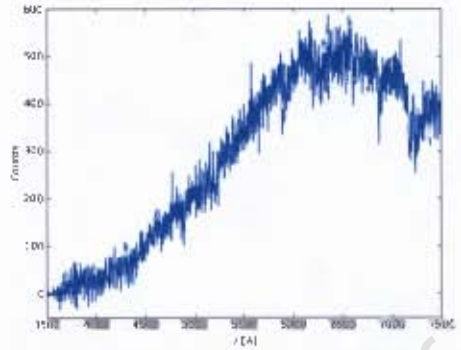

Figure B.40: Spectra for Vela1891

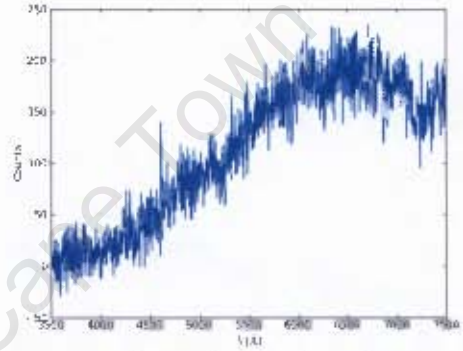

Figure B.41: Spectra for Vela1880

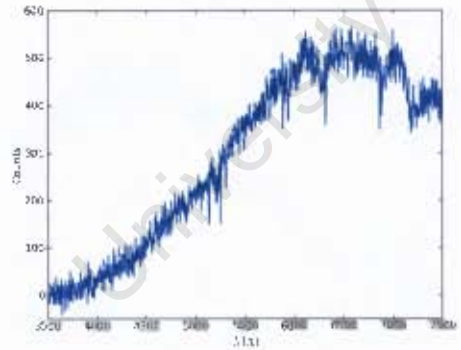

Figure B.42: Spectra for Vela1803

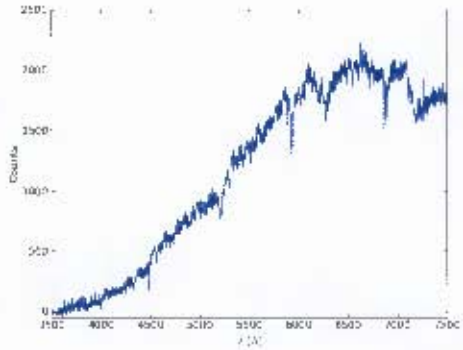

Figure B.43: Spectra for Vela1836

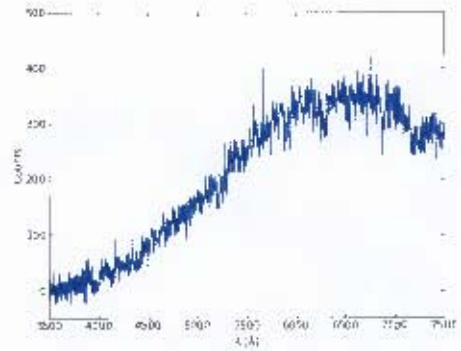

Figure B.44: Spectra for Vela1823

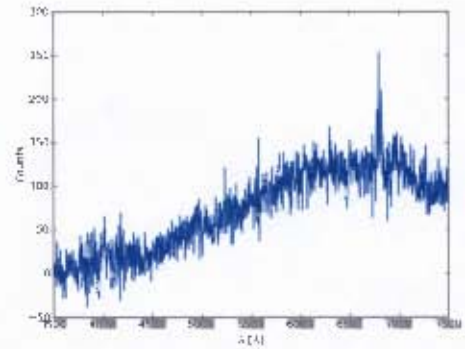

Figure B.45: Spectra for Vela1860

Appendix C

Detailed IRAF Reduction

The reduction steps from the raw CCD image to a two dimensional, wavelength calibrated spectrum are outlined in detail below.

1. The `noao` package is loaded which contains all the packages needed for spectroscopic reduction (Valdes 1992).

2. The package for generic CCD reductions `ccdred` within the image reduction package, `imred`, is loaded.

3. To remove the bias using the overscan region the task `ccdproc` is used.

4. The task `flatcomb` combines and processes flat field images.

5. The package to analyse longslit data, `longslit`, within the package `twodspec` has the task `response`. `response` is used to determine the response calibration.

6. The task `ccdproc` is used to correct for the CCD response. In this particular instance the CCD response for short wavelengths ($\sim$ 3000 – 4000Å) was very low. Dividing this observed low signal by a low valued response function resulted in high noise that masked any features at this end of the spectrum. Therefore this step was omitted.

7. A few rows at the top and bottom of the two dimensional data is cropped where response is not good. The rows selected where those between 35 and 115.

8. The package developed for Kitt Peak National Observatory low/moderate dispersion slits (`kpnoslit`) is loaded and the task `apall` is used to extract the one dimensional spectrum. The `apall` task is used to select the rows containing the galaxy spectrum ($\sim$ row 65 $\pm$ 5 rows) and the colons to use for background subtraction. The trace of the intensity peak of the galaxy across the columns is found and any obvious cosmic rays are 'cleaned' by `apall`.

9. The `identify` task is used to identify the arc lines and the dispersion function for the arc lamp spectrum. This is done for one arc spectrum.

10. The task `reidentify`, reidentifies the arc spectra using the spectrum calibrated in step 9 and calculates a new dispersion function for each spectrum.

11. The `refspectra` task assigns the reference (arc) spectra to the spectra of the galaxies.

12. The task `dispcor` corrects the dispersion of the galaxy spectra, in other words carries out wavelength calibration. Now the one dimensional spectra are extracted and wavelength calibrated.

13. Within the `onedspec` package the task `scombine` is used to combine spectra if multiple exposures were taken of one galaxy.

14. The next to last step is to remove any cosmic rays that escaped the earlier algorithm manually using the task `splot`.

15. Finally, for objects that were observed more than once the spectra are stacked using the task `scombine`.

Bibliography

1983, U.K. Schmidt telescope handbook: the U.K. Schmidt telescope unit of Royal observatory, Edinburgh (Royal observatory)

Abate, A. & Feldman, H. A. 2012, MNRAS, 419, 3482

Abell, G. O. 1975, Clusters of Galaxies, ed. Sandage, A., Sandage, M., & Kristian, J. (the University of Chicago Press), 601

Baade, W. 1946, PASP, 58, 249

Benjamin, R. A., Churchwell, E., Babler, B. L., Bania, T. M., Clemens, D. P., Cohen, M., Dickey, J. M., Indebetouw, R., Jackson, J. M., Kobulnicky, H. A., Lazarian, A., Marston, A. P., Mathis, J. S., Meade, M. R., Seager, S., Stolovy, S. R., Watson, C., Whitney, B. A., Wolff, M. J., & Wolfire, M. G. 2003, PASP, 115, 953

Bennett, C. L., Halpern, M., Hinshaw, G., Jarosik, N., Kogut, A., Limon, M., Meyer, S. S., Page, L., Spergel, D. N., Tucker, G. S., Wollack, E., Wright, E. L., Barnes, C., Greason, M. R., Hill, R. S., Komatsu, E., Nolta, M. R., Odegard, N., Peiris, H. V., Verde, L., & Weiland, J. L. 2003, ApJS, 148, 1

Bilicki, M., Chodorowski, M., Jarrett, T., & Mamon, G. A. 2011, ApJ, 741, 31

Böhringer, H., Schuecker, P., Komossa, S., Retzlaff, J., Reiprich, T. H., & Voges, W. 2000, in Astronomical Society of the Pacific Conference Series, Vol. 218, Mapping the Hidden Universe: The Universe behind the Mily Way - The Universe in HI, ed. R. C. Kraan-Korteweg, P. A. Henning, & H. Andernach, 93

Bottinelli, L., Durand, N., Fouque, P., Garnier, R., Gouguenheim, L., Loulergue, M., Paturel, G., Petit, C., & Teerikorpi, P. 1993, A&AS, 102, 57

Cameron, L. M. 1990, A&A, 233, 16

Cardelli, J. A., Clayton, G. C., & Mathis, J. S. 1989, ApJ, 345, 245

Carey, S. J. 2008, in Bulletin of the American Astronomical Society, Vol. 40, American Astronomical Society Meeting Abstracts #212, 255–+

Carroll, B. W. & Ostlie, D. A. 2007, An Introduction to Modern Astrophysics, 2nd edn. (Pearson Addison-Wesley)

Chamaraux, P., Cayatte, V., Balkowski, C., & Fontanelli, P. 1990, A&A, 229, 340

Collobert, M., Sarzi, M., Davies, R. L., Kuntschner, H., & Colless, M. 2006, MNRAS, 370, 1213

Crook, A. C., Huchra, J. P., Martimbeau, N., Masters, K. L., Jarrett, T., & Macri, L. M. 2008, ApJ, 685, 1320

de Vaucouleurs, G. 1958, Nature, 182, 1478

de Vaucouleurs, G., de Vaucouleurs, A., & Corwin, Jr., H. G. 1976, Second reference catalogue of bright galaxies. Containing information on 4,364 galaxies with references to papers published between 1964 and 1975., ed. de Vaucouleurs, G., de Vaucouleurs, A., & Corwin, H. G., Jr.

de Vaucouleurs, G., de Vaucouleurs, A., Corwin, Jr., H. G., Buta, R. J., Paturel, G., & Fouque, P. 1991, Third Reference Catalogue of Bright Galaxies, ed. de Vaucouleurs, G., de Vaucouleurs, A., Corwin, H. G., Jr., Buta, R. J., Paturel, G., & Fouque, P.

Donley, J. L. et al. 2005, AJ, 129, 220

Drinkwater, M. J., Barnes, D. G., & Ellison, S. L. 1995, PASA, 12, 248

Ebeling, H., Kocevski, D., Tully, R. B., & Mullis, C. R. 2005, in Astronomical Society of the Pacific Conference Series, Vol. 329, Nearby Large-Scale Structures and the Zone of Avoidance, ed. A. P. Fairall & P. A. Woudt, 83–+

Erdoğdu, P., Huchra, J. P., Lahav, O., Colless, M., Cutri, R. M., Falco, E., George, T., Jarrett, T., Jones, D. H., Kochanek, C. S., Macri, L., Mader, J., Martimbeau, N., Pahre, M., Parker, Q., Rassat, A., & Saunders, W. 2006a, MNRAS, 368, 1515

Erdoğdu, P., Lahav, O., Huchra, J. P., Colless, M., Cutri, R. M., Falco, E., George, T., Jarrett, T., Jones, D. H., Macri, L. M., Mader, J., Martimbeau, N., Pahre, M. A., Parker, Q. A., Rassat, A., & Saunders, W. 2006b, MNRAS, 373, 45

Fairall, A. P. 1988, MNRAS, 233, 691

Fairall, A. P., ed. 1998, Large-scale structures in the universe

Fairall, A. P. & Kraan-Korteweg, R. C. 2000, in Astronomical Society of the Pacific Conference Series, Vol. 218, Mapping the Hidden Universe: The Universe behind the Mily Way - The Universe in HI, ed. R. C. Kraan-Korteweg, P. A. Henning, & H. Andernach, 35–+

Feldman, H. A., Watkins, R., & Hudson, M. J. 2010, MNRAS, 407, 2328

Fisher, K. B., Huchra, J. P., Strauss, M. A., Davis, M., Yahil, A., & Schlegel, D. 1995, ApJS, 100, 69

Hasegawa, T., Wakamatsu, K., Malkan, M., Sekiguchi, K., Menzies, J. W., Parker, Q. A., Jugaku, J., Karoji, H., & Okamura, S. 2000a, MNRAS, 316, 326

—. 2000b, MNRAS, 316, 326

Hau, G. K. T., Ferguson, H. C., Lahav, O., & Lynden-Bell, D. 1995, MNRAS, 277, 125

Henning, P. A., Kraan-Korteweg, R. C., & Staveley-Smith, L. 2005, in Astronomical Society of the Pacific Conference Series, Vol. 329, Nearby Large-Scale Structures and the Zone of Avoidance, ed. A. P. Fairall & P. A. Woudt, 199

Herschel, J. F. W. 1864, Royal Society of London Philosophical Transactions Series I, 154, 1

Hogg, D. W., Eisenstein, D. J., Blanton, M. R., Bahcall, N. A., Brinkmann, J., Gunn, J. E., & Schneider, D. P. 2005, ApJ, 624, 54

Hubble, E. 1929, Proceedings of the National Academy of Science, 15, 168

Hubble, E. P. 1925, The Observatory, 48, 139

Huchra, J. P., Macri, L. M., Masters, K. L., Jarrett, T. H., Berlind, P., Calkins, M., Crook, A. C., Cutri, R., Erdogdu, P., Falco, E., George, T., Hutcheson, C. M., Lahav, O., Mader, J., Mink, J. D., Martimbeau, N., Schneider, S., Skrutskie, M., Tokarz, S., & Westover, M. 2011, ArXiv e-prints

Hudson, M. J., Smith, R. J., Lucey, J. R., & Branchini, E. 2004, MNRAS, 352, 61

Jarrett, T. 2004, Publications of the Astronomical Society of Australia, 21, 396

Jarrett, T. H., Chester, T., Cutri, R., Schneider, S., Skrutskie, M., & Huchra, J. P. 2000, AJ, 119, 2498

Jarrett, T. H., Koribalski, B. S., Kraan-Korteweg, R. C., Woudt, P. A., Whitney, B. A., Meade, M. R., Babler, B., Churchwell, E., Benjamin, R. A., & Indebetouw, R. 2007, AJ, 133, 979

Johnston, M. D., Bradt, H. V., Doxsey, R. E., Marshall, F. E., Schwartz, D. A., & Margon, B. 1981, ApJ, 245, 799

Jones, D. H., Read, M. A., Saunders, W., Colless, M., Jarrett, T., Parker, Q. A., Fairall, A. P., Mauch, T., Sadler, E. M., Watson, F. G., Burton, D., Campbell, L. A., Cass, P., Croom, S. M., Dawe, J., Fiegert, K., Frankcombe, L., Hartley, M., Huchra, J., James, D., Kirby, E., Lahav, O., Lucey, J., Mamon, G. A., Moore, L., Peterson, B. A., Prior, S., Proust, D., Russell, K., Safouris, V., Wakamatsu, K., Westra, E., & Williams, M. 2009, MNRAS, 399, 683

Joyce, M., Sylos Labini, F., Gabrielli, A., Montuori, M., & Pietronero, L. 2005, A&A, 443, 11

Kant, I. 1755, Allgemeine Naturgeschichte und Theorie des Himmels, ed. Kant, I.

Kashlinsky, A., Atrio-Barandela, F., & Ebeling, H. 2011, ApJ, 732, 1

Kashlinsky, A., Atrio-Barandela, F., Ebeling, H., Edge, A., & Kocevski, D. 2010, ApJ, 712, L81

Kashlinsky, A., Atrio-Barandela, F., Kocevski, D., & Ebeling, H. 2008, ApJ, 686, L49

Kocevski, D. D. & Ebeling, H. 2006, ApJ, 645, 1043

Kolatt, T., Dekel, A., & Lahav, O. 1995, MNRAS, 275, 797

Koribalski, B. S. & López-Sánchez, Á. R. 2009, MNRAS, 400, 1749

Kraan-Korteweg, R. C. 2000, A&AS, 141, 123

Kraan-Korteweg, R. C., Fairall, A. P., & Balkowski, C. 1994, VizieR Online Data Catalog, 329, 70617

—. 1995, A&A, 297, 617

Kraan-Korteweg, R. C. & Jarrett, T. 2005, in Astronomical Society of the Pacific Conference Series, Vol. 329, Nearby Large-Scale Structures and the Zone of Avoidance, ed. A. P. Fairall & P. A. Woudt, 119–+

Kraan-Korteweg, R. C. & Lahav, O. 2000, A&A Rev., 10, 211

Kraan-Korteweg, R. C., Woudt, P. A., Cayatte, V., Fairall, A. P., Balkowski, C., & Henning, P. A. 1996, Nature, 379, 519

Kurtz, M. J. & Mink, D. J. 1998, PASP, 110, 934

Lahav, O., Fisher, K. B., Hoffman, Y., Scharf, C. A., & Zaroubi, S. 1994, ApJ, 423, L93

Lauberts, A. 1982, ESO/Uppsala survey of the ESO(B) atlas, ed. Lauberts, A.

Lavaux, G., Tully, R. B., Mohayaee, R., & Colombi, S. 2010, ApJ, 709, 483

Lercher, G., Kerber, F., & Weinberger, R. 1996, A&AS, 117, 369

Lewis, G. & Irwin, M. 1996, IEEE Spectrum, 12, 22

Lineweaver, C. H., Tenorio, L., Smoot, G. F., Keegstra, P., Banday, A. J., & Lubin, P. 1996, ApJ, 470, 38

Loeb, A. & Narayan, R. 2008, MNRAS, 386, 2221

Lynden-Bell, D., Faber, S. M., Burstein, D., Davies, R. L., Dressler, A., Terlevich, R. J., & Wegner, G. 1988, ApJ, 326, 19

Lynden-Bell, D., Lahav, O., & Burstein, D. 1989, MNRAS, 241, 325

Macaulay, E., Feldman, H., Ferreira, P. G., Hudson, M. J., & Watkins, R. 2011, MNRAS, 414, 621

Marchiotto, W., Wildauer, H., & Weinberger, R. 1999, in Astronomische Gesellschaft Meeting Abstracts, Vol. 15, Astronomische Gesellschaft Meeting Abstracts, ed. R. E. Schielicke, 86–+

Marleau, F. R., Noriega-Crespo, A., Paladini, R., Clancy, D., Carey, S., Shenoy, S., Kraemer, K. E., Kuchar, T., Mizuno, D. R., & Price, S. 2008, AJ, 136, 662

Meyer, M. J., Zwaan, M. A., Webster, R. L., Staveley-Smith, L., Ryan-Weber, E., Drinkwater, M. J., Barnes, D. G., Howlett, M., Kilborn, V. A., Stevens, J., Waugh, M., Pierce, M. J., Bhathal, R., de Blok, W. J. G., Disney, M. J., Ekers, R. D., Freeman, K. C., Garcia, D. A., Gibson, B. K., Harnett, J., Henning, P. A., Jerjen, H., Kesteven, M. J., Knezek, P. M., Koribalski, B. S., Mader, S., Marquarding, M., Minchin, R. F., O'Brien, J., Oosterloo, T., Price, R. M., Putman, M. E., Ryder, S. D., Sadler, E. M., Stewart, I. M., Stootman, F., & Wright, A. E. 2004, MNRAS, 350, 1195

Neugebauer, G., Habing, H. J., van Duinen, R., Aumann, H. H., Baud, B., Beichman, C. A., Beintema, D. A., Boggess, N., Clegg, P. E., de Jong, T., Emerson, J. P., Gautier, T. N., Gillett, F. C., Harris, S., Hauser, M. G., Houck, J. R., Jennings, R. E., Low, F. J., Marsden, P. L., Miley, G., Olnon, F. M., Pottasch, S. R., Raimond, E., Rowan-Robinson, M., Soifer, B. T., Walker, R. G., Wesselius, P. R., & Young, E. 1984, ApJ, 278, L1

Pantoja, C. A., Altschuler, D. R., Giovanardi, C., & Giovanelli, R. 1994, in Astronomical Society of the Pacific Conference Series, Vol. 67, Unveiling Large-Scale Structures Behind the Milky Way, ed. C. Balkowski & R. C. Kraan-Korteweg, 143–+

Pantoja, C. A., Altschuler, D. R., Giovanardi, C., & Giovanelli, R. 1997, AJ, 113, 905

Paturel, G., Petit, C., Prugniel, P., Theureau, G., Rousseau, J., Brouty, M., Dubois, P., & Cambrésy, L. 2003, A&A, 412, 45

Peebles, P. J. E., Phelps, S. D., Shaya, E. J., & Tully, R. B. 2001, ApJ, 554, 104

Pratt, N. M. 1977, Vistas in Astronomy, 21, 1

Proctor, R. 1887, The Universe of Stars (London: Longman, Green and Co.), 41

Roman, A. T., Nakanishi, K., & Saito, M. 1998, PASJ, 50, 37

Roman, A. T., Nakanishi, K., Tomita, A., & Saito, M. 1996, PASJ, 48, 679

Saito, M., Ohtani, H., Asonuma, A., Kashikawa, N., Maki, T., Nishida, S., & Watanabe, T. 1990, PASJ, 42, 603

Saito, M., Ohtani, H., Baba, A., Hotta, H., Kameno, S., Kurosu, S., Nakada, K., & Takata, T. 1991, PASJ, 43, 449

Salem, C. 1996, Master's thesis, Universite Paris

Saurer, W., Seeberger, R., & Weinberger, R. 1997, A&AS, 126, 247

Schechter, P. 1976, ApJ, 203, 297

Schlegel, D. J., Finkbeiner, D. P., & Davis, M. 1998, ApJ, 500, 525

Seeberger, R. & Saurer, W. 1998, A&AS, 127, 101

Seeberger, R., Saurer, W., & Weinberger, R. 1996, A&AS, 117, 1

Seeberger, R., Saurer, W., Weinberger, R., & Lercher, C. 1994, in Astronomical Society of the Pacific Conference Series, Vol. 67, Unveiling Large-Scale Structures Behind the Milky Way, ed. C. Balkowski & R. C. Kraan-Korteweg, 81–+

Shafi. N. 2008, Master's thesis, University of Cape Town

Shane, C. D. & Wirtanen, C. A. 1967, Publ. Lick Obs. XXII, Pt 1

Shapley, H. 1961, Galaxies (Cambridge: Harvard University Press), 159

Skrutskie, M. F., Cutri, R. M., Stiening, R., Weinberg, M. D., Schneider, S., Carpenter, J. M., Beichman, C., Capps, R., Chester, T., Elias, J., Huchra, J., Liebert, J., Lonsdale, C., Monet, D. G., Price, S., Seitzer, P., Jarrett, T., Kirkpatrick, J. D., Gizis, J. E., Howard, E., Evans, T., Fowler, J., Fullmer, L., Hurt, R., Light, R., Kopan, E. L., Marsh, K. A., McCallon, H. L., Tam, R., Van Dyk, S., & Wheelock, S. 2006, AJ, 131, 1163

Soifer, B. T., Sanders, D. B., Madore, B. F., Neugebauer, G., Danielson, G. E., Elias, J. H., Lonsdale, C. J., & Rice, W. L. 1987, ApJ, 320, 238

Sparke, L. S. & Gallagher, III, J. S. 2007, Galaxies in the Universe: An Introduction, ed. Sparke, L. S. & Gallagher, J. S., III (Cambridge University Press)

Stein, P. 1996, A&AS, 116, 203

Tammann, G. A. & Sandage, A. 1985, ApJ, 294, 81

Theureau, G., Bottinelli, L., Coudreau-Durand, N., Gouguenheim, L., Hallet, N., Loulergue, M., Paturel, G., & Teerikorpi, P. 1998, A&AS, 130, 333

Tonry, J. & Davis, M. 1979, AJ, 84, 1511

Trumpler, R. J. 1930, PASP, 42, 214

Tully, R. B. & Fisher, J. R. 1987, Nearby galaxies Atlas, ed. Tully, R. B. & Fisher, J. R.

Valdes, F. 1992, in Astronomical Society of the Pacific Conference Series, Vol. 25, Astronomical Data Analysis Software and Systems I, ed. D. M. Worrall, C. Biemesderfer, & J. Barnes, 417–+

Wakamatsu, K., Hasegawa, T., Karoji, H., Sekiguchi, K., Menzies, J. W., & Malkan, M. 1994, in Astronomical Society of the Pacific Conference Series, Vol. 67, Unveiling Large-Scale Structures Behind the Milky Way, ed. C. Balkowski & R. C. Kraan-Korteweg, 131–+

Wakamatsu, K. & Malkan, M. A. 1981, PASJ, 33, 57

Wakamatsu, K., Malkan, M. A., Nishida, M. T., Parker, Q. A., Saunders, W., & Watson, F. G. 2005, in Astronomical Society of the Pacific Conference Series, Vol. 329, Nearby Large-Scale Structures and the Zone of Avoidance, ed. A. P. Fairall & P. A. Woudt, 189–+

Watkins, R., Feldman, H. A., & Hudson, M. J. 2009, MNRAS, 392, 743

Weinberger, R., Gajdošík, M., & Zanin, C. 1999, A&AS, 137, 293

Wheelock, S. L., Gautier, T. N., Chillemi, J., Kester, D., McCallon, H., Oken, C., White, J., Gregorich, D., Boulanger, F., & Good, J. 1994, NASA STI/Recon Technical Report N, 95, 22539

Woudt, P. A. 1998a, PhD thesis, , Univ. of Cape Town, South Africa, (1998)

—. 1998b, PhD thesis, , Univ. of Cape Town, South Africa, (1998)

Woudt, P. A. & Kraan-Korteweg, R. C. 2001, A&A, 380, 441

Woudt, P. A., Kraan-Korteweg, R. C., Lucey, J., Fairall, A. P., & Moore, S. A. W. 2008, MNRAS, 383, 445

Wright, E. L., Eisenhardt, P. R. M., Mainzer, A. K., Ressler, M. E., Cutri, R. M., Jarrett, T., Kirkpatrick, J. D., Padgett, D., McMillan, R. S., et al. 2010, AJ, 140, 1868

Yahil, A., Strauss, M. A., Davis, M., & Huchra, J. P. 1991, ApJ, 372, 380

Yamada, T., Tomita, A., Saito, M., Chamaraux, P., & Kazes, I. 1994, MNRAS, 270, 93